ISSN : 2349-6495(P) | 2456-1908 (O)

International Journal of Advanced Engineering Research and Science

(IJAERS)

An Open Access Peer-Reviewed International Journal

Journal DOI: 10.22161/ijaers

Issue DOI: 10.22161/ijaers.115

AI PUBLICATIONS

Vol.- 11 | Issue - 5 | May 2024

editor.ijaers@gmail.com | editor@ijaers.com | https://www.ijaers.com/

International Journal of Advanced Engineering Research and Science

(IJAERS)

(ISSN: 2349-6495(P)| 2456-1908(O))

DOI: 10.22161/ijaers

Vol-11, Issue-5

May, 2024

Publisher

AI Publication

Email: editor.ijaers@gmail.com; editor@ijaers.com

Web: www.ijaers.com

Vol-11, Issue-5, May, 2024

(10.22161/ijaers.115)

Detail with DOI (CrossRef)

Alternative Algorithms for Time Series Water Wave Modeling
Syawaluddin Hutahaean
DOI: 10.22161/ijaers.115.1
Page No: 01-11

Assessing Solar Tracker Effectiveness in Diverse Weather Conditions
Amol Prakash, Kamlesh Lal, Maneesh
DOI: 10.22161/ijaers.115.2
Page No: 12-19

Prevalence of Tuberculosis in the Brazilian Population and Its Aggravating Factors – Systematic Review
Amanda Lima Franco, Amanda Patrícia Gaudio Bayma, Ana Carolina Abdon Seixas, Arthur Henzo da Silva Santos, Bárbara Ferreira Pereira, Daniele Lima da Costa, Maria Gabriela Perdigão Barros Monteiro, Isabela Lima Christo Alves De Campos, Lohanna Gama Nunes, Leonildo Pinheiro de Sousa Junior, Jéssica Pará Amaral de Oliveira, Luiza Bastos Campos, Maria Eduarda Menezes Almeida, Maria Mirella Nunes Bessa Guerra, Rayssa Lima Vilela, Amanda Fernandes Merhe, Antônio Rudyson Maravalhas de Barros, Bernar A Macedo Alves, Vitor Rocha Leitao, Renan Willian Costa da Silva, Brendo Silva Gaia Farias, Luíza Fernandes Malheiro, Leonardo Wanzeller Magalhães, Maria Rita Barboza Rocha, Ana Maria Ferreira Cruz Toledo
DOI: 10.22161/ijaers.115.3
Page No: 20-23

Climate analysis of the semi-arid region of Paraíba: Challenges and sustainable strategies
Amanda Cristiane Gonçalves Fernandes, Raimundo Aprígio de Menezes Júnior
DOI: 10.22161/ijaers.115.4
Page No: 24-34

Quantum Machine Learning: Exploring Quantum Algorithms for Enhancing Deep Learning Models
Hari Gonaygunta, Mohan Harish Maturi, Geeta Sandeep Nadella, Karthik Meduri, Snehal Satish5
DOI: 10.22161/ijaers.115.5
Page No: 35-41

A Web-Based "Department Management System" for Academic Institutions
Kulkarni Rohini, Shelke Aditi, Mane Rutuja, Kulkarni Shruti, Prof. D.P. Kulkarni
DOI: 10.22161/ijaers.115.6
Page No: 42-44

Effect of Charging Current Variation on Internal Resistance in Lithium-Ion Batteries
Keshawa Udiatma, Trias Andromeda, Dr. Iwan Setiawan
DOI: 10.22161/ijaers.115.7
Page No: 45-50

International Journal of Advanced Engineering Research and Science (IJAERS)
Peer-Reviewed Journal
ISSN: 2349-6495(P) | 2456-1908(O)
Vol-11, Issue-5; May, 2024
Journal Home Page Available: https://ijaers.com/
Article DOI: https://dx.doi.org/10.22161/ijaers.115.1

Alternative Algorithms for Time Series Water Wave Modeling

Syawaluddin Hutahaean

Ocean Engineering Program, Faculty of Civil and Environmental Engineering,-Bandung Institute of Technology (ITB), Bandung 40132, Indonesia
syawalf1@yahoo.co.id

Received: 07 Mar 2024,

Receive in revised form: 21 Apr 2024,

Accepted: 03 May 2024,

Available online: 11 May 2024

***Keywords*— calculation algorithm, conservation of energy.**

***Abstract*— This research builds upon Hutahaean (2024a), focusing on time series water wave modeling, with substantial portions of this article derived from that prior study. Modifications were made to the calculation algorithm; specifically, vertical water particle velocity is now computed using the continuity equation, and water surface elevation is determined through kinematic free surface boundary conditions. While this revised algorithm enables the model to simulate wave breaking, it results in an excessively high breaker height and struggles to accurately simulate wave conditions post-breaking, particularly at large wave heights. To address these challenges, the kinetic energy conservation equation was integrated into the model. This addition facilitated the creation of a water surface elevation equation through the superposition of kinematic free surface boundary conditions and the kinetic energy conservation equation. This integration yields an equation that maintains a balance between changes in potential energy and changes in kinetic energy, enhancing the model's capability to simulate both the shoaling-breaking process and subsequent wave conditions in shallow waters more effectively.*

I. INTRODUCTION

Time series water wave modeling continues to evolve, particularly due to challenges in accurately modeling complex phenomena such as wave diffraction at breakwater gaps. Traditional methods based on velocity potential theory often fall short in these areas. A more robust approach is the use of the Boussinesq equation, which has been significantly developed by researchers such as Boussinesq, J. (1871), Dingermans, M.W. (1997), Hamm, L., Madsen, P.A., Peregrine, D.H. (1993), Johnson, R.S. (1997), Kirby, J.T. (2003), and Peregrine, D.H. (1967, 1972), among others.

The conventional time series water wave model primarily comprises two equations: the water surface elevation equation and the horizontal water particle velocity equation. The former is formulated by integrating the continuity equation—taking into account both water depth and vertical surface particle velocity—and applying the Free Surface Boundary Condition. This model is adept at representing shoaling but falls short in simulating wave breaking and post-breaking conditions in shallow waters. While some advancements have been made, as demonstrated by Hutahaean, S. Achiari H. (2017) and Hutahaean S. (2019), the ability to reliably simulate post-breaking conditions remains inconsistent, with some datasets accurately modeled and others not.

Building on this knowledge, recent research by Hutahaean (2024b) has made significant strides. Utilizing velocity potential theory, this study identified that breaking characteristics are prominent in the Kinematic Free Surface Boundary Condition. Leveraging this insight, a new time series water wave model has been developed, incorporating the Kinematic Free Surface Boundary Condition for calculating water surface elevations. This model also utilizes the continuity equation to determine vertical water particle velocities.

The current model successfully simulates shoaling and breaking but tends to overestimate the height of breaking waves and fails to accurately model wave behavior as it progresses into very shallow waters. One significant limitation identified is within the Kinematic Free Surface Boundary Condition, which accounts for changes in potential energy due to variations in water surface elevation without a corresponding adjustment for kinetic energy. This oversight results in an energy imbalance, as there's no accounted source of energy to facilitate the observed changes in potential energy.

To rectify this issue, the model has been refined by integrating the Kinematic Free Surface Boundary Condition with a conservation of kinetic energy equation. This integration ensures a balanced accounting of energy changes, which enhances the accuracy of the water surface elevation predictions.

Additionally, modifications have been made to the Euler momentum conservation equation, as detailed in Hutahaean (2024a). The updated Euler Momentum Conservation Equation now strictly enforces that horizontal velocity changes occur only on the horizontal axis and vertical velocity changes only on the vertical axis.

With these critical modifications, the enhanced time series model now more accurately simulates wave breaking, effectively extending its predictive capabilities to shallow waters near the coast.

II. WEIGHTED TAYLOR SERIES

In this paper, we adopt the $x - z$ coordinate system, where the x -axis represents the horizontal axis and the z -axis denotes the vertical axis.

A weighted Taylor series is a truncated Taylor series limited to first-order terms, with the influence of higher-order terms encapsulated in coefficients known as weighting coefficients.

For a function of two variables $f = f(x\ ,t)$

$$f(x+\delta x, t+\delta t) = f(x,t) + \gamma_{t,2}\delta t\frac{\partial f}{\partial t} + \gamma_x \delta x\frac{\partial f}{\partial x} \quad ....(1)$$

$\gamma_{t,2}$ and γ_x are weighting coefficients.

For function $f = f(x,z,t)$ the weighted Taylor series is

$$f(x+\delta x, z+\delta z, t+\delta t) = f(x,z,t) + \gamma_{t,3}\delta t\frac{\partial f}{\partial t} + \gamma_x \delta x\frac{\partial f}{\partial x} + \gamma_z \delta z\frac{\partial f}{\partial z} \quad ...(2)$$

$\gamma_{t,3}$, γ_x and γ_z are weighting coeffcients. There is no difference between γ_x in $f(x,t)$ and γ_x in $f(x,z,t)$. The basic values of these weighting coefficients are, $\gamma_{t,2} = 2$, $\gamma_{t,3} = 3$, $\gamma_x = 1$ and $\gamma_z = 1$.

The updated weighting coefficient values are presented in Table (1), wherein these coefficients are dependent on the optimization coefficient ε . A larger ε corresponds to a greater influence of higher-order Taylor series terms. The methodology for computing these weighting coefficients is detailed in Hutahaean (2023). However, the precision of the weighting coefficients listed in Table (1) surpasses that of Hutahaean (2023).

In this particular time series model, the selection of weighting coefficients hinges on the wave amplitude. Specifically, a higher wave amplitude corresponds to a larger ε , falling within the range of $0.15 \leq \varepsilon \leq 0.35$.

Table (1) Weighting coefficients.

ε	$\gamma_{t,2}$	$\gamma_{t,3}$	γ_x	γ_z
0.010	1.999797	3.004905	0.998792	1.011458
0.012	1.999707	3.007157	0.998257	1.016713
0.014	1.999600	3.009870	0.997625	1.023049
0.016	1.999477	3.013062	0.996894	1.030512
0.018	1.999336	3.016751	0.996064	1.039152
0.020	1.999178	3.020955	0.995135	1.049022
0.022	1.999002	3.025692	0.994107	1.060178
0.024	1.998809	3.030982	0.992979	1.072679
0.026	1.998599	3.036843	0.991751	1.086589
0.028	1.998370	3.043296	0.990422	1.101976
0.030	1.998124	3.050358	0.988994	1.118910
0.032	1.997859	3.058049	0.987464	1.137468
0.034	1.997576	3.066390	0.985834	1.157729
0.036	1.997275	3.075398	0.984104	1.179778
0.038	1.996954	3.085094	0.982272	1.203703
0.040	1.996615	3.095495	0.980339	1.229598

With the weighted Taylor series, the kinematic free surface boundary condition becomes,

$$w_\eta = \gamma_{t,2}\frac{\partial \eta}{\partial t} + \gamma_x u_\eta \frac{\partial \eta}{\partial x} \quad ....(3)$$

w_η = vertical surface water particle velocity

u_η = horizontal surface water particle velocity

$\eta(x,t)$, water surface elevation equation.

Meanwhile, the total acceleration of horizontal and vertical water particles is,

$$\frac{Du}{dt} = \gamma_{t,3}\frac{\partial u}{\partial t} + \frac{\gamma_x}{2}\frac{\partial uu}{\partial x} + \gamma_z w\frac{\partial u}{\partial z}$$

$$\frac{Dw}{dt}=\gamma_{t,3}\frac{\partial w}{\partial t}+\gamma_x u\frac{\partial w}{\partial x}+\frac{\gamma_z}{2}\frac{\partial ww}{\partial z}$$

III. DEPTH AVERAGE VELOCITY

The model is formulated using depth average velocity as its variable, where according to Dean (1991), the horizontal depth average velocity is,

$$U=\frac{1}{\beta_u D}\int_{-h}^{\eta}u\ dz \qquad \text{...........(4)}$$

U = horizontal depth average velocity
β_u = the horizontal velocity integration coefficient
$D=h+\eta$
D = total water depth
h = water depth towards still water level (Fig. 1)
η = surface water level towards still water level (Fig.1)

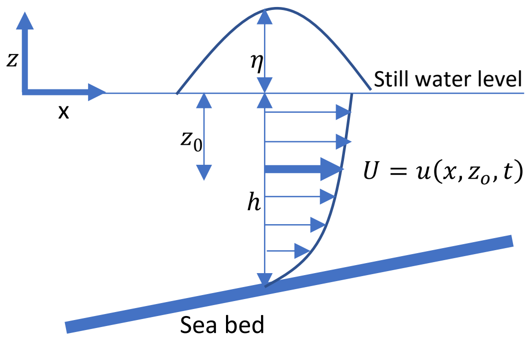

Fig (1). Depth average velocity concept

Equation (4) was initially formulated to model very long waves, such as tidal waves, using a horizontal velocity integration coefficient $\beta_u=1$. In this study, the integration coefficient is calculated by defining the depth-averaged velocity as the velocity at a depth $z=z_0$ below the still water level. Here, z_0 is negative, as shown in Figure 1. Consequently, z_0 is defined in terms of the water depth h, specifically $z_0=-\xi h$, where $0<\xi<1$.

The velocity potential equation solution of Laplace equation is

$$\phi(x,z,t)=G(\cos kx+\sin kx)\cosh k(h+z)\sin\sigma t$$

G is wave constant
k is wave number
σ is angular frequency, $\sigma=\frac{2\pi}{T}$
T is wave period.

a. Coefficients of Integration β_u and β_w

Horizontal water particle velocity from velocity potential is

$$u(x,z,t)=-\frac{\partial\phi}{\partial x}=-Gk(-\sin kx+\cos kx)\cosh k(h+z)\sin\sigma t$$

Vertical water particle velocity is

$$w(x,z,t)=-\frac{\partial\phi}{\partial z}=-Gk(\cos kx+\sin kx)\sinh k(h+z)\sin\sigma t$$

Based on the definition of the horizontal depth average velocity,

$$U=u(x,-\xi h,t)=-Gk(-\sin kx+\cos kx)\cosh kh(1-\xi)\sin\sigma t$$

Thus,

$$\frac{u}{U}=\frac{\cosh k(h+z)}{\cosh kh\,(1-\xi)}$$

Equation (4) is written into the equation for β_u,

$$\beta_u=\frac{1}{UD}\int_{-h}^{\eta}u\,dz$$

$$\beta_u=\frac{1}{D\cosh kh(1-\xi)}\int_{-h}^{\eta}\cosh k(h+z)\ dz$$

$$\beta_u=\frac{\sinh k(h+\eta)}{kD\cosh kh(1-\xi)}$$

$$\beta_u=\frac{\sinh kD}{kD\cosh kh(1-\xi)}$$

In deep water, $kD\approx kh=\theta\pi$, θ is referred to as the deep water coefficient where $\tanh\theta\pi=1$, and $\theta=1.70$ is used in this research

$$\beta_u=\frac{\sinh\theta\pi}{\theta\pi\cosh\theta\pi(1-\xi)} \qquad \text{.....(5)}$$

Although this equation is formulated in deep water, it also applies to shallow water, given the law of conservation of wave number (Hutahaean (2024b)) , where

$$\frac{\partial k(h+z)}{\partial x}=0$$

Thereby $k(h+z)$ is constant, unchanged against changes in water depth, as well as $k(h+\eta)$ is constant .

The integration coefficient of the vertical depth average velocity β_w , is formulated in the same way,

$$\beta_w=\frac{1}{DW}\int_{-h}^{\eta}w\ dz$$

$$\beta_w=\frac{1}{D\sinh kh(1-\xi)}\int_{-h}^{\eta}\sinh k(h+z)\,dz$$

$$\beta_w=\frac{\cosh kD-1}{kD\sinh kh(1-\xi)}$$

$$\beta_w=\frac{\cosh\theta\pi-1}{\theta\pi\sinh\theta\pi(1-\xi)} \qquad \text{......(6)}$$

b. Transformation coefficients

In the derivation of equations for water surface elevation and water particle velocity, variables for surface water particle velocities, namely horizontal velocity u_η and vertical velocity w_η, are introduced. To apply these equations more broadly, it is necessary to transform these surface velocities into depth-averaged velocities.
Using the definition of the depth average velocity,

$$\alpha_{u\eta}=\frac{u_\eta}{U}=\frac{\cosh k(h+\eta)}{\cosh kh(1-\xi)}=\frac{\cosh \theta\pi}{\cosh \theta\pi(1-\xi)}$$

Or

$u_\eta=\alpha_{u\eta}U$

Where the transformation coefficient $\alpha_{u\eta}$ is,

$$\alpha_{u\eta}=\frac{\cosh\theta\pi}{\cosh\theta\pi(1-\xi)} \qquad \text{........(7)}$$

Since $u_\eta u_\eta$ and $u_\eta u_\eta u_\eta$ is derived from u_η Thus its distribution over space and time is the same as u_η. Therefore, its transformation coefficient is the same as the transformation coefficient of u_η.

$u_\eta u_\eta=\alpha_{u\eta}UU$

$u_\eta u_\eta u_\eta=\alpha_{u\eta}UUU$

The vertical velocity transformation coefficient is

$$\alpha_{w\eta}=\frac{w_\eta}{W}=\frac{\sinh\theta\pi}{\sinh\theta\pi(1-\xi)} \qquad \text{.........(8)}$$

A relationship is obtained,

$w_\eta=\alpha_{w\eta}W$

$w_\eta w_\eta=\alpha_{w\eta}WW$

$w_\eta w_\eta w_\eta=\alpha_{w\eta}WWW$

In this study $\theta=1.70$, $\xi=0.32$, are used, with

$\beta_u=1.033$, $\alpha_{u\eta}=5.52$, $\alpha_{w\eta}=5.53$

The effect of θ value is that the larger the θ value, the deeper the breaker depth and vice versa, the smaller the θ value, the smaller the breaker depth, but has no effect on the breaker height value.

IV. THE CONSERVATION EQUATIONS

4.1.Weighted continuity equation.

The continuity equation is formulated using the weighted Taylor series and by working on the conservation of mass principle,,

$$\gamma_x\frac{\partial u}{\partial x}+\gamma_z\frac{\partial w}{\partial z}=0 \qquad \text{......(9)}$$

This equation is formulated under the condition that horizontal particle velocity only changed on the horizontal axis, as well as vertical particle velocity only changes on the vertical axis.

4.2. Kinetic Energy Conservation Equation

The kinetic energy conservation equation is formulated by reviewing the inflow and outflow of kinetic energy in a control volume. In the moving fluid mass contained kinetic energy Thus in the flow of the fluid mass there is also a flow of kinetic energy. The horizontal kinetic energy flow is $u(\rho E_{kx})$ and the vertical kinetic energy flow is $w(\rho E_{kz})$, where the kinetic energy on the horizontal axis is $E_{kx}=\frac{u^2}{2g}$ while the kinetic energy on the vertical axis is $E_{kz}=\frac{w^2}{2g}$, ρ is the mass density of water. To formulate the kinetic energy conservation equation, the control volume in Fig (2) is used.

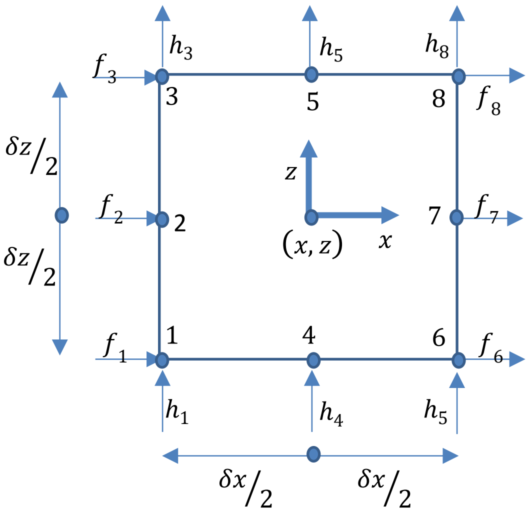

Fig (2). Control volume.

a. Space Averaging

The velocity distribution on the sides of the control volume is not uniform, so an average velocity that represents the flow velocity on each side is required.

Defined as

$f(x,z,t)=u(\rho E_{kx})$

$h(x,z,t)=w(\rho E_{kz})$

The horizontal kinetic energy input to the control volume through side $\overline{123}$ at a time $t=t$, is

$$f_1=f\left(x-\frac{\delta x}{2},z-\frac{\delta z}{2},t\right)$$
$$=f(x,z,t)-\gamma_x\frac{\delta x}{2}\frac{\partial f}{\partial x}-\gamma_z\frac{\delta z}{2}\frac{\partial f}{\partial z}$$

$$f_2=f\left(x-\frac{\delta x}{2},z,t\right)=f(x,z,t)-\gamma_x\frac{\delta x}{2}\frac{\partial f}{\partial x}$$

$$f_3=f\left(x-\frac{\delta x}{2},z+\frac{\delta z}{2},t\right)$$
$$=f(x,z,t)-\gamma_x\frac{\delta x}{2}\frac{\partial f}{\partial x}+\gamma_z\frac{\delta z}{2}\frac{\partial f}{\partial z}$$

The kinetic energy input rate on the $\overline{123}$ side is defined as

$$f_{input}=\frac{f_1+f_2+f_3}{3}$$

Substitution of the equations of f_1, f_2 and f_3 obtained

$$f_{input}=f_2=f\left(x-\frac{\delta x}{2},z,t\right)$$
$$=f(x,z,t)-\gamma_x\frac{\delta x}{2}\frac{\partial f}{\partial x}$$

Using the same method, the following was obtained

$$f_{output}=f_7=f\left(x+\frac{\delta x}{2},z,t\right)=f(x,z,t)+\gamma_x\frac{\delta x}{2}\frac{\partial f}{\partial x}$$

$$h_{input} = h_4 = h\left(x, z - \frac{\delta z}{2}, t\right) = h(x,z,t) - \gamma_z \frac{\delta z}{2}\frac{\partial h}{\partial z}$$

$$h_{output} = h_5 = h\left(x, z + \frac{\delta z}{2}, t\right) = h(x,z,t) + \gamma_z \frac{\delta z}{2}\frac{\partial h}{\partial z}$$

b. Time averaging

The inflow and outflow of kinetic energy is observed at a very small time interval δt. At that time interval, although very small, there is certainly a change in velocity. Therefore, an average velocity that represents the velocity at the time interval δt is required. Defined the average velocity at the time interval from $t = -\frac{\delta t}{2}$ ke $t = \frac{\delta t}{2}$ is,

$$\bar{f_t} = \frac{f\left(x,z,t-\frac{\delta t}{2}\right) + f(x,z,t) + f\left(x,z,t+\frac{\delta t}{2}\right)}{3}$$

Using the weighted Taylor series, the following was obtained

$$f_t = f(x,z,t)$$

Thus, for the inflow outflow process at an interval of δt, the velocity at time $t = t$ can be used.

The kinetic energy inflow-outflow at time interval δt is

$$IO = (f_{input} - f_{output})\delta z\,\delta t + (h_{input} - h_{output})\delta x\,\delta t$$

By working out the input and output equations on the sides of the control volume that has been formulated, the followings are obtained

$$IO = \left(-\gamma_x \delta x \frac{\partial f}{\partial x}\right)\delta z \delta t + \left(-\gamma_z \frac{\partial h}{\partial z}\right)\delta x \delta t$$

The inflow-outflow causes a change in kinetic energy in the control volume,

$$\delta E_k = (\delta E_{kx} + \delta E_{kz})\rho \delta x \delta z$$

The principle of conservation of energy,

$$(\delta E_{kx} + \delta E_{kz})\rho \delta x \delta z = \left(-\gamma_x \delta x \frac{\partial f}{\partial x}\right)\delta z \delta t + \left(-\gamma_z \frac{\partial h}{\partial z}\right)\delta x \delta t$$

The substitute the definition of f and h and work on the assumption of incompressible flow are

$$(\delta E_{kx} + \delta E_{kz})\rho \delta x \delta z = \left(-\gamma_x \delta x \rho \frac{\partial u E_{kx}}{\partial x}\right)\delta z \delta t + \left(-\gamma_z \rho \frac{\partial w \rho E_{kz}}{\partial z}\right)\delta x \delta t$$

Both parts of the equation are divided by $\rho \delta x \delta z \delta t$, and worked out at very small δt close to zero,

$$\frac{\partial E_{kx}}{\partial t} + \frac{\partial E_{kz}}{\partial t} = -\gamma_x \frac{\partial u E_{kx}}{\partial x} - \gamma_z \frac{\partial w E_{kz}}{\partial z} \qquad \ldots\ldots.(10)$$

This equation is the kinetic energy conservation equation.

4.3. Euler's momentum conservation equation in horizontal direction.

By using the weighted Taylor series and by using the same fluid flow conditions as the continuity equation formulation where horizontal velocity only changes in the horizontal axis and vertical velocity only changes in the vertical axis, Hutahaean (2024a) obtained Euler's momentum conservation equation in the horizontal direction is,

$$\gamma_{t,3}\frac{\partial u}{\partial t} + \frac{\gamma_x}{2}\frac{\partial uu}{\partial x} = -\gamma_{t,3}\frac{\partial}{\partial x}\int_z^\eta \frac{\partial w}{\partial t}dz - \frac{\gamma_z}{2}\frac{\partial}{\partial x}(w_\eta w_\eta - ww) - g\frac{\partial \eta}{\partial x} \qquad \ldots\ldots.(11)$$

V. VERTICAL WATER PARTICLE VELOCITY EQUATION.

Vertical water particle velocity equation is formulated by integrating the continuity equation with respect to water depth.

$$\gamma_x \int_{-h}^{\eta} \frac{\partial u}{\partial x}dz + \gamma_z w_\eta - \gamma_z w_{-h} = 0$$

This equation is written as an equation for w_η where the bottom vertical water particle velocity is ignored,

$$w_\eta = -\frac{\gamma_x}{\gamma_z}\int_{-h}^{\eta}\frac{\partial u}{\partial x}dz$$

Integration of the right-hand segment is solved by Leibniz Integration (Protter, Murray, Morrey, & Charles, 1985)

$$\int_\alpha^\beta \frac{\partial f}{\partial x}dz = \frac{\partial}{\partial x}\int_\alpha^\beta f\,dz - f_\beta \frac{\partial \beta}{\partial x} + f_\alpha \frac{\partial \alpha}{\partial x}$$

$$\int_{-h}^{\eta}\frac{\partial u}{\partial x}\,dz = \frac{\partial}{\partial x}\int_{-h}^{\eta} u\,dz - u_\eta \frac{\partial \eta}{\partial x} - u_{-h}\frac{\partial h}{\partial x}$$

The integration of the first term of the right segment is solved by the depth average velocity concept and the bottom horizontal water particle velocity is ignored and substituted into the vertical velocity equation,

$$w_\eta = -\frac{\gamma_x}{\gamma_z}\left(\beta_u \frac{\partial UD}{\partial x} - u_\eta \frac{\partial \eta}{\partial x}\right)$$

Transformation into depth average velocity equation,

$$W = -\frac{\gamma_x}{\alpha_{w\eta}\gamma_z}\left(\beta_u \frac{\partial UD}{\partial x} - \alpha_{u\eta} U \frac{\partial \eta}{\partial x}\right) \qquad \ldots\ldots(12)$$

Where,

$D = h + \eta$ is the total water depth. The coefficient β_u, defined in Equation (5). The coefficient $\alpha_{w\eta}$ outlined in Equation (8), serves as the transformation coefficient from surface vertical water particle velocity to depth-averaged vertical water particle velocity. Similarly, $\alpha_{u\eta}$ specified in Equation (7) is the transformation coefficient from surface horizontal water particle velocity to depth-averaged horizontal water particle velocity.

VI. WATER SURFACE ELEVATION EQUATION.

Water surface elevation equation is formulated by using Kinematic Free Surface Boundary Condition and kinetic energy conservation equation.

6.1.Kinematic Free Surface Boundary Condition.

Weighted kinematic water particle velocity is

$$w_\eta = \gamma_{t,2}\frac{\partial\eta}{\partial t} + \gamma_x u_\eta \frac{\partial\eta}{\partial x}$$

Written as water surface elevation equation,

$$\frac{\partial\eta}{\partial t} = \frac{1}{\gamma_{t,2}}\left(w_\eta - \gamma_x u_\eta \frac{\partial\eta}{\partial x}\right)$$

Added with depth average velocity variable, the water surface elevation equation becomes,

$$\frac{\partial\eta}{\partial t} = \frac{1}{\gamma_{t,2}}\left(\alpha_{w\eta} W - \gamma_x\, \alpha_{u\eta} U \frac{\partial\eta}{\partial x}\right) \qquad ......(13)$$

6.2. Integration of the conservation of energy equation.

The energy conservation equation is multiplied by dz and integrated over the water depth,

$$\frac{1}{2g}\left(\int_{-h}^{\eta}\frac{\partial uu}{\partial t}dz + \int_{-h}^{\eta}\frac{\partial ww}{\partial t}dz\right) =$$
$$\frac{1}{2g}\left(-\gamma_x\int_{-h}^{\eta}\frac{\partial uuu}{\partial x}dz - \gamma_z\left(w_\eta^3 - w_{-h}^3\right)\right)$$

Although there is an element of $\frac{1}{2g}$, in both segments of the equation, it cannot be removed, this is to keep the unit of the equation the same as the unit of the Kinematic Free Surface Boundary Condition, which is m/sec.

The integration is solved by Leibniz integration method and by working on the concept of depth average velocity and bottom water particle velocity is ignored,

$$\lambda\frac{\partial\eta}{\partial t} = \frac{1}{2g}\left(-\frac{\partial UU}{\partial t} - \frac{\beta_w}{\beta_u}\frac{\partial WW}{\partial t} - \frac{\gamma_x}{\beta_u D}\left(\beta_u\frac{\partial U^3 D}{\partial x} - \alpha_{u\eta}U^3\frac{\partial\eta}{\partial x}\right) - \frac{\gamma_z\alpha_{w\eta}}{\beta_u D}W^3\right)$$

Where,

$$\lambda == \frac{\left((\beta_u - \alpha_{u\eta})\frac{UU}{2g} + (\beta_w - \alpha_{w\eta})\frac{WW}{2g}\right)}{\beta_u D}$$

The water surface change equation is the sum of the water surface change from the Kinematic Free Surface Boundary Condition and the water surface elevation equation change from the energy conservation equation.

$$(1+\lambda)\frac{\partial\eta}{\partial t} = \frac{1}{\gamma_{t,2}}\left(\alpha_{w\eta}W - \gamma_x\,\alpha_{u\eta}U\frac{\partial\eta}{\partial x}\right)$$
$$-\frac{1}{2g}\left(\frac{\partial UU}{\partial t} + \frac{\beta_w}{\beta_u}\frac{\partial WW}{\partial t} + \frac{\gamma_x}{\beta_u D}\left(\beta_u\frac{\partial U^3 D}{\partial x} - \alpha_{u\eta}U^3\frac{\partial\eta}{\partial x}\right) + \frac{\gamma_z\alpha_{w\eta}}{\beta_u D}W^3\right) \qquad ....(14)$$

Equation (14) is the final water surface elevation equation of the water surface elevation equation. In the right segment of the equation there is a change in kinetic energy which is the source of energy for the change in potential energy in the left segment, Thus this equation can be called the energy conservation equation, which is a balance equation between changes in potential energy and changes in kinetic energy.

VII. HORIZONTAL WATER PARTICLE VELOCITY EQUATION.

Equation (11) is worked out on the surface at $z = \eta$,

$$\gamma_{t,3}\frac{\partial u_\eta}{\partial t} + \frac{\gamma_x}{2}\frac{\partial u_\eta u_\eta}{\partial x} = -g\frac{\partial\eta}{\partial x}$$

By using variable depth average velocity,

$$\gamma_{t,3}\alpha_{u\eta}\frac{\partial U}{\partial t} + \frac{\gamma_x\alpha_{u\eta}}{2}\frac{\partial UU}{\partial x} = -g\frac{\partial\eta}{\partial x} \qquad ....(15)$$

VIII. NUMERICAL METHOD

The space differential is solved by the Finite Difference Method while the time differential is solved by the predictor-corrector method. Details of the numerical methods as used by Hutahaean (2024a).

IX. MODEL OUTCOME

a. Wilson's Criteria (1963)

Wilson (1963) categorized wave profiles based on the ratio of wave crest elevation to wave height (Fig (3)). The wave profiles based on the comparison numbers are presented in Table (3).

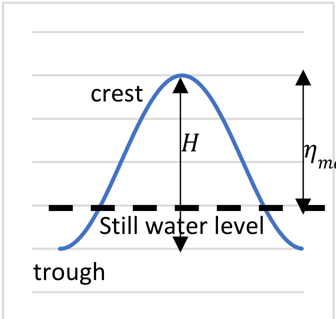

Fig (3). Water wave profile according to Wilson (1963).

Table (3) Water wave profile criteria (Wilson (1963))

Wave type	$\frac{\eta_{max}}{H}$
Airy/sinusoidal waves	< 0.505
Stoke's waves	$0.505 - 0.635$
Cnoidal waves	$0.635 - 1$
Solitary waves	$= 1$

a. Model execution at constant water depth..

In this section, the results of model execution at constant water depth (Fig (4)) are presented, with two water depths, $h = 20.0$ and $h = 8.0$ m.

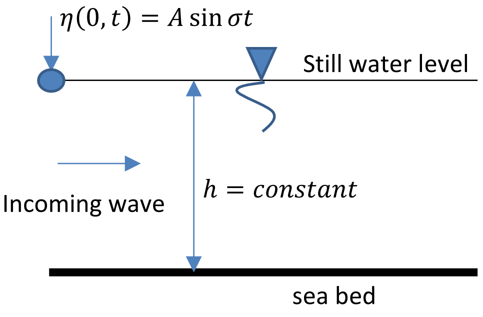

Fig (4). Constant water depth

As input, sinusoidal waves with the equation $\eta(0,t) = A\sin\sigma t$, is used, where $\sigma = \frac{2\pi}{T}$, T is the wave period, $T = 8.0$ sec. While wave amplitude A is used from 0.3-1.3 m, in order to obtain the types of wave profiles at various wave amplitudes.

a.1. Wave amplitude $A = 0.30$ m

The model execution results at $h = 20.0$ m is shown in Fig (5), where $\frac{\eta max}{H} = \frac{0.33}{0.6} = 0.55$, is quite close to Wilson's sinusoidal profile criteria. The model execution results at $h = 8.0$ m is presented in Fig (6), where $\frac{\eta max}{H} = \frac{0.37}{0.6} = 0.62$, which according to Wilson's criteria belongs to Stoke's profile.

On Stoke's profile, there is a deflection at the transition from wave crest to wave trough at $\eta \approx 0.0\ m$. The deflection can be the difference between sinusoidal profile and Stoke's profile. In the sinusoidal profile Fig (5), the deflection is actually visible but still very weak, the deflection can be eliminated by reducing the wave amplitude, thereby at deep water depth $h = 20.0$ m, wave amplitude $A = 0.30$ m is the transition limit from sinusoidal profile to Stoke's profile.

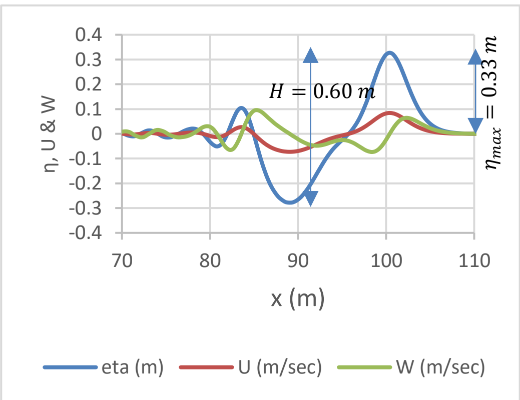

Fig (5). Sinusoidal wave profile, $A = 0.30\ m$, $h = 20.0\ m$

a.2. Wave amplitude $A = 0.60$ m

The model execution results at $h = 20.0$ m are presented in Fig (7), where $\frac{\eta max}{H} = \frac{0.70}{1.2} = 0.583$, which based on Wilson's criteria belongs to Stoke's profile. In addition, there is a deflection at the transition from wave crest to wave trough, this deflection is also found in the Stoke's profile in Fig. (6). Fig (8) presents the model execution results at water depth $h = 8.0$ m, where $\frac{\eta max}{H} = \frac{0.87}{1.2} = 0.725$, with the wave profile belonging to the cnoidal profile. Deflection changes to a small wave crest.

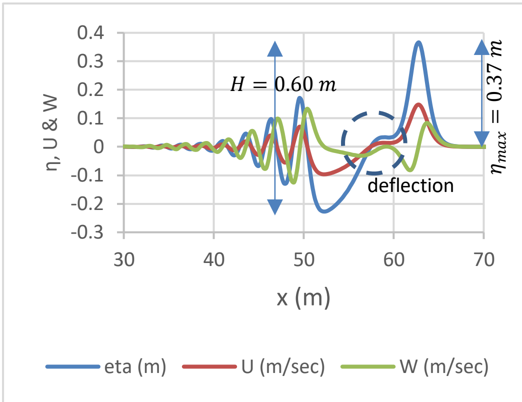

Fig (6). Stoke's wave profile, $A = 0.30\ m$, $h = 8.0\ m$

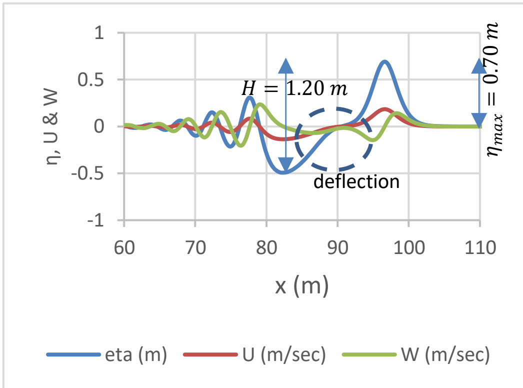

Fig (7). Stoke wave profile, $A = 0.60\ m$, $h = 20.0\ m$

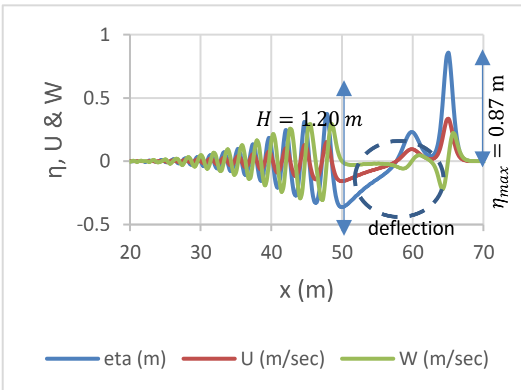

Fig (8). Cnoidal wave profile, $A = 0.60\ m$,

$h = 8.0\ m$

a.2. Wave amplitude $A = 1.30$ m

The model execution results at $h = 20.0$ m are shown in Fig (9), where $\frac{\eta_{max}}{H} = \frac{1.75}{2.5} = 0.7$ which according to Wilson's criteria belongs to the Cnoidal profile. The wave height is reduced from $H = 2.60\ m$ to $2.50\ m$, that is assumed due to deflection in the form of small wave. In Fig (10), the model execution results at water depth $h = 8.0\ m$ are presented, three wave crests are formed, the largest of which is the main wave. In this case, the main wave can be classified as a solitary wave with wave height $H = 2.20\ m$, considering that the entire wave body is above the still water level. There is a reduction in wave height because some of the wave energy is used to form two small waves, one of which has a solitary wave profile.

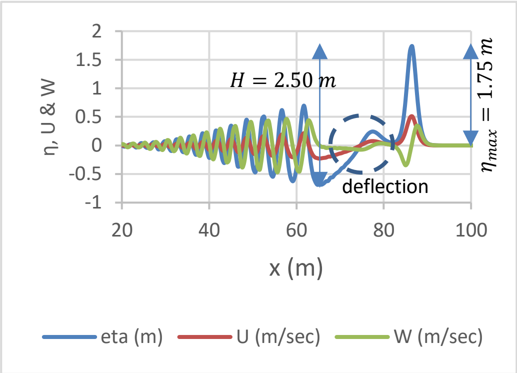

Fig (9). Cnoidal wave profile, $A = 1.30\ m$, $h = 20.0\ m$

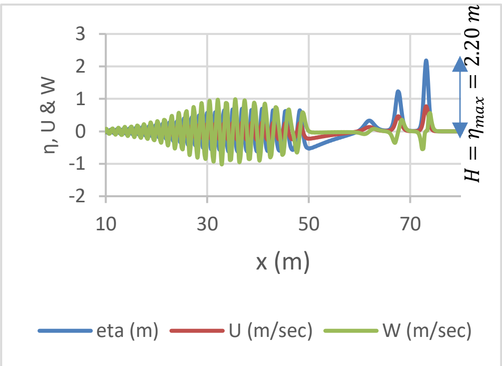

Fig (10). Solitary wave profile, $A = 1.30\ m$, $h = 8.0\ m$

The results from the model execution at a constant water depth revealed that sinusoidal wave profiles typically manifest in waves with small amplitudes. The formation of a wave profile is influenced by both the wave amplitude and the water depth. In deep water, a wave with a given amplitude might exhibit a sinusoidal profile, whereas the same amplitude in shallow water could result in a Stoke's profile. Conversely, a Stoke's profile in deep water may transition into a cnoidal profile in shallow waters, and a cnoidal profile in deep water can evolve into a solitary profile when the water depth decreases.

The distinction between a sinusoidal profile and a Stoke's profile is not only evident through the Wilson criteria but also by the characteristic deflection seen in the Stoke's profile, which appears as a flattened line at the transition from wave crest to wave trough. In contrast, in a cnoidal profile, this deflection manifests as small, gently sloping waves, and in a solitary profile, the deflection presents as two or more smaller waves.

Additionally, the primary wave is often accompanied by a tail wave or multiple secondary waves. The phenomena of shoaling and breaking of these secondary waves, which will be further discussed in the following section, are critical aspects of coastal wave dynamics.

b. Model execution at sloping bottom.

In this section, the model is executed on a sloping sea bed (Fig (11)), with water depth 15.0-1.0 m, bottom slope $\frac{14.0}{150.0} = 0.093$.

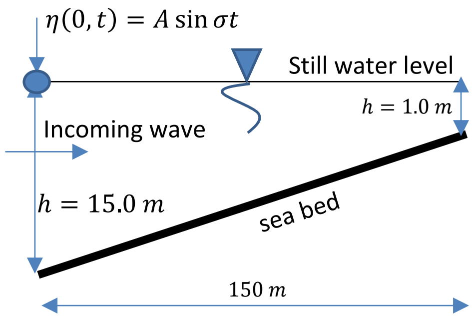

Fig (11). Sloping sea bed

In the simulation, a wave with a period of 8 seconds and an amplitude of 1.00 meter was input. Unlike previous depictions, the simulation results for this sloping bottom scenario are presented with the water depth h on the abscissa, allowing for a clear visualization of the relationship between water depth and wave characteristics. The waves transition from deep to shallow water, indicating that in the model, waves move from right to left.

The simulation was conducted until the main wave reached a water depth of approximately ≈ 1.3 m. The results are presented in Figure (12) and Figure (13). At this depth $h \approx 1.3\ m$, the height of the main wave stabilizes at 0.6 meters, and the wave profile transitions to a solitary profile, as shown in Figure (13).

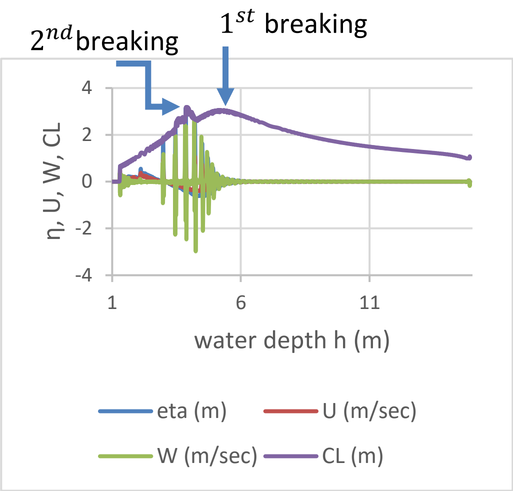

Fig (12). Wave condition after breaking.

Notes: CL (Crest Line) is the line that connects the maximum water level elevation along the wave trajectory. In Figure 12, it is apparent that there are two breaking events; however, there are actually more than two, as will be demonstrated in the next section (Figure 14). The first breaking event, which occurs at greater water depths, involves the main wave, while the second event, occurring in shallower waters, involves the breaking of the tail wave or secondary wave.

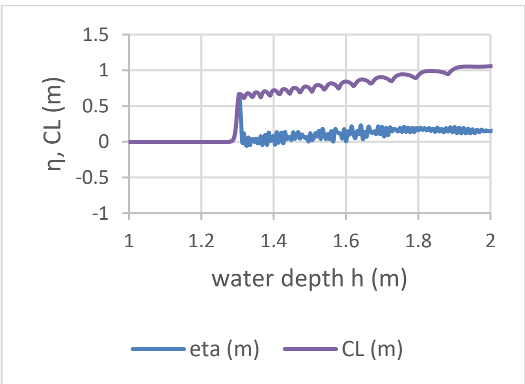

Fig (13). Main wave profile at water depth $\approx 1.3\ m$

The wave condition after the first breaking in the surf zone is highly unstable, as observed in the unstable crest line (Fig. (13) and Fig. (14)). Wave instability in the surf zone is a well-documented phenomenon. Within this zone, the secondary wave experiences breaking, which is depicted in Fig.(14), where two breakings occur in two secondary waves. The wave profile is a solitary profile, as shown in Fig.(15).

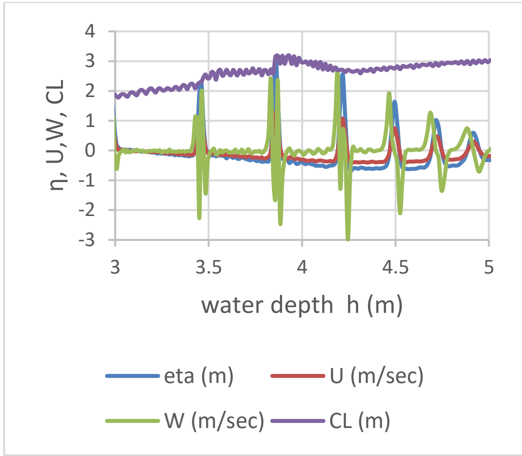

Fig (14). Breaking of the secondary wave.

There are 3 breaking points with 3 breaking conditions, namely :

a. Main wave breaking, $H_{br} = 3.06$ m ,

$h_{br} = 5.17$ m, $\frac{H_{br}}{h_{br}} = 0.59$

b. 1st secondary wave breaking 1 $H_{br} = 3.19$ m,

$h_{br} = 3.87$ m, $\frac{H_{br}}{h_{br}} = 0.82$

c.2nd secondary wave breaking $H_{br} = 2.3$ m ,

$h_{br} = 3.45$ m, $\frac{H_{br}}{h_{br}} = 0.67$

Breaker height as suggested by Komar and Gaughan (1972) is:

$$H_{br} = 0.39\ g^{1/5}(T_0 H_0^2)^{2/5} \qquad .....(16)$$

Where $T_0 = 8.0$ sec., $H_0 = 2.00$ m, $g = 9.81$ m/sec^2 obtain $H_{br} = 2.46$ m. The closest model result is the 2nd secondary breaking wave $H_{br} = 2.2$ m.

Breaker depth index from Mc Cowan (1894),

$$\frac{H_{br}}{h_{br}} = 0.78 \qquad .....(17)$$

The closest model result is the breaking of the 1st secondary wave $\frac{H_{br}}{h_{br}} = 0.82$.

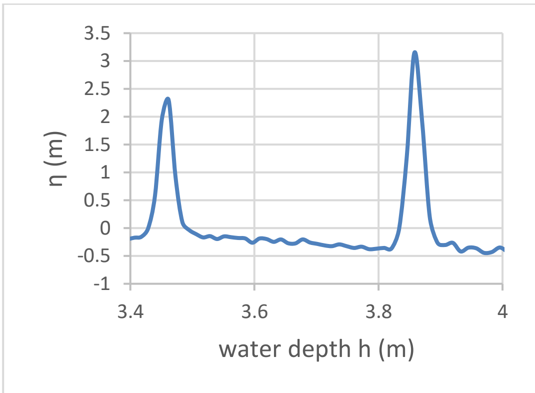

Fig (15). Breaking wave profile of the secondary wave.

Next, the breaking condition of the main wave is shown (Fig. (16)) with the wave profile being a solitary profile, Fig. (17).

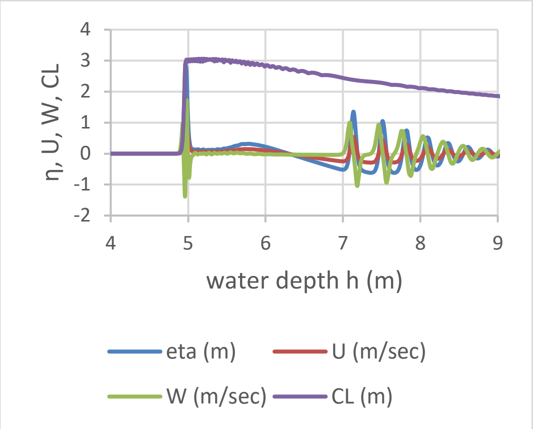

Fig (16). The breaking condition of the main wave.

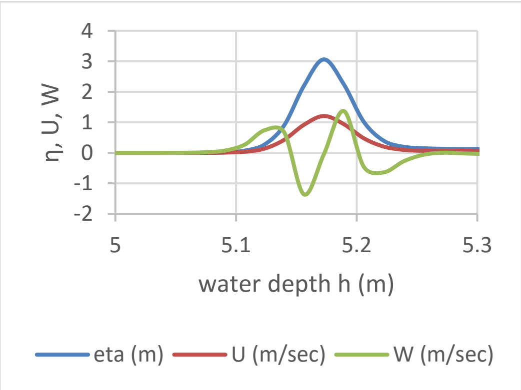

Fig (17). Wave profile of the main wave at the breaking point.

The model results from the sloped bottom indicate that it can effectively simulate the shoaling-breaking process and subsequent movement in very shallow water depths. The simulation identifies three types of breaking waves: a primary breaking wave and two secondary breaking waves, with the wave profile adopting a solitary shape at the moment of breaking. If the simulation continues, there may be additional breakings, such as a fourth and fifth wave.

Additionally, the model reveals a significant increase in vertical water particle velocity at the point of breaking. According to the continuity equation, a decrease in water depth leads to a greater disparity between input and output in the horizontal direction, which, in turn, escalates the vertical velocity. Thus, there is a likelihood that wave breaking may occur when the vertical velocity becomes excessively high.

X. CONCLUSION

The study demonstrated that by incorporating Surface Kinematic Boundary Conditions as the water surface elevation equation and combining it with the kinetic energy conservation equation, a model was developed capable of simulating wave breaking until a reduction in wave height occurs in shallow water. This combination generates an equation that adheres to the energy conservation principle, establishing a balance between potential energy changes, indicated by variations in water surface elevation, and kinetic energy changes.

The model, with modifications to its calculation algorithm, consistently generates four distinct wave profiles according to wave height and water depth: sinusoidal, Stoke's, cnoidal, and solitary profiles. Overall, the model effectively simulates water wave mechanics in both deep and shallow water environments.

Future developments should focus on refining the estimation of breaker height and depth to align more closely with the results obtained from physical model studies conducted by previous researchers, as well as those derived from velocity potential theory.

REFERENCES

[1] Hutahaean, S. (2024a). Applying Weighted Taylor Series on Time Series Water Wave Modeling. International Journal of Advance Engineering Research and Science (IJAERS). Vol. 11, Issue 2; Feb, 2024, pp 38-47. Article DOI: https://dx.doi..org/10.22161/ijaers.112.6.

[2] Boussinesq, J. (1871) Theorie de l'intumescence liquede,aplelee onde ou de translation, se propageant dans un canal rectangulaire. Comptes Rendus de l'Academic des Sciences. **72**:755-759.

[3] Dingermans, M.W. (1997). Wave propagation over uneven bottom. Advances series on Ocean Engineering **13.** World Scientific, Singapore. ISBN 978-981-02-0427-3. Archived from the original on 2012-0-08. Retrieved 2008-01-21, Chapter 5.

[4] Hamm, L.; Madsen, P.A.; Peregrine, D.A. (1993). Wave transformation in the nearshore zone: A Review. Coastal Engineering. **21** (1-3):5-39. Doi:10.1016/0378-3839(93)90044-9.

[5] Johnson, R.S. (1997). A modern introduction to the mathematical theory ofwater waves. Cambridge Texts in Applied Mathematics. **19.** Cambridge University Press ISBN 0 521 59832 X.

[6]Kirby, J.T. (2003). Boussinesq Models and Applications to nearshore wave propagation, surfzone process and waves induced currents. In Lakhan, V.C. (ed). Advances in Coastal Modeling. Elsevier Oceanography Series.**67.** Elsevier, pp. 1-41. ISBN 0 444 51149 0.

[7] Peregrine, D.H. (1967). Long waves on a Beache. Journal of Fluid Mechanics. **27** (4): 815-824. Bibcode: 1967 JFM.....815P. doi:10.1017/S0022112067002605.

[8] Peregrine, D.H. (1972). Equations for water waves and the propagation approximations behind them. In Meyer, R.E.(ed). Wave on Beaches and Resulting Sediment Transport. Academic Press.pp.95-122. ISBN 0 12 493 250 9.

[9] Hutahaean, S., Achiari H. (2017). Non-Linear Water Wave Equation Time Series Formulated Using Velocity Equation as The Result of Laplace Equation. International Journal of Engineering Research and Application (IJERA). Vol. 7, Issue 6, Part (-3); June, 2017, pp 37-45.

[10] Hutahaean, S. (2019). A Continuity Equation For Time Series Water Wave Modeling Formulated Using Weighted Total Acceleration. International Journal of Advance Engineering Research and Science (IJAERS). Vol. 6, Issue 9; Sept, 2019, pp 148-153. Article DOI: https://dx.doi..org/10.22161/ijaers.69.16.

[11] Hutahaean, S. (2024b). Breaking Index Study on Weighted Laplace Equation. International Journal of Advance Engineering Research and Science (IJAERS). Vol. 11, Issue 1; Jan, 2024, pp 34-43. Article DOI: https://dx.doi..org/10.22161/ijaers.11.6.

[12] Hutahaean, S. (2023). Method for Determining Weighting Coefficients in Weighted Taylor Series Applied to Water Wave Modeling. International Journal of Advance Engineering Research and Science (IJAERS). Vol. 10, Issue 12; Dec, 2023, pp 105-114. Article DOI: https://dx.doi..org/10.22161/ijaers.1012.11.

[13] Dean, R.G., Dalrymple, R.A. (1991). Water wave mechanics for engineers and scientists. Advance Series on Ocean Engineering.2. Singapore: World Scientific. ISBN 978-981-02-0420-4. OCLC 22907242.

[14] Protter, Murray, H.; Morrey, Charles, B. Jr. (1985). Differentiation Under The Integral Sign. Intermediate Calculus (second ed.). New York: Springer pp. 421-426. ISBN 978-0-387-96058-6.

[15] Wilson, B.W. (1963). Condition of Existence for Types of Tsunami Waves, paper presented at XIIIth Assembly IUGG, Berkeley, California, August 1963 (unpublish).

[16] Komar, P.D. & Gaughan M.K. (1972). Airy Wave Theory and Breaker Height Prediction, Coastal Engineering Proceedings, 1 (13).

[17] Mc Cowan, J. (1894). On the highest waves of a permanent type, Philosophical Magazine, Edinburgh 38, 5th Series, pp. 351-358.

International Journal of Advanced Engineering Research and Science (IJAERS)
Peer-Reviewed Journal
ISSN: 2349-6495(P) | 2456-1908(O)
Vol-11, Issue-5; May, 2024
Journal Home Page Available: https://ijaers.com/
Article DOI: https://dx.doi.org/10.22161/ijaers.115.2

Assessing Solar Tracker Effectiveness in Diverse Weather Conditions

Amol Prakash[1*], Kamlesh Lal[2], Maneesh[2]

[1]Department of Renewable Energy Engineering, Vaugh Institute of Agricultural Engineering and Tehnology, SHUATS, Uttar Pradesh, India
[2]Department of Farm Machinery and Power Engineering, Vaugh Institute of Agricultural Engineering and Tehnology, SHUATS, Uttar Pradesh, India

Received: 011 Mar 2024,
Receive in revised form: 25 Apr 2024,
Accepted: 07 May 2024,
Available online: 12 May 2024

***Keywords*— Solar panel, Tracking, Non-tracking, Power, Single Axis solar tracking Mechanism**

***Abstract*— *Solar tracking systems aim to optimize solar photovoltaic (PV) panel efficiency by maximizing exposure to sunlight. This paper explores solar tracking, its benefits, and various system types, emphasizing the goal of ensuring panels are perpendicular to the sun's rays. Tracking enhances energy generation potential compared to fixed installations, increasing output by 25-35%. This boosts return on investment and reduces payback periods. In agriculture, solar tracking promotes energy efficiency, productivity, and sustainability. However, long-term benefits, economic feasibility, and environmental impacts require further research. This study proposes evaluating solar panel output under different weather conditions, comparing tracking and non-tracking modes. The analysis concludes that tracking mode generates more power than non-tracking mode. This finding underscores the efficacy of solar tracking technology in maximizing energy production. Overall, adopting solar tracking systems can foster a greener, more sustainable future, particularly in agricultural contexts.*

I. INTRODUCTION

1.1 Solar Energy

The utilization of solar energy dates back millennia, with ancient civilizations such as the Greeks and Romans employing solar architecture to capture and utilize the sun's heat for various purposes [6]. Many early innovations laid the foundation for the solar technologies we have today. One of the most revolutionary developments in solar energy is the widespread adoption of photovoltaic (PV) technology. PV panels, often referred to as solar panels, convert sunlight directly into electricity through the photovoltaic effect [3]. This innovation has transformed the energy landscape by making solar power accessible and economically viable on a large scale. Over the years, intensive research and development efforts have significantly improved the efficiency of solar panels. Breakthroughs in materials science, such as the development of perovskite solar cells, promise even greater efficiency gains in the future [7]. Enhanced efficiency translates into more power generation from the same area of solar panels, making solar energy a compelling choice for meeting energy demands. As solar energy capacity increases, grid integration and energy storage solutions become critical. Research in this area has led to innovations like smart grids, which enable efficient distribution and management of solar-generated electricity [5]. Moreover, energy storage technologies like lithium-ion batteries are making it possible to store excess solar energy for use during cloudy days or at night.

Solar energy is not only economically viable but also environmentally friendly. It produces no greenhouse gas emissions during operation, reducing the carbon footprint associated with energy production [2]. The use of solar power contributes to mitigating climate change and reducing air pollution, thus enhancing overall environmental quality. Beyond its environmental advantages, solar energy also offers economic benefits. The solar industry has witnessed rapid growth, creating jobs and stimulating local economies [1]. As governments worldwide invest in renewable energy, solar power is increasingly becoming an engine for economic development. While solar energy holds tremendous promise, it is not without its challenges. Issues such as intermittency, land use, and the environmental impact of manufacturing PV panels require ongoing research and innovation [4]. Addressing these challenges will be crucial for the continued expansion of solar energy.

1.2 Single-Axis Solar Tracking Mechanism

The quest for sustainable energy sources has led to an unprecedented surge in research and innovation within the field of renewable energy. Solar power stands as one of the most promising and abundant sources of clean energy, offering immense potential for addressing our ever-growing energy needs while mitigating environmental concerns. To maximize the efficiency of solar energy conversion, solar tracking mechanisms have emerged as an essential component of solar photovoltaic systems. Among them, the Single Axis Solar Tracking Mechanism (SASTM) has gained substantial attention due to its cost-effectiveness and significant improvement in energy yield. In recent years, a multitude of research papers and studies have explored various aspects of Single Axis Solar Tracking Mechanisms, highlighting their importance in enhancing solar energy capture. These mechanisms operate by tilting solar panels or arrays along a single axis, typically the east-west axis, to follow the sun's daily path across the sky [8]. This movement ensures that the solar panels are optimally oriented to receive sunlight at nearly perpendicular angles, thereby increasing energy generation. Numerous research findings underscore the benefits of SASTMs.

Solar power occupies a significant position among global renewable energy sources due to its abundant energy eventuality. Accordingly, its donation to electricity generation is steadily adding . still, carrying peak effectiveness from fixed solar photovoltaic(PV) panels is a redoubtable task due to their limited capability to constantly tap into solar energy(10). To attack this issue and alleviate energy effectiveness losses, the application of solar shadowing systems has surfaced as an exceptionally effective result. These systems enable nonstop adaptation of the panels ’ position to align with the sun’s line, optimizing energy immersion and enhancing overall performance(8,9). Photovoltaic energy has shown a eventuality for cost reduction and better conversion effectiveness, and it's believed to come one of the primary source of energy force in the future [11]. solar energy is anticipated to come cheaper than conventional energy sources in the near future, due to two main factors nonstop development of photovoltaic technology, and fossil energies raising prices.

II. MATERIALS AND METHODS

2.1 Materials used:

Table 1. List of materials used in the fabrication

S. No.	Particular’s Name
1.	Solar panel
2	Arduino Uno
3	DC motor
4	LDR sensor
5	Resistance
6	Motor driver
7	Jumper wire
8	Battery
9	Digital Multimeter
10	Tilt sensor

2.2 Following Steps were taken for the fabrication and performance evaluation of SASTM

- Designing of the structure in autocad software
- Collecting different components as per the need of the project
- Fabrication of the basic supporting structure
- Feeding the program in Arduino uno through Arduino IDE
- Assembling of all the desired components on the structure i.e. solar panel, sensors, motor Battery, Arduino Uno
- Placing the project in direct solar radiation
- Measuring the amount of short–circuit current and open circuit – voltage with the help of a multimeter in different weather conditions (clear sky and cloudy sky) by tracking and non-tracking mechanism
- Calculating the Fill Fator (FF)
- Comparing different fill factors for different conditions

2.3 Designing of the structure in AutoCAD

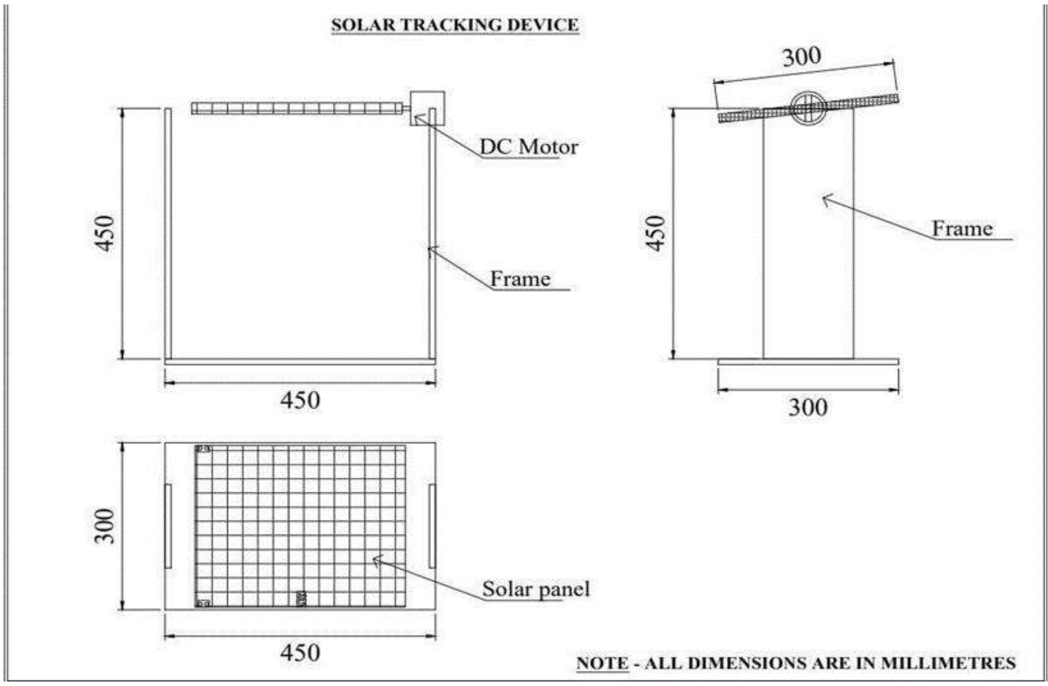

Fig.1. Structural of SASTM

2.4 Theoretical and Mathematical Background

2.4.1 Fill Fator (FF)

A solar photovoltaic module's efficiency is commonly measured by the Fill Factor (FF). It measures the real highest power that may be achieved [12]. The FF is described as the proportion of the highest power of the solar cell to the total(multiplication) of Voc and Isc, which are described as follows:

$$FF\ (\%) = (Pmax) / (V_{oc} \times I_{sc}) \quad (2.1)$$

2.4.2 Short Circuit Current (I_{sc})

Short circuit current, also known as "fault current" or "maximum fault current," refers to the maximum current that can flow through a circuit when a fault or short circuit occurs. A short circuit is an unintended connection between two conductors, typically with very low or zero resistance, which causes a significant increase in current flow. It is crucial for designing and protecting electrical systems, as it determines the magnitude of current that protective devices like circuit breakers or fuses need to handle [13].

2.4.3 Open Circuit Voltage (V_{oc})

Open circuit voltage, often abbreviated as "OCV" or "Voc," refers to the voltage across a circuit or component when there is no load or current flowing through it. In other words, it is the voltage measured across the terminals of a device when it is disconnected from any external circuit. It is an important parameter in understanding the behavior of power sources like batteries, solar cells, and generators. It represents the voltage potential of the source when no current is drawn from it [14].

III. RESULTS AND DISCUSSIONS

3.1. Observations recorded in clear sky & partially cloudy sky weather condition by tracking and non-tracking mechanism

Short circuit current & open circuit voltage had been measures with help of multimeter in different weather condition in tracking and non-tracking mechanism. The measure value is being discussed in following tables:

Table 1. Measurement of the (Voc) and (Isc) of solar panel in partially cloudy weather (non- tracking), Date- 2 august, 2023

S. No.	Time	Voltage (Voc)	Current (Isc)
1	10:00AM	19.67V	0.28A
2	11:00AM	19.72V	0.62A
3	12:00PM	18.65V	0.26A
4	01:00PM	19.85V	0.41A
5	02:00PM	18,54V	0.11A
6	03:00PM	18.74V	0.13A
7	04:00PM	18.74V	0.16A
8	05:00PM	18.26V	0.08A

Table 2. Measurement of the (Voc) and (Isc) of solar panel in partially cloudy weather (tracking), Date- 1 August, 2023

S. No.	Time	Voltage (voc)	Current (Isc)
1	10:00AM	19.65V	0.16A
2	11:00AM	19.48V	0.20A
3	12:00PM	18.36V	0.22A
4	01:00PM	19.07V	0.35A
5	02:00PM	19,44V	0.31A
6	03:00PM	19.57V	0.41A
7	04:00PM	17.86V	0.07A
8	05:00PM	17.56V	0.09A

Table 3. Measurements of the (Voc) and (Isc) of solar panel in clear sky (tracking), Date- 25 July, 2023

S. No.	Time	Voltage (voc)	Current (Isc)
1	10:00AM	19.24V	0.22A
2	11:00AM	19.79V	0.54A
3	12:00PM	19.44V	0.46A
4	01:00PM	19.86V	0.63A
5	02:00PM	19,40V	0.52A
6	03:00PM	19.05V	0.34A
7	04:00PM	19.62V	0.30A
8	05:00PM	19.17V	0.25A

Table 4. Measurement of the (Voc) and (Isc) of solar panel in clear sky (non- tracking), Date- 26 July, 2023

S. No.	Time	Voltage (Voc)	Current (Isc)
1	10:00AM	19.08V	0.11A
2	11:00AM	19.69V	0.22A
3	12:00PM	19.84V	0.09A
4	01:00PM	19.01V	0.30A
5	02:00PM	19,02V	0.21A
6	03:00PM	19.24V	0.25A
7	04:00PM	18.18V	0.18A
8	05:00PM	18.05V	0.15A

3.2 Calculation to find fill factor in different weather conditions by tracking and non-tracking mechanism

The fill factor is calculated by equation (1)

Table 5. Fill factor of the partially cloudy sky by the non-tracking mechanism

S.no	Time	Pidel (Voc× Ios)	FF(%)
1	10:00AM	5.50	16%
2	11:00AM	12.22	7%
3	12:00 PM	4.84	16%
4	01:00 PM	8.13	24%
5	02:00 PM	2.03	6%
6	03:00 PM	2.43	8%
7	04:00 PM	2.99	9%
8	05:00 PM	1.46	5%

Table 6. Fill factor of the partially cloudy sky by tracking mechanism

S. no	Time	Pidel (Voc× Ios)	FF(%)
1	10:00AM	3.14	9%
2	11:00AM	3.89	11%
3	12:00 PM	4.03	13%
4	01:00 PM	6.92	20%
5	02:00 PM	7.97	25%
6	03:00 PM	8.02	24%
7	04:00 PM	1.25	4%
8	05:00 PM	1.58	5%

Table 7. Fill factor for clear sky by tracking mechanism

S.no	Time	Pidel (Voc× Ios)	FF(%)
1	10:00AM	4.23	12%
2	11:00AM	10.68	30%
3	12:00 PM	1.15	26%
4	01:00 PM	12.51	37%
5	02:00 PM	10.08	20%
6	03:00 PM	1.71	18%
7	04:00 PM	1.99	17%
8	05:00 PM	1.56	14%

Table 8. Fill factor for clear sky by non-tracking

S.no	Time	Pidel ($Voc \times Ios$)	FF(%)
1	10:00AM	2.09	**6%**
2	11:00AM	4.33	**13%**
3	12:00 PM	9.12	**26%**
4	01:00 PM	6.65	**20%**
5	02:00 PM	5.89	**18%**
6	03:00 PM	4.81	**13%**
7	04:00 PM	3.27	**11%**
8	**05:00 PM**	**2.70**	**9%**

3.3Comparison of fill factor in different weather condition by (Tracking and Non-tracking) mechanism.

Table 9. Comparison of fill factor in clear sky by tracking and non-tracking

S. no.	FF(%) (non-tracking mechanism)	FF(%) (tracking mechanism)
1	6%	12%
2	13%	30%
3	26%	26%
4	24%	37%
5	18%	20%
6	14%	18%
7	11%	17%
8	9%	14%

Table 10. Comparison of fill factor in cloudy sky by tracking and non-tracking mechanism

S. no.	FF(%) (non-tracking mechanism)	FF(%) (tracking mechanism)
1	16%	9%
2	7%	11%
3	16%	13%
4	24%	20%
5	6%	25%
6	8%	24%
7	9%	4%
8	5%	5%

3.4 Graphical representation of comparison of fill factor for clear sky and cloudy sky (tracking mechanism) and clear sky and cloudy sky (non-tracking mechanism)

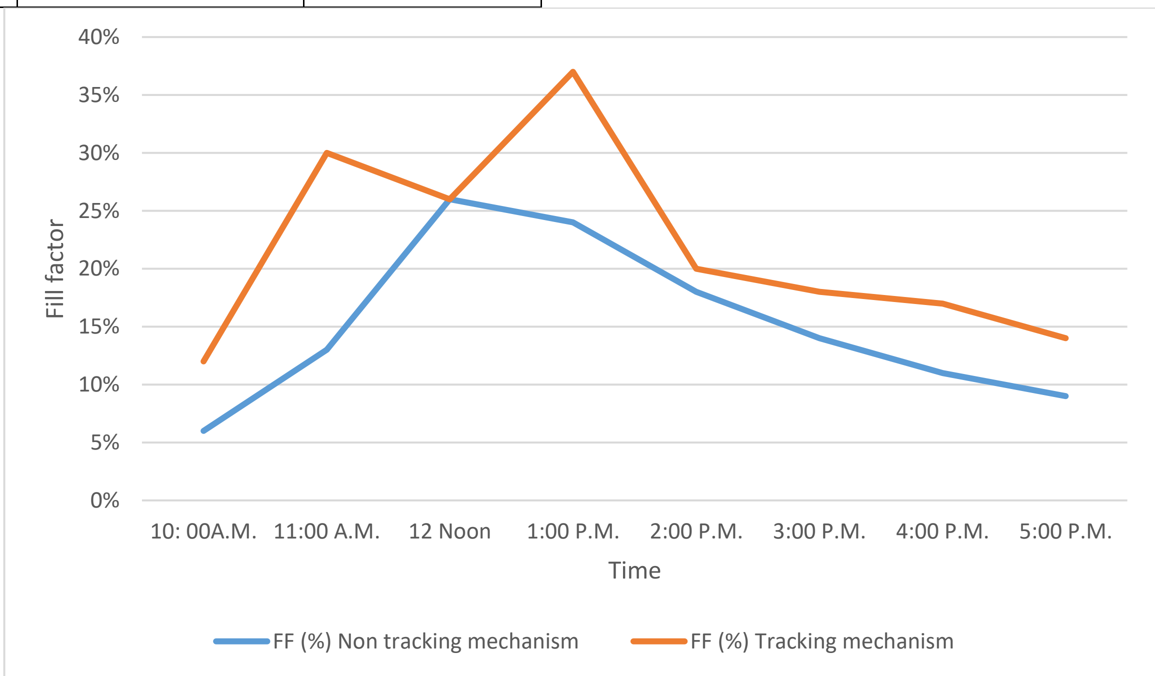

Fig.1. Comparative graph of fill factor in the clear sky by tracking and non-tracking mechanism

The values of fill factor is always high in clear sky by tracking mechanism where as the values of fill factor is always less in cloudy sky by non tracking for every interval of time. This is due to the fact that tracking the solar radiation will automatically increases the voltage and circuit generated by the solar panel

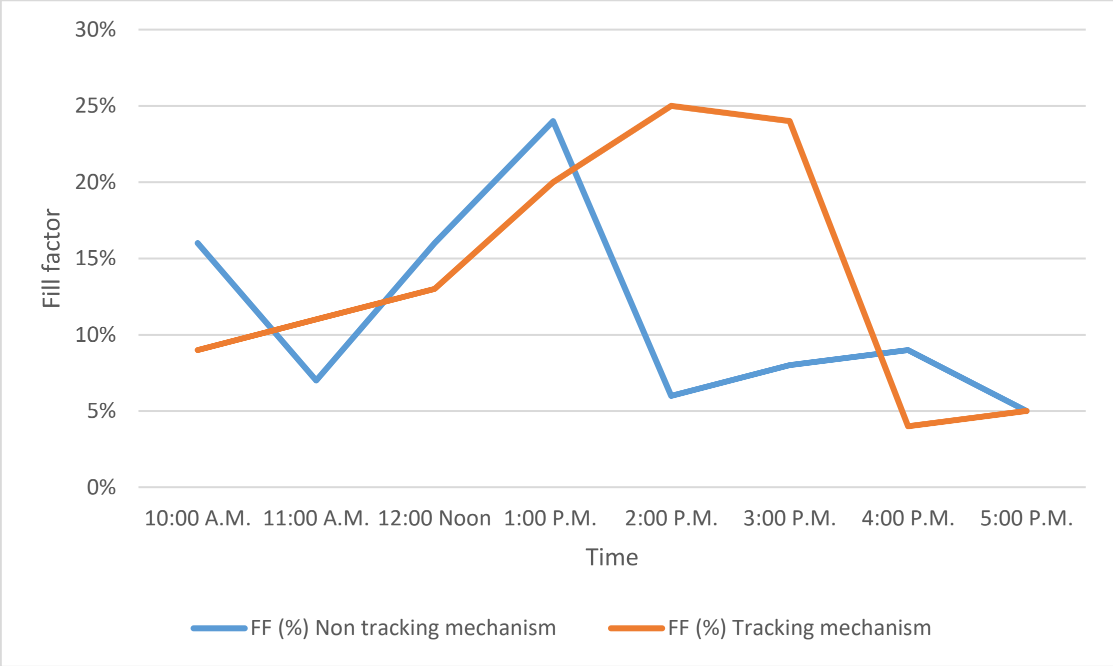

Fig. 2 Comparative graph of fill factor in partially cloudy sky by tracking and Non-tracking mechanism

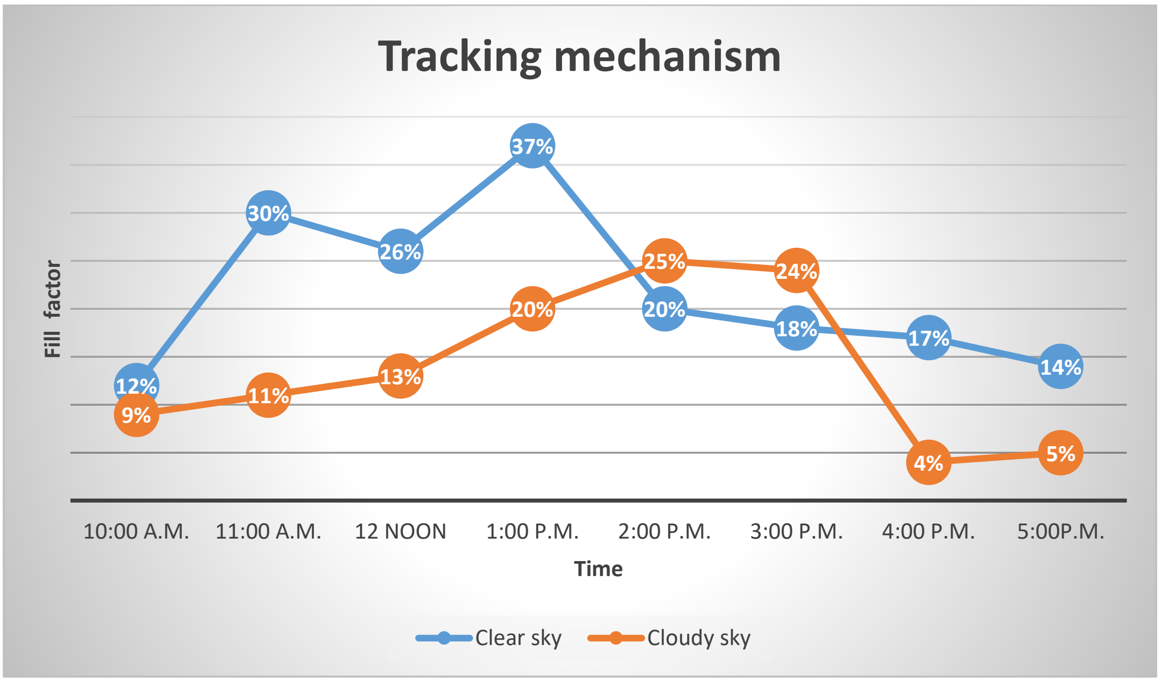

Fig.3 Comparative graph of fill factor in the clear sky and cloudy sky by tracking mechanism

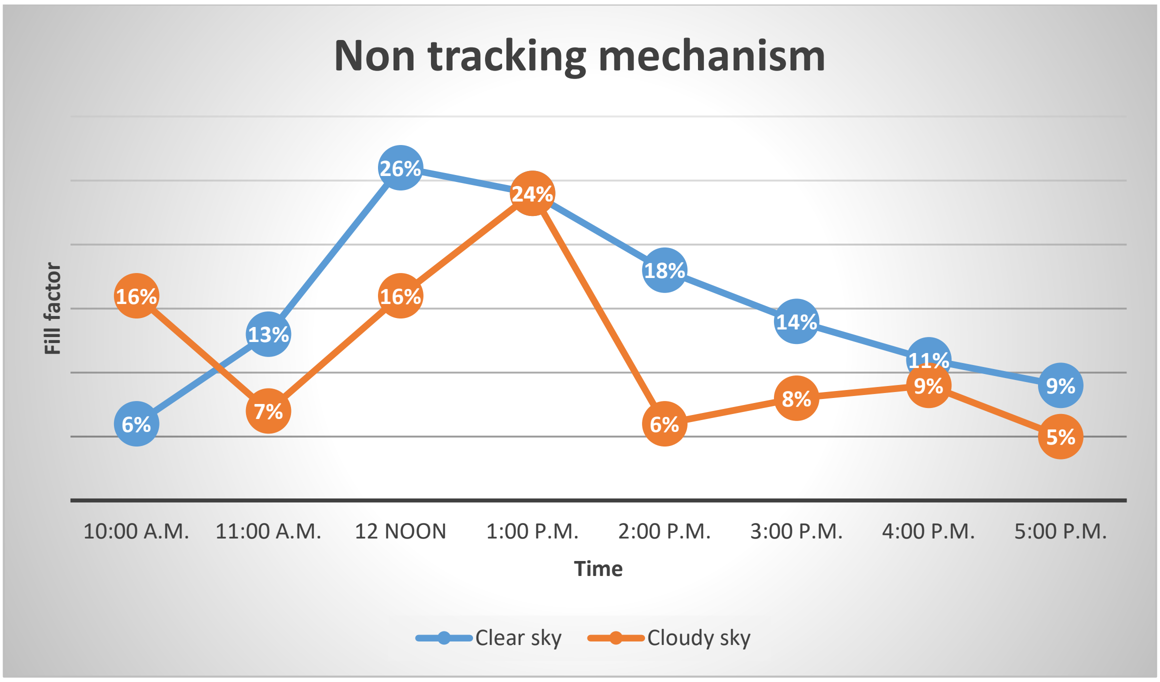

Fig.4 Comparative graph of fill factor in the clear sky and cloudy sky by Non tracking mechanism

IV. CONCLUSIONS

Fill factor has been calculated by observing different voltage and current in different weather condition on the basis of observation tables and graphical representation, this can be concluded that fill factor of clear sky weather is more in tracking condition, in compare to non-tracking condition. This simply means that energy conversion in tracking mode is higher than non-tracking mode. In case of partially cloudy sky, the fill factor has some randomness, that can be seen in table no.4 this is because there is variation in the amount of clouds and density of the clouds too.The maximum amount of voltage and current observed was 19.86V and current 0.63A respectively (Table 3) which was in clear sky weather (tracking mechanism)

ACKNOWLEDGMENTS

I extend my sincere gratitude to the Farm Machinery Department at SHUATS for their invaluable support and resources. I am deeply thankful for the opportunity to conduct research within such a prestigious institution. Additionally, I would like to express my appreciation for the research work mentioned in this paper, which has greatly contributed to the development of my own study. Your dedication and contributions have been instrumental in shaping the outcomes of this research endeavor. Thank you for your unwavering support and guidance throughout this journey.

REFERENCES

[1] Bennett, D. (2020). The economic impacts of COVID-19 on the global solar photovoltaic industry. Nature Energy, 5(6), 510-512.

[2] Creutzig, F., Agoston, P., Goldschmidt, J. C., Luderer, G., Nemet, G., Pietzcker, R. C., ... & Edenhofer, O. (2017). The underestimated potential of solar energy to mitigate climate change. Nature Energy, 2(9), 17140.

[3] Green, M. A., Emery, K., Hishikawa, Y., & Warta, W. (2019). Solar cell efficiency tables (Version 54). Progress in Photovoltaics: Research and Applications, 27(1), 3-12.

[4] Li, L., Wang, H., Zhang, H., & Han, G. (2017). A review of photovoltaic systems' development and policies in China and the US. Renewable and Sustainable Energy Reviews, 68, 597-607.

[5] Lu, R., Xie, X., & El Saddik, A. (2020). A survey of smart grids: Innovations, technologies, and applications. IEEE Access, 8, 144404-144420.

[6] Mazria, E. (2014). The passive solar energy book: A complete guide to passive solar home, greenhouse, and building design. Rodale

[7] Fei Ma, Yang Zhao, Zihan Qu, and Jingbi You (2023). Development of Highly Efficient Perovskite Solar Cells. Accounts of materials research paper 4(8). 716-725

[8] Arabnejad, H., & Siahkolah Amiri, B. (2017). A novel single-axis sun tracking system for PV panels in desert environments. Solar Energy, 144, 35-47.

[9] Lin, L., & E, J. (2016). Economic analysis of a single-axis solar tracking system for large-scale photovoltaic power plants. Renewable Energy, 95, 388-399.

[10] Colleoni, M., & Leonardi, R. (2019). Environmental assessment of single-axis solar tracking systems: A case study in Italy. Solar Energy, 186, 122-132.

[11] Chang, Y.P. (2010). Optimal the tilt angles photovoltaic modules in Taiwan. Electrical Power and Energy Systems, London, v. 32, p. 956-964.
[12] Sharma, Dinesh & Purohit, Ghanshyam. (2014). Analysis of the Effect of Fill Factor on the Efficiency of Solar PV System for Improved Design of MPPT.
[13] James W. Nilsson and Susan A. Riedel. Introduction to Electric Circuits. RRD Jefferson City, Wiley. 2012
[14] Allan R. Hambley (1996). Electrical Engineering: Principles & Applications. Pearson,

International Journal of Advanced Engineering Research and Science (IJAERS)
Peer-Reviewed Journal
ISSN: 2349-6495(P) | 2456-1908(O)
Vol-11, Issue-5; May, 2024
Journal Home Page Available: https://ijaers.com/
Article DOI: https://dx.doi.org/10.22161/ijaers.115.3

Prevalence of Tuberculosis in the Brazilian Population and Its Aggravating Factors – Systematic Review

Prevalência da Tuberculose na População Brasileira e Seus Fatores agravantes – Revisão Sistemática

Amanda Lima Franco[1], Amanda Patrícia Gaudio Bayma[2], Ana Carolina Abdon Seixas[3], Arthur Henzo da Silva Santos[4], Bárbara Ferreira Pereira[5], Daniele Lima da Costa[6], Maria Gabriela Perdigão Barros Monteiro[7], Isabela Lima Christo Alves De Campos[8], Lohanna Gama Nunes[9], Leonildo Pinheiro de Sousa Junior[10], Jéssica Pará Amaral de Oliveira[11], Luiza Bastos Campos[12], Maria Eduarda Menezes Almeida[13], Maria Mirella Nunes Bessa Guerra[14], Rayssa Lima Vilela[15], Amanda Fernandes Merhe[16], Antônio Rudyson Maravalhas de Barros[17], Bernar A Macedo Alves[18], Vitor Rocha Leitao[19], Renan Willian Costa da Silva[20], Brendo Silva Gaia Farias[21], Luíza Fernandes Malheiro[22], Leonardo Wanzeller Magalhães[23], Maria Rita Barboza Rocha[24], Ana Maria Ferreira Cruz Toledo[25]

[1-16]Acadêmico de Medicina do Centro Universitário da Amazônia, Belém, Pará – UNIFAMAZ.
[8] Médico graduado pela Universidade do Estado do Pará, Santarém - UEPA
[17]Médico graduado pela Universidade Federal do Pará, Belém – UFPA.
[18-22]Acadêmicos de Medicina da Universidade Federal do Pará, Belém – UFPA.
[23]Acadêmico de medicina do Instituto de Educação Médica, Castanhal, Pará – IDOMED.
[24]Acadêmico de medicina no centro universitário do Pará, Belém – CESUPA.
[25]Acadêmico de medicina da Pontifícia Universidade Católica de Goiás, Goiânia – PUC.
Email: Amanda.lima.franco@gmail.com

Received: 11 Mar 2024,

Receive in revised form: 25 Apr 2024,

Accepted: 07 May 2024,

Available online: 15 May 2024

***Keywords*— Tuberculosis; Illness; Brazil; Contamination; Combat.**

***Abstract*— *Tuberculosis disease is a public health problem in Brazil, with high population mortality rates. The main problem with this pathology is the high number of people at the mercy of society, such as homeless people and those with the HIV virus, who, when affected, have a greater chance of causing undesirable outcomes. This work aims to demonstrate to the scientific community the impact of this problem in Brazil, based on the quantification of numbers offered by the federal government DATA SUS. The methodology of this study is a systematic observational review, searching for data from 2001 to 2024 on Tuberculosis. As a result, in this period almost one hundred thousand people were diagnosed with TB, mainly men aged around 20 – 30 years. Therefore, the high power of contamination of this disease in the population is demonstrated, as well as the continued need for public policies, which still appear to be flawed, such as ditero combat.*

I. INTRODUÇÃO

A tuberculose (TB) permanece como problema de saúde pública no Brasil, pelos seus padrões altos de morbidade e mortalidade, principalmente atacando pessoas à mercê da sociedade, como portadores do vírus HIV e privados de liberdade. Contudo, possui boa taxa de sucesso ao tratamento, com níveis de ≥90% de sucesso, sendo que, conforme a ORGANIZAÇÃO Mundial da Saúde (OMS), até o ano de 2025, projeta-se redução de 75% da sua mortalidade. Neste país, em 2019, foram estimados cerca de 10 milhões de diagnósticos e 1,4 milhões com morte, estando na lista da OMS com as maiores taxas de TB e coinfecção de TB-HIV.

A tuberculose é uma doença infecciosa e transmissível, afetando principalmente os Pulmões e a função respiratória, embora possa acometer outros órgãos e sistemas. Tem como agente biológico o Mycobacterium tuberculosis ou bacilo de Koch, com a principal sintomatologia de febre vespertina, sudorese noturna, emagrecimento, fadiga e tosse. Neste contexto, seu diagnóstico aponta os seguintes exames: baciloscopia, teste rápido molecular para TB, cultura mico bactéria e raio-x de tórax. Transmitida pela inalação de aerossóis advindos das vias aéreas contendo o bacilo, desta forma após a inalação destes as bactérias intra e extracelulares crescem preferencialmente nas vias aéreas superiores dos pulmões, especialmente nos álveos macroscópicos, demorando de 3 a 4 semanas para desenvolver células T imunológicas e levando ao crescimento destas tanto em paciente imunocomprometidos ou não. Entretanto, muitos destes desenvolvem sintomas de forma latente e nem sempre acompanhados de sinais radiológicos.

O risco de morte por TB está associado a países com recursos restritos, fatores de desigualdade socioeconômica, idade avançada e associação a outras comorbidades. De acordo com estudos publicados por Nordholm AC et al. 2023, a TB acomete principalmente homens com mais idade e com múltiplas doenças. Por outro lado, o risco de fatalidade é mais prevalente nos primeiros 6 meses de tratamento devido a um declínio do tratamento.

A principal problemática desta doença é seu seguimento clínico. A adesão ao tratamento se torna afetada, pelo tempo e quantidade de medicações, onde o esquema RIPE (rifampicina, isoniazida, pirazinamida e etambutol) leva de 9 a 12 meses para eficiência absoluta, sendo que as taxas de sucesso quando se utiliza de forma correta os fármacos chegam a 81%. Assim, a falta de informação, ignorância popular, medo e efeitos colaterais levam o Brasil a números exorbitantes de diagnósticos e óbitos, eventos trágicos que assolam a população. O objetivo central deste estudo é abordar e quantificar, a partir de dados governamentais, números de diagnósticos e óbitos na população brasileira entre 2001 e 2023 e demonstrar à comunidade científica como os são preocupantes.

II. METODOLOGIA

Artigo em caráter de revisão sistemática da literatura, observacional, abordando trabalhos publicados nos últimos 5 anos na base de dados PUBMED e resultados do site DATA SUS tabelados a partir do TABNET. Foram utilizados os descritores em inglês “diagnosis” and “tuberculosis” and “treatment” and “Brasil”, analisando artigo de livre acesso. Já no TABNET, selecionaram-se os anos de 2001 a 2023, com ano de diagnóstico, casos confirmados e mortalidade. Foi realizada análise multivariada para estimar associação entre as variáveis com o abandono.

A partir disto, desenvolveu-se a pergunta PICOTT “Qual a porcentagem de notificação pelo governo do Brasil de pacientes diagnosticados com Tuberculose relacionados à mortalidade desta população? ”.

I. RESULTADOS

Tabela 1: Relação ano e casos confirmados de TB.

ANO DIAGNÓSTICO	CASOS CONFIRMADOS
2001	3600
2002	3882
2003	4038
2004	4146
2005	4040
2006	3831
2007	3821
2008	3842
2009	4140
2010	4161
2011	4370
2012	4093
2013	4167
2014	3985
2015	4031
2016	4254
2017	4542
2018	4711
2019	5530

2020	**4934**
2021	**5330**
2022	**5966**
TOTAL	**95.414**
ÓBITOS POR TUBERCULOSE	**54611**

FONTE:(http://tabnet.datasus.gov.br/cgi/tabcgi.exe?sinannet/cnv/tubercpa.def)

II. DISCUSSÃO

Ao total, foram utilizados 22 anos de pesquisa no DATA SUS, obtendo-se um resultado de 95.414 casos confirmados de TB no Brasil, havendo um crescente nos números nacionais e piores valores de informação.

Um dos fatores observados nas pesquisas foi a epidemiologia das populações de risco, com aumento exponencial da migração e refugiados no Brasil, advindos de países que não possuem campanhas de vacinações ou políticas públicas associadas. Tal fator deu-se início pela imersão do país como membro do BRICS, assim como organizador de eventos de escala mundial, como a Copa do Mundo de futebol. Assim, esta população específica aplicou vulnerabilidade à sociedade.

Os resultados apresentam crescimento nos anos seguintes aos casos diagnosticados de TB. O perfil destes teve 63,6% diagnosticados, sendo do sexo masculino, seguindo para 57,2%, evoluindo para óbitos. Em relação às faixas etárias acometidas, de um total de 95.414 casos ditos, 692 acometeram crianças de 1 a 4 anos, 682 de 5 a 9 anos, 1516 de 10 a 14 anos, 6945 de 15 a 19 anos, 44899 adultos de 20 a 39 anos, 26912 de 40 a 59 anos, 4313 de 60 a 64 anos, 3371 de 65 a 69 anos, 4092 de 70 a 79 anos e 1485 de idosos com 80 ou mais anos.

O combate à TB é um fator de saúde pública, podendo associar as políticas governamentais e seu esforço à detecção e tratamento. Um exemplo é o estado do Piauí, que descentralizou as ações da medicina da família e comunidade a ações primarias, reduzindo suas fontes de contatos e reduzindo a disseminação da mazela. Em adição à magnitude desta, do total de casos confirmados nestes 22 anos, 80885 formam os números de novos diagnósticos, com uma reincidiva de 4646 casos e reincidiva após o abandono de 5159 pacientes. Assim, foram necessárias a adição de impactos econômicos no país, custeando cerca de US$ 57 milhões de dólares.

Por fim, os resultados apontam que a magnitude dos números de óbitos relacionados à TB, 54%, está proporcionalmente interligada à população de risco. Entre pacientes em cárcere privado, moradores de rua e portadores de AIDES, a incidência foi maior que na população geral. A proporção de casos de reincidiva em aprisionados comparados a não aprisionados foi de 43% e 34%. Já em relação aos moradores de rua, fatores como falta de moradia, insegurança e comorbidades, uso de drogas e álcool, dificulta o reconhecimento de sintomas, tendo suas condições de vida agravam o acesso à saúde e continuidade ao tratamento, tornando estes um ciclo vicioso e resistência farmacológica.

III. CONCLUSÃO

A tuberculose mostrou-se uma doença altamente contaminante, sendo que, mesmo que considerando os estímulos monetários governamentais ao seu combate, ainda é um problema à comunidade. Políticas de promoção a direitos humanos à população carcerária, atenção à população em situação de rua, tais como tratamentos e políticas de prevenção à transmissão de ISTs, têm demonstrado melhorias, porém não suficientes para reduzir significativamente a TB. Conforme a complexidade do contexto desta, a relevância deste estudo é demonstrar à comunidade científica que ainda se pode tolerar melhorias nas políticas governamentais, implementando a pacientes específicos e individualizando grupos em detrimento do impacto da sua incidência.

REFERENCES

[1] WHO. (2015). *The end TB strategy*. Www.who.int. https://www.who.int/publications/i/item/WHO-HTM-TB-2015.19

[2] Sousa, G. J. B., Maranhão, T. A., Leitão, T. do M. J. S., Souza, J. T. de, Moreira, T. M. M., & Pereira, M. L. D. (2021). Prevalência e fatores associados ao abandono do tratamento da tuberculose. *Revista Da Escola de Enfermagem Da USP*, *55*. https://doi.org/10.1590/s1980-220x2020039203767

[3] Ridolfi, F., Peetluk, L. S., Amorim, G., Turner, M., Figueiredo, M. C., Cordeiro-Santos, M., Cavalcante, S., Afrânio Lineu Kritski, Betina Durovni, Andrade, B. B., Sterling, T. R., & Valeria Cavalcanti Rolla. (2022). Tuberculosis Treatment Outcomes in Brazil: Different Predictors for Each Type of Unsuccessful Outcome. *Clinical Infectious Diseases*, *76*(3), e930–e937. https://doi.org/10.1093/cid/ciac541

[4] Anne Christine Nordholm, Aase Bengaard Andersen, Wejse, C., Norman, A., Claus Thorn Ekstrøm, Peter Henrik Andersen, Troels Lillebæk, & Koch, A. (2023). Mortality, risk factors, and causes of death among people with tuberculosis in Denmark, 1990-2018. *International Journal of Infectious Diseases*, *130*, 76–82. https://doi.org/10.1016/j.ijid.2023.02.024

[5] Suárez, I., Fünger, S. M., Kröger, S., Rademacher, J., Fätkenheuer, G., & Rybniker, J. (2019). The Diagnosis and Treatment of Tuberculosis. *Deutsches Arzteblatt International*, *116*(43), 729–735. https://doi.org/10.3238/arztebl.2019.0729

[6] Silva, D. R., Mello, F. C. de Q., Johansen, F. D. C., Centis, R., D'Ambrosio, L., & Migliori, G. B. (2023). Migration and medical screening for tuberculosis. *Jornal Brasileiro de Pneumologia: Publicacao Oficial Da Sociedade Brasileira de Pneumologia E Tisilogia*, *49*(2), e20230051. https://doi.org/10.36416/1806-3756/e20230051

[7] Brito, A. B., Magalhães, W. B. de, Paiva, J. P. S. de, Leal, T. C., Silva, L. F. da, Santos, L. G., Santana, G. B. de A., Fernandes, T. R. M. de O., & Souza, C. D. F. de. (2020). Tuberculosis in Northeastern Brasil (2001-2016): trend, clinical profile, and prevalence of risk factors and associated comorbidities. *Revista Da Associação Médica Brasileira*, *66*, 1196–1202. https://doi.org/10.1590/1806-9282.66.9.1196

International Journal of Advanced Engineering Research and Science (IJAERS)
Peer-Reviewed Journal
ISSN: 2349-6495(P) | 2456-1908(O)
Vol-11, Issue-5; May, 2024
Journal Home Page Available: https://ijaers.com/
Article DOI: https://dx.doi.org/10.22161/ijaers.115.4

Climate analysis of the semi-arid region of Paraíba: Challenges and sustainable strategies

Análise climática do Semiárido paraibano: Desafios e estratégias sustentáveis

Amanda Cristiane Gonçalves Fernandes[1], Raimundo Aprígio de Menezes Júnior[2]

[1]Centro de Ciências Exatas e Natureza (CCEN)-UFPB, BRASIL
UFPB Campus I, Cidade Universitária, S/N – João Pessoa, Paraíba, Brasil CEP: 58.051-900
Email: amandafernandestt@gmail.com
[2] Departamento de Energias Alternativas e Renováveis (CEAR), UFPB, BRASIL
UFPB Campus I, Cidade Universitária, S/N – João Pessoa, Paraíba, Brasil CEP: 58.051-900
Email: jrmenezes@cear.ufpb.br

Received: 15 Mar 2024,

Receive in revised form: 27 Apr 2024,

Accepted: 05 May 2024,

Available online: 15 May 2024

***Keywords*— Adaptation strategies, Cistern Program, Climatic trends.**

***Abstract*— *This study aimed to analyze climatic trends in the semi-arid region of Paraiba by understanding changes in climatic variables over time and proposing adaptation and mitigation strategies to address the challenges posed by climate change, aiming to promote sustainable and resilient development in the region. The study area corresponds to the municipalities of Remígio, Esperança, Arara, Solânea, Lagoa Seca, São Sebastião de Lagoa de Roça, and Queimadas. Climatic variables such as Average Daily Temperature (C°), Precipitation (mm/day) and Evapotranspiration (mm/day) were obtained from the Goddard Earth Sciences Data and Information Services Center (GES DISC) through the tool also obtained in the study by Giovanni (2023). Descriptive statistics of climatic variables were performed, the Kendall test was used to assess the presence of temporal trends, and simple regression analysis was conducted to explore relationships between climatic variables. The climatic analyses indicated a decreasing trend in precipitation and evapotranspiration over time. This highlights the vulnerability of the semi-arid region of Paraiba to adverse climatic conditions, with potential impacts on available water resources. It is essential to implement policies and practical measures to address water scarcity, rising temperatures, and extreme events, thereby ensuring a more resilient and sustainable future for the semi-arid region of Paraiba.*

I. INTRODUÇÃO

A desertificação emerge como uma preocupação ambiental proeminente, especialmente nas áreas áridas e semiáridas, destacando-se como um problema grave dentre as questões contemporâneas sobre o meio ambiente. No Nordeste do Brasil, essa problemática se manifesta na região semiárida devido à interação complexa entre o clima local e a ampla gama de vulnerabilidades dos recursos naturais, aliadas aos impactos das atividades humanas. Esses fatores combinados delineiam um cenário de grande suscetibilidade à desertificação (Garcia et al., 2019).

Santana (2007) destaca os principais elementos ambientais associados à suscetibilidade à desertificação, incluindo as características do solo, os padrões de precipitação pluviométrica, a morfologia e a altitude do relevo, o bioma dominante, a cobertura vegetal e seu estado de conservação.

As variáveis climáticas, tais como a precipitação, a temperatura e a evapotranspiração, exercem um papel crucial na desertificação das áreas semiáridas. A escassez de chuva e o aumento da temperatura podem resultar na diminuição da vegetação e no agravamento da erosão do solo, o que culmina em degradação ambiental e desertificação. Além disso, as mudanças climáticas podem impactar negativamente a diversidade biológica e acelerar o processo de desertificação ao reduzir a evapotranspiração, levando consequentemente à diminuição das chuvas nessas áreas secas. Tais impactos podem comprometer a produção agrícola, os recursos hídricos, a necessidade de irrigação e a biodiversidade, alterando significativamente o ecossistema da Caatinga e acelerando o avanço do processo de desertificação (Tavares et al., 2019; Medeiros et al., 2019).

Apesar da significativa quantidade de estudos realizados no semiárido brasileiro, essas áreas são frequentemente afetadas por ações humanas e eventos naturais, resultando em um agravamento das secas severas na região. Portanto, é de extrema importância estudar e compreender a variabilidade climática e da vegetação para o planejamento adequado das atividades agrícolas, hídricas e socioeconômicas da região (Souza et al., 2022).

Assim, este estudo objetivou analisar as tendências climáticas na região do semiárido Paraibano, utilizando métodos científicos como análises climáticas e sensoriamento remoto. Pretendeu-se compreender as mudanças nas variáveis climáticas, como precipitação, evapotranspiração e temperatura, ao longo do tempo, e avaliar os impactos dessas mudanças no ambiente e na sociedade local. Além disso, buscou-se propor estratégias de adaptação e mitigação para enfrentar os desafios impostos pelas mudanças climáticas, visando promover um desenvolvimento sustentável e resiliente na região.

II. MÉTODOS

2.1. Caracterização da área de estudo

A área de estudo corresponde aos municípios de Remígio, Esperança, Arara, Solânea, Lagoa Seca, São Sebastião de Lagoa de Roça e Queimadas. Estes municípios estão inseridos na delimitação do semiárido paraibano (Fig. 1).

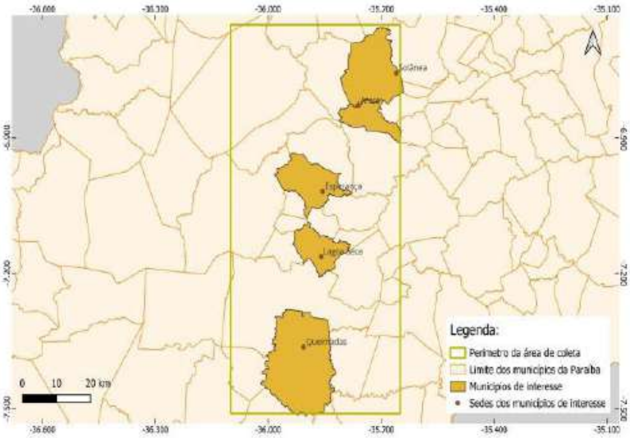

Fig. 1: Mapa de localização dos municípios paraibanos pertencentes a delimitação do semiárido.

2.2. Estudo da correlação das séries climáticas dos municípios estudados.

Para fins de coleta dos dados climáticos, foi definido um retângulo englobando todos os pontos de coletas que compreendem os municípios estudados, sendo as coordenadas -36.0652 W, -7.2985 S, -35.395 W, -6.3866 S (Figura 2). Foi definida uma série histórica de 1984 a 2014 a partir dos dados do Global Land Data Assimilation System – GLDAS com resolução de 0,25°.

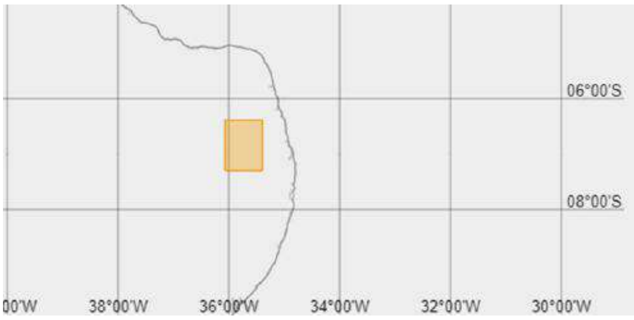

Fig. 2: Pontos de coleta no GLDAS referente a área de estudo.

Os dados do GLDAS resultaram de uma colaboração entre a NASA (*National Aeronautics and Space Administration*), o GSFC (*Goodard Space Flight Center*) e os NCEP (*National Centers for Environmental Prediction*) e NOAA (*National Aeronautics and Space Administration*). O objetivo principal do GLDAS foi criar um conjunto de dados de alta resolução em escala global, unindo observações provenientes de satélites e estações terrestres, por meio da aplicação de modelos de superfície terrestre (LSM) e técnicas de assimilação de dados (PARK & CHOI, 2014).

As variáveis climáticas como a Temperatura média diária (K°), Precipitação (Kg.m².s^{-1}) e Evapotranspiração (Kg.m².s^{-1}) foram obtidas na plataforma *Goddard Earth Sciences Data and Information Services Center* (GES DISC) através da ferramenta também obtida no estudo de Giovanni (2023). Os dados de Temperatura média diária foram convertidos de Kelvin (K°) para Celsius (C°) e Precipitação e Evapotranspiração de Kg.m².s^{-1} para mm/dia. De posse da série histórica e com auxílio do pacote Office Excel, foram plotados gráficos para cada variável que se encontram nas figuras 3, 4 e 5.

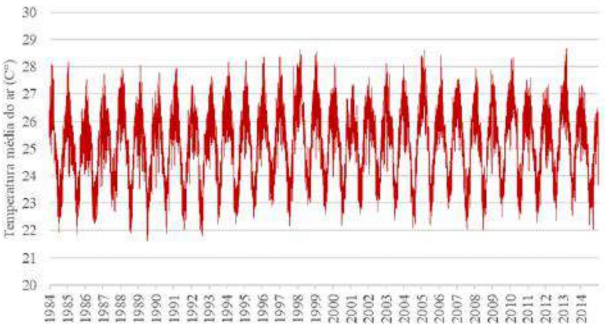

Fig. 3: Série histórica diária da Temperatura média do ar (C°) para a região de coleta de 1984 a 2014.

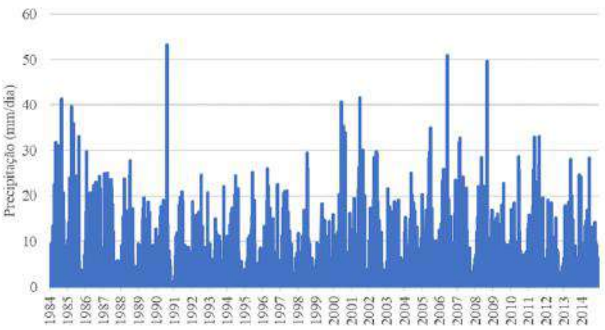

Fig. 4: Série histórica diária da Precipitação (mm/dia) para a região de coleta de 1984 a 2014.

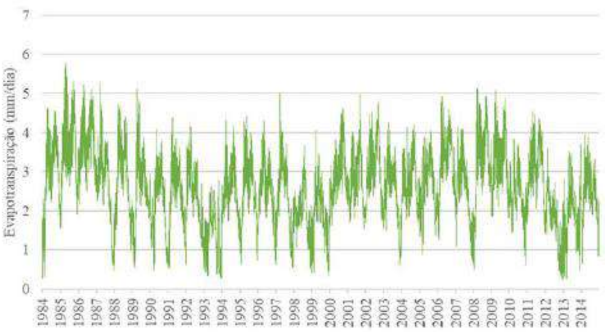

Fig. 5: Série histórica diária da Evapotranspiração (mm/dia) para a região de coleta de 1984 a 2014.

Todas as análises realizadas foram feitas através do software Rstudio, seguindo os pacotes de dados específicos para cada análise: Na tabela 1 são apresentadas as análises estatísticas e os pacotes utilizados no software Rstudio.

Tabela 1: Análises estatísticas e os pacotes utilizados no software Rstudio.

ANÁLISE	PACOTES UTILIZADOS
Estatística Descritiva	\`summarytools\`, \`psych\`
Teste de Kendall	\`Kendall\`, \`coin\`
Regressão Linear Múltipla	\`car\`, \`lmtest\`, \`ggplot2\`
Visualização de Dados Temporais	\`ggplot2\`, \`tsibble\`, \`plotly\`
Manipulação de Dados e Estatísticas	\`dplyr\`, \`tidyr\`, \`broom\`, \`ggplot2\`
Tratamento de Datas	\`lubridate\`

Fonte: Dados da pesquisa, (2023).

2.3. Descrição dos Dados

Para iniciar a análise, realizou-se uma estatística descritiva das variáveis climáticas estudadas, incluindo Precipitação, Evapotranspiração. Os dados foram resumidos através de medidas como mínimo, primeiro quartil, mediana, média, terceiro quartil e máximo com o auxílio do pacote "*psych*" (Revelle, 2023).

2.4. Teste de Kendall

Utilizou-se o Teste de Kendall para avaliar a presença de tendências temporais nas variáveis climáticas. Esse teste é robusto e adequado para identificar mudanças ao longo do tempo. Foi aplicado o teste não-paramétrico de Mann-Kendall por ser uma análise robusta e sequencial com o intuito de se analisar a presença de tendências temporais estatisticamente significativas. Para esse teste foi utilizado o pacote trend (Pohlert, 2023). Todas as análises foram realizadas com o auxílio do software RStudio.

O teste de Mann-Kendall é baseado na estatística de Mann-Kendall (S), que é calculada da seguinte maneira:

$$S=\sum_{i=1}^{n-1}\sum_{j=i+1}^{n} \text{sign}(x_j - x_i)$$

Onde:

n é o número de observações na série temporal.

x_i é o valor da observação na posição *i* na série temporal.

x_j é o valor da observação na posição

sign (x_j-x_i) é a função de sinal, que retorna +1 se x_j-x_j > 0, -1 se x_j-x_i < 0 e 0 se x_j-x_i = 0.

Uma vez calculada a estatística de Mann-Kendall (S), pode-se então determinar a significância estatística da tendência utilizando a distribuição normal padrão. Isso é feito calculando o valor z:

$$Z = \frac{S-1}{\sqrt{V}}$$

V: é a variância da estatística de Mann-Kendall, dada por:

$$V = \frac{n\,(n-1)(2n+5) - \sum_{p=1}^{k} tp\,(tp-1)(2tp+5)}{18}$$

t_p é o número de empates de tamanho p na série temporal.

k é o número de valores distintos na série temporal.

Finalmente, o valor z é utilizado para calcular o valor p, que indica a significância estatística da tendência observada. Este valor p é então comparado com um nível de significância escolhido para determinar se a tendência é estatisticamente significativa.

2.5. Análise de Regressão

Realizou-se uma análise de regressão simples para explorar as relações entre as variáveis climáticas. Modelos foram ajustados para investigar a associação entre Precipitação, Evapotranspiração e Temperatura.

O modelo de regressão, que expressa a relação entre as variáveis em termos matemáticos. O modelo mais comum é a regressão linear, que assume que a relação entre as variáveis é linear. O modelo de regressão linear simples é representado pela equação:

$$Y=\beta_0+\beta_{1X}+\varepsilon$$

Onde:

Y é a variável dependente (ou resposta).

X é a variável independente (ou explanatória).

β 0 é o intercepto da linha de regressão.

β1 é o coeficiente de regressão (ou inclinação), que representa a mudança esperada em Y para uma unidade de mudança em X.

ε é o termo de erro, que representa a variação não explicada pelo modelo.

2.6. Enhanced Vegetation Index – EVI

As séries temporais de imagens provenientes do satélite TERRA foram adquiridas do Banco de Produtos EVI/MODIS na base Estadual Brasileira (Embrapa Informática Agropecuária, 2024). Este banco armazena e disponibiliza na Internet imagens do produto MOD13Q1, organizadas por estados, na projeção geográfica, datum WGS-84 e no formato GeoTIFF. O produto MOD13Q1 é composto por pixels de alta qualidade radiométrica, geometria de observação otimizada, presença mínima de nuvens e aerossóis, sendo selecionados a partir de imagens diárias ao longo de 16 dias. A coleção atual é a versão 6, que incorpora mudanças significativas para aprimorar a qualidade dos dados.

Para a composição das imagens, foram escolhidos três anos específicos: o primeiro ano de observação, um ano intermediário e o ano de conclusão das observações da área de estudo, que são os anos de 2004, 2012 e 2020, respectivamente. A fim de proporcionar uma representação mais precisa da cobertura vegetal, foi selecionada uma sequência de três imagens durante o período de estiagem da região, concentrado em janeiro, e outra sequência de três imagens durante o período das chuvas, em junho de cada ano.

III. RESULTADOS

Na realização deste estudo, empregou-se uma série temporal idêntica para a computação anual das quantidades de precipitação e evapotranspiração, bem como para o cálculo das médias anuais da temperatura do ar. Na tabela 2 procedeu-se à agregação dos dados acumulados mensalmente, resultando na definição das séries temporais mensais correspondentes.

3.1. Análise Descritiva

Tabela 2: Estatística descritiva das variáveis precipitação (Pr), evapotranspiração (Ev) e temperatura (Te).

	Pr	**Ev**	**Te**
Min:	0.0000	0.240	21.62
1st Qu:	0.0000	1.980	24.13
Median:	0.5827	2.640	25.36
Mean:	2.8291	2.605	25.17
3rd Qu:	3.8422	3.240	26.13
Max:	53.1403	5.790	28.68

Precipitação: Min-Max: A precipitação varia de 0 mm a 53.14 mm, indicando uma considerável variabilidade nas chuvas; mediana (Median): A mediana de 0.58 mm sugere uma distribuição desigual de chuvas, com uma parte significativa dos dados concentrada em valores mais baixos; média (Mean): A média de 2.83 mm aponta para uma tendência de chuvas moderadas, mas a variabilidade pode resultar em períodos prolongados de escassez; 3º Quartil: 75% dos dados de precipitação estão abaixo de 3.84 mm, indicando uma prevalência de eventos de chuva de intensidade moderada.

Evapotranspiração: Min-Max. A evapotranspiração varia de 0.24 a 5.79, destacando a capacidade da região de perder água para a atmosfera, principalmente em condições de temperaturas mais altas; mediana (Median): A mediana de 2.64 sugere que a metade dos dados está concentrada em valores moderados de evapotranspiração; média (Mean): A média de 2.61 indica uma taxa consistente de evapotranspiração na região; 3º Quartil: 75% dos dados de evapotranspiração estão abaixo de 3.24, sugerindo que a maior parte da região experimenta níveis moderados de perda de água para a atmosfera.

Temperatura: Min-Max. As temperaturas variam de 21.62°C a 28.68°C, indicando um clima predominantemente quente; mediana (Median) A mediana de 25.36°C representa a temperatura central, sugerindo que a maioria dos anos possui temperaturas moderadas a elevadas; média (Mean): A média de 25.17°C confirma a natureza quente da região; 3º Quartil: 75% dos dados de temperatura estão abaixo de 26.13°C, mostrando que a maioria dos anos está dentro de uma faixa moderada a quente.

A baixa mediana de precipitação sugere desafios relacionados à disponibilidade de água, fortalecendo a necessidade de políticas como o Programa de Cisterna. A variabilidade nas temperaturas destaca a necessidade de estratégias de adaptação para lidar com condições climáticas extremas.

As análises de tendência de Kendall que serão descritas posteriormente reforçam os padrões observados nos dados descritivos, fornecendo uma base estatística para as conclusões acima. Com base nos resultados, há uma necessidade evidente de políticas de gestão da água na região, como o Programa de Cisterna, para enfrentar os desafios de escassez de água devido à baixa precipitação e alta evaporação.

Na figura 6 é apresentado o blox-pot em relação a variabilidade das variáveis estudadas.

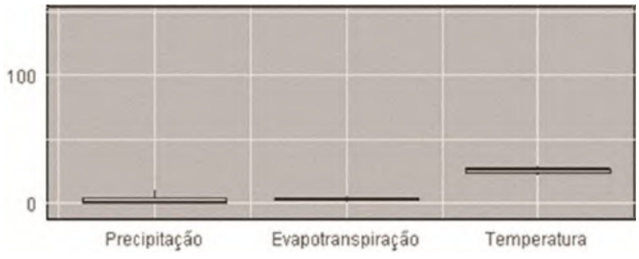

Fig. 6: Box-plot das variabilidades em relação as variáveis estudadas.

O boxplot destaca visualmente que a temperatura varia mais com o passar dos anos, no caso o boxplot é uma parte gráfica dos dados descritivos. Quanto mais alta a caixa, maior a variabilidade dos dados.

3.2. Interpretação dos Testes de Kendall para Tendências Climáticas

Na tabela 3 é apresentada os resultados do Teste de análise de séries temporais.

Tabela 3: Resultados da aplicação do Teste Kendall nas séries temporais estudadas.

Variáveis	Statistic	P-value	Method
Precipitação	-4,92936702	8,24965E-07	Mann kendall
Evapotranspiração	-9,43647383	3,85536E-21	Mann kendall
Temperatura	8,33272743	7,90009E-17	Mann kendall

Fonte: Autora, 2023.

Precipitação: A estatística de Kendall negativa sugere uma tendência significativa de diminuição na precipitação ao longo do tempo. O valor de p (8.25E-07) indica uma forte evidência estatística para esta redução. Esse resultado corrobora a importância de políticas como o Programa de Cisterna para mitigar os impactos da escassez de água.

Evapotranspiração: A estatística de Kendall fortemente negativa indica uma tendência significativa de diminuição na evapotranspiração ao longo do tempo. O valor de p (3.86E-21) também sugere uma forte evidência estatística dessa tendência. Isso pode indicar uma redução na perda de água para a atmosfera, o que pode impactar os recursos hídricos na região.

Temperatura: A estatística de Kendall positiva sugere uma tendência significativa de aumento nas temperaturas ao longo do tempo. O valor de p (7.90E-17) indica uma forte evidência estatística dessa tendência. Esse resultado destaca a importância de estratégias de adaptação às condições climáticas cada vez mais quentes.

O valor de p de cada teste estatístico se baseia em um valor fixo de 0,05. Se o valor de p de determinado teste estiver menor que 0,05, quer dizer que os seus dados deram diferença significativa ou que teve uma tendência significativa. Se tiver maior que 0,05 é ao contrário, não houve nenhuma diferença estatística significativa.

Os resultados dos testes de Kendall fortalecem as conclusões derivadas da análise descritiva, fornecendo uma base estatística para as tendências climáticas observadas. A significativa diminuição na precipitação e evapotranspiração sugere mudanças nas condições hidrológicas que podem impactar a disponibilidade de água. A tendência de aumento na temperatura destaca os desafios relacionados ao calor crescente na região, reforçando a necessidade de estratégias de adaptação e tecnologias sustentáveis.

3.3. Análise de eventos climáticos extremos

Para a análise de eventos climáticos extremos foi adotada a Análise de Distribuição Extrema (GEV) para Dados Climáticos do Semiárido. Realizamos uma análise de distribuição extrema (GEV) sobre as variáveis climáticas (Precipitação, Evapotranspiração e Temperatura) referentes ao semiárido paraibano. O objetivo dessa análise é compreender o comportamento dessas variáveis ao longo do tempo, fornecendo insights relevantes para a implementação de tecnologias sustentáveis na região em estudo.

Precipitação: A análise revelou que a distribuição GEV para a precipitação apresenta os seguintes parâmetros estimados: localização: 3.43e-12; escala: 1.17e-11 e forma: 3.39. Esses resultados indicam uma tendência para eventos extremos na precipitação, sugerindo uma variabilidade significativa ao longo do tempo. Na figura 7 é apresentado o gráfico que analisa o comportamento dos dados ao longo do tempo da variável Precipitação.

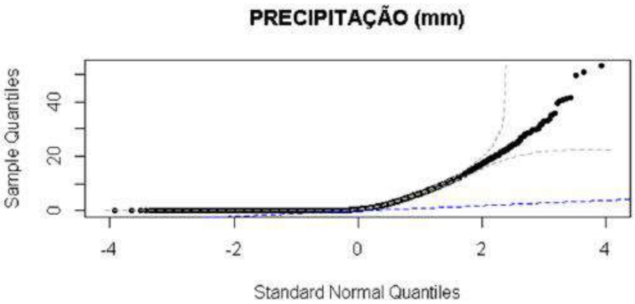

Fig. 7: Comportamento dos dados da variável precipitação ao longo do tempo.

Evapotranspiração: Os parâmetros estimados para a evapotranspiração são: localização: 2.27; escala: 0.92 e forma: -0.26. Esses resultados indicam uma distribuição GEV com características que podem afetar a gestão hídrica na região, fornecendo informações relevantes para a implementação de práticas sustentáveis. Na figura 8 é apresentado o gráfico que analisa o comportamento dos dados ao longo do tempo da variável Evapotranspiração.

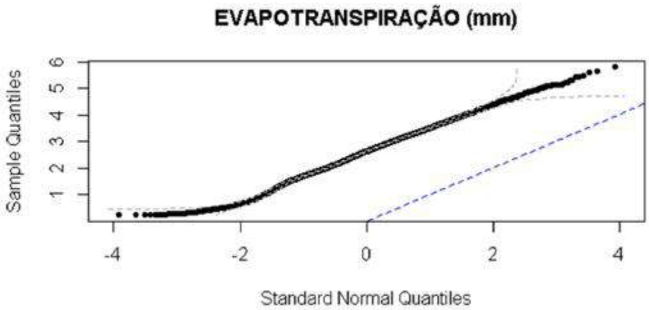

Fig. 8: Comportamento dos dados da variável evapotranspiração ao longo do tempo.

Temperatura: A análise da temperatura revela os seguintes parâmetros estimados: localização: 21.72; escala: 15.11; forma: 155.22. Esses resultados indicam uma forma acentuada na distribuição, destacando a variabilidade nas temperaturas ao longo do tempo. A linha de tendência da temperatura também está mais próxima da central, indicando que pode ser um modelo apropriado. Na figura 9 é apresentado o gráfico que analisa o comportamento dos dados ao longo do tempo da variável Temperatura.

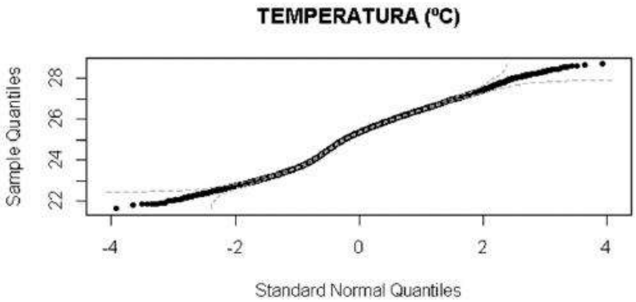

Fig. 9: Comportamento dos dados da variável temperatura ao longo do tempo.

Os resultados da análise GEV oferecem insights valiosos sobre a variabilidade climática no semiárido paraibano. A presença de eventos extremos e padrões de distribuição distintos em cada variável climática enfatiza a complexidade do ambiente. Essas informações são cruciais para a implementação de tecnologias sustentáveis que dependem das condições climáticas locais.

A interpretação desses resultados sugere que a região apresenta desafios consideráveis em termos de variabilidade climática, destacando a importância de abordagens adaptativas e tecnologias robustas para lidar com as condições extremas.

Em relação as hipóteses deste estudo, tem-se:

Análise Variabilidade Climática na região do semiárido: A análise da evapotranspiração e precipitação revela padrões notáveis na região. A evapotranspiração, embora apresente uma variação significativa, demonstra uma tendência persistente, sugerindo uma alta taxa de evaporação. Juntamente com a precipitação relativamente baixa, esses resultados indicam desafios consideráveis em relação ao fornecimento de água na região. Essa constatação fortalece a necessidade de políticas como o Programa de Cisterna, que podem oferecer uma solução para a escassez hídrica, capturando e armazenando água da chuva para uso posterior.

3.4. Regressão Linear Simples entre as variáveis

Tabela 4: Resultados de correlação da Regressão Linear Simples entre as variáveis estudadas.

Correlação de variáveis	Coeficiente	P-Valor
Precipitação/Evapotranspiração	Evapotranspiração 0.83339	2.2e-16
Precipitação/Temperatura	Temperatura -0.85867	2.2e-16
Evapotranspiração/Precipitação	Precipitação 0.030687	2.2e-16
Evapotranspiração/Temperatura	Temperatura -0.257050	2.2e-16
Temperatura/ Evapotranspiração	Evapotranspiração -0.50590	2.2e-16

Fonte: Autora, 2023.

Abaixo segue as discussões das correlações entre as variáveis estudadas.

-PRECIPITAÇÃO ~ EVAPOTRANSPIRAÇÃO: A variável independente EVAPOTRANSPIRAÇÃO tem um efeito significativo sobre a variável dependente PRECIPITAÇÃO (p-valor muito pequeno). O coeficiente de EVAPOTRANSPIRAÇÃO é positivo (0.83339), indicando que um aumento em EVAPOTRANSPIRAÇÃO está associado a um aumento em PRECIPITAÇÃO.

-PRECIPITAÇÃO ~ TEMPERATURA: A variável independente TEMPERATURA tem um efeito significativo sobre a variável dependente PRECIPITAÇÃO (p-valor muito pequeno). O coeficiente de TEMPERATURA é negativo (-0.85867), indicando que um aumento em TEMPERATURA está associado a uma diminuição em PRECIPITAÇÃO.

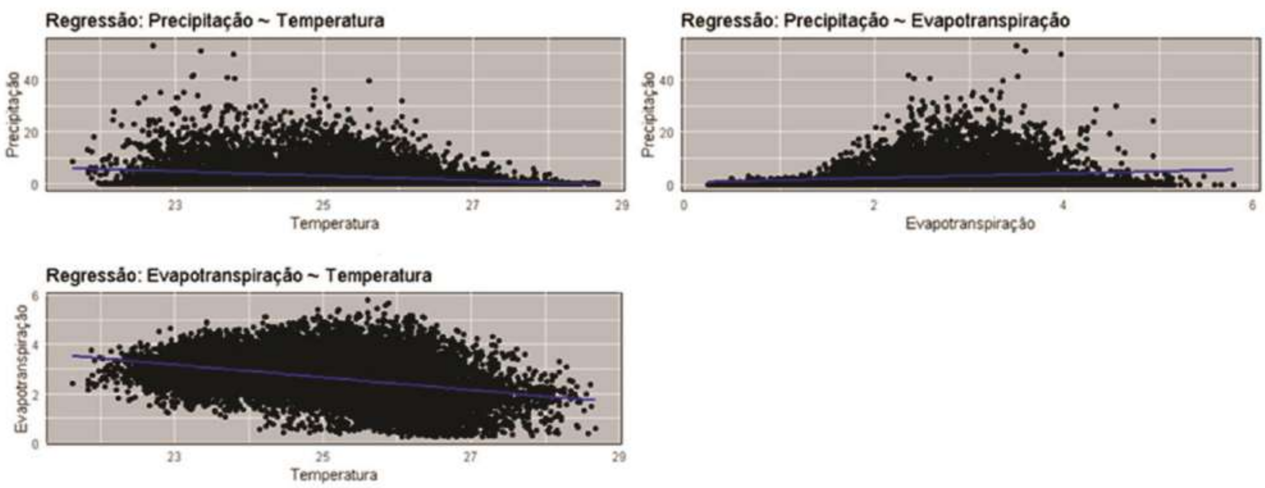

Fig. 10: Analise da reta de ajuste das variáveis estudadas

-EVAPOTRANSPIRAÇÃO ~ PRECIPITAÇÃO: A variável independente PRECIPITAÇÃO tem um efeito significativo sobre a variável dependente EVAPOTRANSPIRAÇÃO (p-valor muito pequeno). O coeficiente de PRECIPITAÇÃO é positivo (0.030687), indicando que um aumento em PRECIPITAÇÃO está associado a um aumento em EVAPOTRANSPIRAÇÃO.

-EVAPOTRANSPIRAÇÃO ~ TEMPERATURA: A variável independente TEMPERATURA tem um efeito significativo sobre a variável dependente EVAPOTRANSPIRAÇÃO (p-valor muito pequeno). O coeficiente de TEMPERATURA é negativo (-0.257050), indicando que um aumento em TEMPERATURA está associado a uma diminuição em EVAPOTRANSPIRAÇÃO.

-TEMPERATURA ~ PRECIPITAÇÃO: A variável independente PRECIPITAÇÃO tem um efeito significativo sobre a variável dependente TEMPERATURA (p-valor muito pequeno). O coeficiente de PRECIPITACAO é negativo (-0.062225), indicando que um aumento em PRECIPITAÇÃO está associado a uma diminuição em TEMPERATURA.

-TEMPERATURA ~ EVAPOTRANSPIRAÇÃO: A variável independente EVAPOTRANSPIRAÇÃO tem um efeito significativo sobre a variável dependente TEMPERATURA (p-valor muito pequeno). O coeficiente de EVAPOTRANSPIRAÇÃO é negativo (-0.50590), indicando que um aumento em EVAPOTRANSPIRAÇÃO está associado a uma diminuição em TEMPERATURA.

Com base nas análises de regressão realizadas entre as variáveis climáticas na região do semiárido Paraibano, podemos inferir informações relevantes para a teoria propostas:

Programa de Cisterna: A análise de regressão entre Precipitação e Evapotranspiração revelou uma relação significativa entre essas variáveis. O coeficiente positivo para Evapotranspiração indica que à medida que a evapotranspiração aumenta, a precipitação também tende a aumentar. Isso sugere que a região experimenta altas taxas de evaporação, o que pode ser uma indicação da necessidade de estratégias de conservação de água. Além disso, a regressão entre Precipitação e Temperatura mostrou uma relação negativa significativa. O aumento da temperatura está associado a uma diminuição na precipitação. Isso ressalta os desafios enfrentados pela região devido às altas temperaturas e baixa precipitação, reforçando a importância de iniciativas também de conservação de água.

Portanto, com base nas análises de regressão, há suporte estatístico para a teoria propostas. A implementação de um Programa de Cisterna pode ser justificada pela relação entre evapotranspiração e precipitação.

3.5. Análise do índice de vegetação melhorado – EVI

Os índices de vegetação (IVs) possuem um amplo potencial para avaliar de maneira rápida e abrangente a quantidade e as condições das plantas em áreas extensas no campo. Esses índices estabelecem uma relação entre a radiação solar e os tecidos fotossinteticamente ativos das plantas, visando destacar informações cruciais sobre a fitomassa verde presente na radiância refletida pelos dosséis vegetais. Essa abordagem é alcançada por meio da combinação de bandas espectrais na faixa do visível e infravermelho próximo. Dentre os principais IVs empregados no sensoriamento remoto, merece destaque o Enhanced Vegetation Index (EVI), que se destina a detectar a sensibilidade às variações na estrutura e arquitetura do dossel, incluindo índices de área foliar e fisionomia da planta. Adicionalmente, o EVI desempenha um papel crucial na minimização dos efeitos da influência do solo e da atmosfera na vegetação, conforme indicado por Caron e Minuzzi (2022).

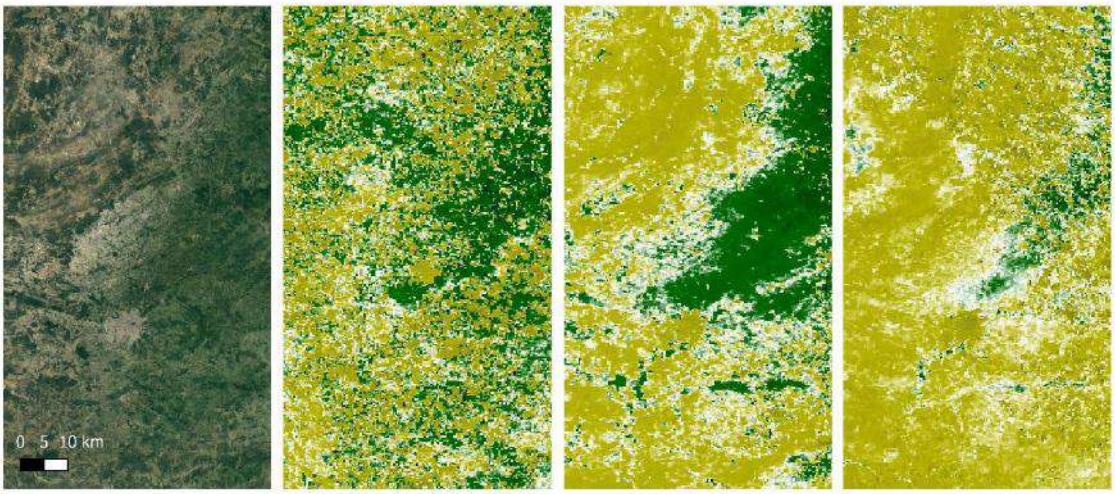

Fig. 11: Imagens EVI/MODIS do período de estiagem (janeiro) da área de interesse dos anos de 2004, 2012 e 2020, respectivamente.

Os dados processados para estudos ambientais têm sido gerados pelo sensor MODIS (*Moderate Resolution Imaging Spectroradiometer*), que está a bordo das plataformas orbitais do programa internacional EOS (*Earth Observing System*), sob a liderança da NASA (*National Aeronautics and Space Administration*). Lançado em dezembro de 1999, o satélite TERRA realiza passagens sobre o Equador às 10h30 (horário local), em órbita descendente. Os dados provenientes do MODIS, caracterizados por moderada resolução espacial, alta repetitividade, boa qualidade radiométrica, alta precisão geométrica, juntamente com correção atmosférica e distribuição gratuita, possuem um significativo potencial de aplicação no monitoramento da vegetação (Antunes e Esquerdo, 2014).

As figuras 11 e 12 apresentam o EVI para a área de estudos nos anos 2004, 2012 e 2020 as épocas de estiagem e chuvosa, respectivamente.

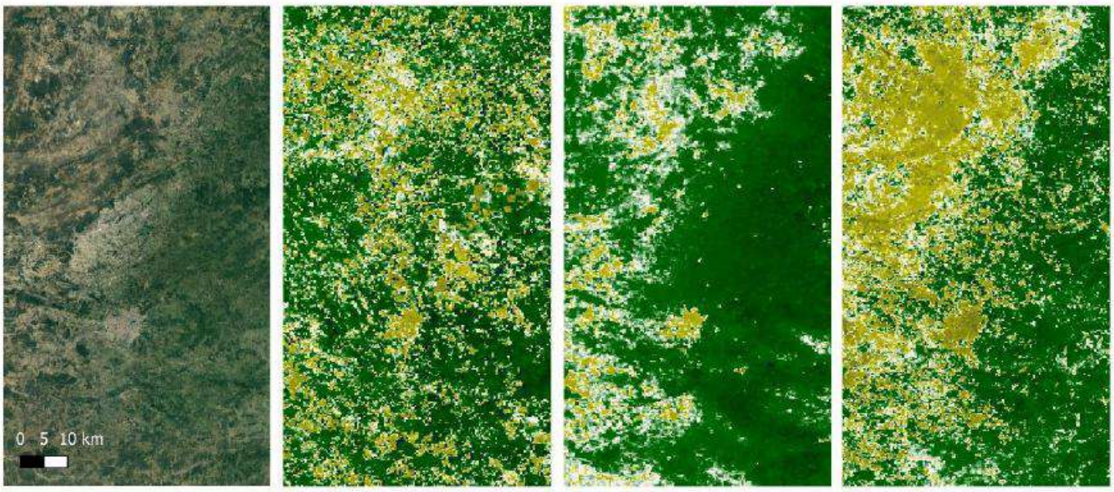

Fig. 12: Imagens EVI/MODIS do período das chuvas (junho) da área de interesse dos anos de 2004, 2012 e 2020, respectivamente.

IV. DISCUSSÃO

As análises climáticas indicam uma tendência de diminuição na precipitação e evapotranspiração ao longo do tempo. Isso destaca a vulnerabilidade da região do semiárido paraibano a condições climáticas adversas, com possíveis impactos nos recursos hídricos disponíveis. No semiárido, o clima se caracteriza pela variabilidade pluviométrica e a alta evapotranspiração, ocasionando o déficit hídrico. (EMBRAPA, 2024). Pelos os seus eventos extremos, a região do semiárido sobre com a escassez hídrica pelo período das secas e as chuvas torrenciais no período chuvoso. (Marengo, 2008).

O Quarto Relatório de Avaliação do International Panel on Climate Change (2007), aponta para a região do semiárido brasileiro como uma das regiões mais vulnerável pelas mudanças climáticas, tornando-as mais árida, aumento a ocorrência de eventos extremos de secas, e redução da demanda dos recursos hídricos. Essas alterações refletem negativamente sobre a vegetação, biodiversidade e sobre as atividades que precisam dos recursos naturais como matéria prima (Marengo, 2008).

Em 2022 o relatório do IPCC (Painel Intergovernamental sobre Mudanças Climáticas) apontou que os pesquisadores que atuam na região do semiárido vêm constatando o aquecimento global a partir do tratamento e modelagem de séries de dados coletados desde a década de 1980. Para esta região os extremos serão mais impactantes: períodos de chuvas intensos e secas mais prolongadas com intensidades maiores: será uma realidade maior para os próximos anos do que a realidade que ocorre hoje.

O estudo de Campos et al. (2010) previa o aumento da temperatura média variando entre 3º C a 6º C no estado da Paraíba e apontava para os riscos decorrentes para a cultura do feijão-caupi. Souza et al. (2016) em seu estudo detectou variação da temperatura no período de 2006 a 2010 e mudanças no uso e cobertura do solo para a cidade de João Pessoa-PB.

Sobre a importância do Programa de Cisternas na região os resultados dos testes de tendência indicam que a região enfrenta desafios significativos relacionados à escassez de água. A implementação e expansão de políticas como o Programa de Cisterna são fundamentais para lidar com a redução na precipitação e evapotranspiração, contribuindo para a segurança hídrica da população.

Alguns estudos (Bastos et al., 2011; Benko-Iseppon et al., 2011; Brito et al., 2012; Burney et al., 2014; Cesano et al., 2011; Freitas, 2011; Queiroz, 2011; Oliveira et al., 2015, Ventura et al., 2011) sugerem que para regiões com alta suscetibilidade sejam desenvolvidas ações de adaptação para o semiárido brasileiro como as tecnologias de captação e armazenamento de água de chuva, técnicas para o uso racional da água para irrigação, sistemas de cultivos múltiplos, reflorestamento local, entre outros. O estudo de Santana e Rahal (2020) aponta o Programa de Cisternas como alternativa de desenvolvimento local em municípios do semiárido.

Em relação a adaptação às mudanças climáticas a tendência de aumento nas temperaturas destaca a necessidade urgente de estratégias de adaptação. A região do semiárido Paraibano deve buscar medidas para enfrentar os desafios impostos pelo aquecimento global, como a implementação de práticas sustentáveis e o desenvolvimento de tecnologias de conservação de água.

Com base no Enhanced Vegetation Index (EVI), é possível observar uma redução na densidade fotossinteticamente ativa durante os períodos de seca ao longo dos anos, resultando em uma fitomassa fotossintética menos densa. Isso é evidenciado pela Figura 13, que mostra uma redução nas áreas verdes e uma sobreposição crescente das áreas amareladas. Embora as áreas verdes predominem durante o período chuvoso, como ilustrado na Figura 14, observa-se um padrão semelhante ao longo dos anos, com uma diminuição na densidade das áreas verdes e um aumento correspondente nas áreas amareladas, indicando uma redução na cobertura vegetal da caatinga. Esses resultados reforçam as observações realizadas com os dados climáticos e a necessidade de se implementar políticas públicas que visem contornar os eventos extremos que são cada vez mais presentes na região semiárida.

V. CONCLUSÃO

Em suma, os resultados apresentados neste estudo destacam a gravidade das mudanças climáticas no semiárido Paraibano e a urgência de ações para enfrentar esses desafios. A análise detalhada dos resultados obtidos fornece insights valiosos para compreender as tendências climáticas na região e para desenvolver estratégias de adaptação e mitigação. É essencial que sejam implementadas políticas e medidas práticas para lidar com a escassez de água, o aumento das temperaturas e os eventos extremos, garantindo assim um futuro mais resiliente e sustentável para a região do semiárido Paraibano. A colaboração entre diversos atores, incluindo comunidades locais, governos e instituições de pesquisa, é crucial para alcançar esse objetivo e garantir a segurança hídrica e ambiental da região a longo prazo.

AGRADECIMENTOS

Ao Programa de Pós Graduação em Desenvolvimento e Meio Ambiente da Universidade Federal da Paraíba.

REFERENCIAS

[1] Antunes, J. F. G. & Esquerdo, J. C. D. Classificação sub-pixel de séries temporais de dados MODIS para a quantificação de áreas inundadas do Pantanal. 2014. In: Anais 5º Simpósio de Geotecnologias no Pantanal, Campo Grande, MS. Embrapa Informática Agropecuária/INPE, 325 -335.

[2] Bastos, E.A., Nascimento, S.P., Silva, E.M., Freire Filho, R.F., Gomide, R.L., 2011. Identification of cowpea genotypes for drought tolerance. Revista Ciência Agronômica 42, 100-107.

[3] Benko-Iseppon, A.M., Soares-Cavalcanti, N. M., Belarmino, L.C., Bezerra Neto, J.P., Amorim, L. L.B., Ferreira Neto, J.R.C., Pandolfi, V., Azevedo, H.M.A., Silva, R.L.O., Santos, M.G., Alves, M. V., Kido, E.A. 2011. Prospecção de Genes de Resistência à Seca e à Salinidade em Plantas Nativas e Cultivadas. Revista Brasileira de Geografia Física 6, 1112-1134.

[4] Brito, L. T. de L., Cavalcanti, N. de B., Silva, A. de S., Pereira, L.A., 2012. Produtividade de água de chuva em culturas de subsistência no semiárido pernambucano. Engenharia Agrícola 32, 102-109.

[5] Burney, J., Cesano, D., Russell, J., LA Rovere, E.L., Corral, T., Coelho, N. S., Santos, L., 2014. Climate change adaptation strategies for smallholder farmers in the Brazilian Sertão. Climatic Change 126, 45-59.

[6] Campos, J. H. B. da C., Silva, M. T., & Silva, V. de P. R. da. (2010). Impacto do aquecimento global no cultivo do feijão-caupi, no Estado da Paraíba. Revista Brasileira De Engenharia Agrícola E Ambiental, 14(4), 396–404. https://doi.org/10.1590/S1415-43662010000400008.

[7] Caron, M. L. & Minuzzi, R. B. Estimativa de produtividade de soja com uso de perfis temporais de índices de vegetação do sensor MODIS em Sapezal, Mato Grosso. 2022. Revista Brasileira de Geografia Física, 15 (03), 1660-1675.

[8] Cesano, D., Rovere, E.L.L., Martin, O., Corral, T., Santos, L., Coelho, N.S., Neves, C.G., 2011. As experiências da coalizão adaptam Sertão na disseminação de tecnologias e estratégias de adaptação à mudança climática para o agricultor familiar do Semiárido Brasileiro. Revista Brasileira de Geografia Física 6, 1336-1350.

[9] Embrapa Informática Agropecuária. Banco de Produtos MODIS na base Estadual Brasileira. 2024. Disponível em <https://www.modis.cnptia.embrapa.br>. Acesso em 31 jan. 2024.

[10] Freitas, A.D.S., Silva, T.O., Menezes, R.S.C., Sampaio, E.V.S.B., Araújo, E.R., Fraga, V.S., 2011. Nodulação e fixação de nitrogênio por forrageiras da caatinga cultivadas em solos do semiárido paraibano. Revista Brasileira de Zootecnia 40, 1856-1861.

[11] Garcia, A. C. S.; Araújo Filho, J. C.; Silva, H. P. S. P.; Carvalho, R. M. C. M. O. Estudo espaço temporal de áreas susceptíveis à desertificação do semiárido brasileiro. (2019). Revista Gestão & Sustentabilidade Ambiental, 8 (3), 352-370. https://doi.org/10.19177/rgsa.v8e32019352-370.

[12] Giovanni. Giovanni: The Bridge Between Data and Science. 2023. v 4.38. Disponível em <https://giovanni.gsfc.nasa.gov/giovanni/> acesso em: 07 agosto 2023.

[13] IPCC. Intergovernmental Panel on Climate Change, 2007. The Physical Science Basis. Summary for Policymakers. Contribution of Working Group I to the Fourth Assessment

Report of the Intergovernmental Panel on Climate Change. IPCC, Genebra.

[14] Marengo, J. A. Mudanças climáticas globais e seus efeitos sobre a biodiversidade: caracterização do clima atual e definição das alterações climáticas para o território brasileiro ao longo do século XXI. 2008 Brasília: MMA.

[15] Medeiros, T. K. F.; Lustosa, E. A.; Oliveira, J. L. S. Silva, E. 2019. Desertificação ambiental: Causas e efeitos no semiárido paraibano. Anais I Congresso Internacional de Meio Ambiente e Sociedade e III Congresso Internacional da Diversidade do Semiárido. Campina Grande: Realize Editora.

[16] Oliveira, E.J., Aidar, S.T., Morgante, C.V., Chaves, A.R.M., Cruz, J.L., Coelho Filho, M.A., 2015. Genetic parameters for drought tolerance in cassava. Pesquisa Agropecuária Brasileira 50, 233-241.

[17] Park, J., & Choi, M. Estimation of evapotranspiration from ground-based meteorological data and global land data assimilation system (GLDAS). 2014. Stochastic. Environmental Research and Risk Assessment, 29 (8), 1963–1992. doi:10.1007/s00477-014-1004-2

[18] Pohlert, T. Trend: Non-Parametric Trend Tests and Change-Point Detection. 2023. R package version 1.1.5. Disponível em: https://CRAN.R-project.org/package=trend.

[19] Queiroz, M.A. Recursos Genéticos Vegetais da Caatinga para o Desenvolvimento do Semiárido Brasileiro. 2011. Revista Brasileira de Geografia Física 6, 1135-1150.

[20] Revelle, W. Psych: Procedures for Psychological, Psychometric, and Personality Research. 2023. Northwestern University, Evanston, Illinois. R package version 2.3.6, Disponível em: <https://CRAN.R-project.org/package=psych>.

[21] Santana, M.O (Org.). (2007). Atlas das áreas suscetíveis à desertificação do Brasil. Brasília: MMA.

[22] Santana, V. L.; Rahal, L. S. dos. Tecnologias sociais como impulso para o acesso à água e o desenvolvimento sustentável no meio rural brasileiro: a experiência do Programa Cisternas. Investimentos transformadores para um estilo de desenvolvimento sustentável: Estudos de casos de grande impulso (Big Push) para a sustentabilidade no Brasil. Brasília: CEPAL, 2020. LC/TS. 2020/37. p. 155-169, 2020.

[23] Souza JF de; Silva, R.M., Silva, A. M. Influência do uso e ocupação do solo na temperatura da superfície: o estudo de caso de João Pessoa - PB. Ambient constr [Internet]. 2016Jan;16(1):21–37. Available from: https://doi.org/10.1590/s1678-86212016000100058.

[24] Souza, B. S.; Cantalice, W. L. B. C.; Braga, C. C.; Silva, M. T.; Silva, E. A. Response of the EVI Vegetation Index to precipitation anomalies in the State of Paraíba. 2022. Journal of Hyperspectral Remote Sensing, 12 (1), 10-19.

[25] Tavares, Valter Cardoso et al. Desertificação, mudanças climáticas e secas no Semiárido brasileiro: uma revisão bibliográfica. 2019. Geosul, Florianópolis, 34 (70) 385-405. http://dx.doi.org/10.5007/2177-5230.2019v34n70p385

[26] Ventura, A.C., Andrade, J.C.S., 2011. Policultura no semiárido brasileiro. Field Actions Science Reports [online] 3. Disponível: http://factsreports.revues.org/2558. Acesso: 30 jun. 2023.

International Journal of Advanced Engineering Research and Science (IJAERS)
Peer-Reviewed Journal
ISSN: 2349-6495(P) | 2456-1908(O)
Vol-11, Issue-5; May, 2024
Journal Home Page Available: https://ijaers.com/
Article DOI: https://dx.doi.org/10.22161/ijaers.115.5

Quantum Machine Learning: Exploring Quantum Algorithms for Enhancing Deep Learning Models

Hari Gonaygunta*, Mohan Harish Maturi, Geeta Sandeep Nadella, Karthik Meduri, Snehal Satish[5]

Department of Information Technology, University of the Cumberlands, USA
*Email: hari.gonaygunta@ieee.org

Received: 03 Apr 2024,

Receive in revised form: 05 May 2024,

Accepted: 15 May 2024,

Available online: 23 May 2024

***Keywords*—Quantum Machine learning (QML), Deep learning, QNN, Qiskit. Estimator QNN, Sampler QNN**

***Abstract*—Using quantum algorithms to improve deep learning models' capabilities is becoming increasingly popular as quantum computing develops. In this work, we investigate how quantum algorithms using quantum neural networks (QNNs) might enhance the effectiveness and performance of deep learning models. We examine the effects of quantum-inspired methods on tasks, including regression, sorting, and optimization, by thoroughly analyzing quantum algorithms and how they integrate with deep learning systems. We experiment with Estimator QNN and Sampler QNN implementations using Qiskit machine-learning, analyzing their forward and backward pass outcomes to assess the effectiveness of quantum algorithms in improving deep learning models. Our research clarifies the scope, intricacy, and scalability issues surrounding QNNs and offers insights into the possible advantages and difficulties of quantum-enhanced deep learning. This work adds to the continuing investigation of quantum computing's potential to advance machine learning and artificial intelligence paradigms by clarifying the interaction between quantum algorithms and deep learning systems.*

I. INTRODUCTION

Two of the most exciting areas in computer science are quantum data processing and machine learning (Tychola et al., 2023). With the ability to use the laws of quantum physics to solve complicated computational problems, Quantum technology can change an array of various sectors ten times faster than regular computers. On the other hand, challenges like picture identification, natural language processing, and drug discovery have been remarkably solved by machine learning, especially deep learning (Liu et al., 2024).

Deep learning and quantum computing have fundamental constraints, notwithstanding their respective triumphs. Issues, including the curse of dimensionality, sluggish convergence rates, and the requirement for enormous volumes of labeled training data, are common to classical deep learning models (Valdez & Melin, 2023). Despite its unparalleled computational capacity, quantum computing is still in its infancy and faces obstacles, including noise, de-coherence, and difficulty scaling up quantum machines.

The combined characteristics of deep learning and quantum computing provide impetus for investigating their interaction. Using quantum phenomena like superposition and entanglement allows quantum computing to get around the restrictions imposed on classical computation (Jadhav et al., 2023). These characteristics may be used to create new algorithms that handle and analyze big datasets faster than their traditional equivalents.

Quantum machine learning methods may solve some of the core problems in deep learning. Quantum algorithms, for instance, may make feature mapping, reduce dimensionality, and optimize strategies more effectively, improving the functionality of deep neural networks.

Quantum machine learning is also promising for solving intrinsic quantum problems, including optimizing quantum circuits or mimicking quantum systems (Avramouli et al., 2023).

1.1 Research Motivations

Realizing the inherent constraints of classical computers and conventional deep learning approaches drives research at the nexus of quantum science and deep learning. Due to constraints like the exponential increase in computational resources needed for larger and more complicated optimization problems, traditional computers have difficulty processing large-scale datasets and solving these challenging issues. In the meantime, despite their great potential, deep learning models frequently suffer from problems including overfitting, sluggish convergence rates, and the requirement for large amounts of labeled training data (Santosh et al., 2022). By utilizing quantum dynamics entanglement and superposition, quantum computing enables a paradigm change in computing by allowing calculations to be completed tenfold more quickly than traditional computers (Liu et al., 2024). By investigating quantum algorithms to improve deep learning models, scientists hope to overcome these obstacles and uncover new possibilities for resolving challenging issues in various domains, from voice and picture recognition to medication development and optimization. The ultimate goal of this study is to push the limits of computation and machine learning to facilitate revolutionary advances in artificial intelligence and science.

II. BACKGROUND STUDY

Two important areas are explored in the background research for this work: deep learning and quantum technology. With the potential for exponential computational speedups, quantum computing uses the concepts of quantum physics to manipulate data in ways that traditional computers cannot (Egon et al., 2023). Meanwhile, by autonomously deriving abstractions from data, the deep learning tech is part of ML for impressive performance in several disciplines. Scaling problems, sluggish convergence rates, and the curse of dimensionality beset conventional deep learning models. By incorporating quantum computing concepts into deep learning frameworks, researchers hope to get beyond these constraints and open up new possibilities for improved performance and efficiency when tackling challenging tasks (Fikadu & Pandey, 2023). Laying the foundations for investigating quantum algorithms to improve deep learning models requires understanding the fundamental ideas and difficulties in both quantum computing and deep learning.

2.1 Quantum Computing Fundamentals

Based on concepts fundamentally different from classical computing, quantum computing uses the exciting field of quantum mechanics. Qubits, the quantum equivalents of classical bits, are the fundamental building blocks of quantum computing (Kharsa et al., 2023). Because of superposition, qubits can concurrently occupy many states, as opposed to traditional bits of information limited to two possible values: 0 and 1. This greatly increases the range of possible computations since a qubit may simultaneously be a mixture of 0 and 1. Quantum algorithms are based on superposition, enabling them to investigate several possible solutions to a problem simultaneously (Ramezani et al., 2020).

Quantum bits and superposition: It can display entanglement, a distinctive quantum phenomenon in which the states of two qubits are inextricably connected regardless of their distance. This phenomenon greatly increases the computing capabilities of quantum computers by allowing them to execute coordinated operations on entangled qubits. By utilizing these characteristics, quantum computing can potentially address computationally demanding issues beyond the capabilities of conventional computers (Zahorodko et al., 2021). The possibilities for quantum computing are enormous and potentially revolutionary, ranging from modeling intricate quantum systems to optimizing massive logistical networks.

Solving major technical obstacles, such as de-coherence and error correction, as well as creating scalable quantum technology, are necessary to realize this promise. Research on quantum computing is still driven by the fascination of using qubits and superposition to solve problems and open up new computational and problem-solving possibilities (Avramouli et al., 2023).

2.2 Quantum Gates and Circuits

Modern doors and quantum systems are the fundamental components of quantum computing, providing the means of controlling qubits and carrying out calculations. Quantum gates are simple procedures that change the state of qubits, much like logic gates are used in conventional computers to carry out logical operations (Alchieri et al., 2021). Quantum gates can execute operations that use the special characteristics of quantum physics, in contrast to classical gates, which operate on bits (0s and 1s) in Figure 1.

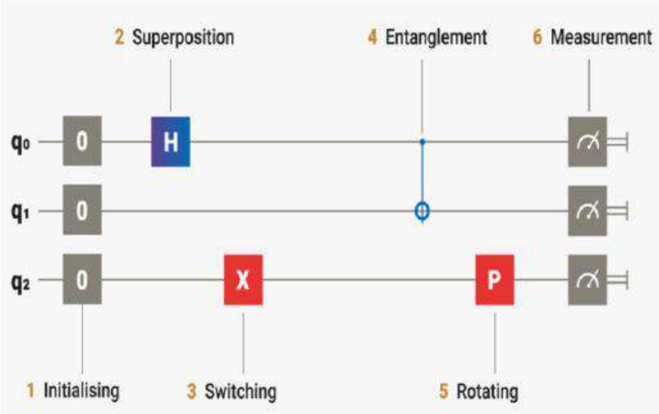

Fig.1: Quantum Gates and Circuits

The Hadamard gate, which produces limbo by changing a qubit from a definite state (0 or 1) to a state that mixes 0 and 1, is one of the basic quantum gates (Jerbi et al., 2021). This gate is essential for creating quantum states that allow for simultaneous exploration of many solutions and parallel computing. Similar to the traditional NOT gate, the Pauli-X gate is another crucial gate that allows a qubit to be switched from 0 to 1 or vice versa (Buffoni & Carus, 2021) to accomplish desired functions on qubits, quantum circuits are chains of quantum gates organized in a certain order. Qubits are shown as lines in these circuit representations, and gates are shown as symbols operating on these lines (Khan & Robles-Kelly, 2020). The order and configuration of gates in a quantum circuit dictate how the computation is performed.

Quantum circuits of different gates are used to develop fundamentals, such as the infinite integer factoring technique proposed by Fried and the randomized algorithm for searching developed by Grover (Batra et al., 2021). Gather, which happens whenever a number of the qubits are connected to the point that their current conditions rely on each other even if particles differ by enormous distances, is a further significant idea in quantum devices. Due to their ability to generate and modify entangled states, quantum gates are useful for applications like quantum cryptography and teleportation (Dunjko & Wittek, 2020).

2.3 Challenges in Deep Learning

Despite its astounding achievements, in Figure 2, deep learning still has several issues that prevent mainstream acceptance and use in various fields (Liu et al., 2024). Among these difficulties are:

Data Availability: Deep learning models need much-labeled data to discover patterns and provide precise predictions. Getting tagged data may be expensive, time-consuming, and sometimes not feasible (Surjeet et al., 2024). Labeled data might not always be easily accessible for certain tasks or domains, a major obstacle to deep learning model training.

Fig.2: Challenges in deep learning models

High-Performance Hardware: Large computing resources, such as powerful GPUs or specialized hardware like TPUs (Tensor Processing Units), are frequently required to train deep learning models (Bishwas et al., 2020). For smaller businesses or academics with limited funding, deep learning solutions may not be as scalable due to the high cost of obtaining such gear. This problem is made more difficult by the increasing need for more powerful hardware as deep learning models become larger and more complicated (Gil-Fuster et al., 2024).

Suboptimal Hyper-parameter Optimization: Many parameters that control the construction, method of training, and evaluation process of deep learning models are usually involved. Optimizing the hyperparameter combination can greatly influence how well the model performs. Manually adjusting hyperparameters takes time and effort and frequently calls for domain knowledge and experience (Lewis et al., 2024). Although there are automated methods for optimizing hyperparameters, their effectiveness may not always be guaranteed, resulting in less-than-ideal model performance.

Data Security and Privacy: Data privacy and security are challenges raised by deep learning models trained on private or sensitive data. Protecting the privacy and integrity of data fit for training and test inference is critical as deep-learning models proliferate in various applications, such as cybersecurity, finance, and healthcare. Strong data security procedures are even more crucial in light of worries about possible weaknesses, hostile assaults, and unintentional biases in deep learning models (Dave, 2022).

III. RESEARCH METHODOLOGY

This study's research approach uses a series of discrete phases to investigate Qiskit, a quantum computing framework, to investigate the use of quantum neural networks for classification problems (Wichert, 2023). There are several intriguing ways to improve deep learning models using quantum algorithms. First, using quantum parallelism and entanglement to build deep learning models might speed up optimization processes, leading to faster convergence and more effective model training. Second, using quantum computing's enhanced capacity to handle high-dimensional data, approaches such as quantum feature mapping and dimensionality reduction enable more effective feature representation and decrease computational complexity (Das, 2023). The ability to encode conventional data into quantum states is made possible by quantum data encoding techniques, which may make data processing and representation in quantum-based models more effective. The following is an outline of the methodology:

3.1 Quantum Algorithms for Enhancing Deep Learning

With linked nodes or neurons structured in layers, traditional neural networks are used for computation statements motivated by social intellect and capable of identifying patterns in data and solving complicated problems (Priyanka, 2023). Modifying parameters with machine learning or deep learning approaches teaches these networks.

Quantum Machine Learning (QML) aims to combine ideas from conventional and quantum computers to develop and improve learning approaches (Beer et al., 2020). This merging is embodied by Quantum Neural Networks (QNNs), which combine parametrized quantum circuits with conventional neural networks. QNNs are positioned at the nexus of two domains and provide two views:

From the machine learning perspective, figure 3 QNNs work similarly to classical models in that they are computationally trained to find underlying patterns in data. As shown in Figure 2, they function by loading classical input into quantum states, processing it with quantum gates defined by adaptable weight, and measuring the output state.

3.2 Data Loading

When discussing data loading concerning Estimator QNN, we mean converting traditional input data into a quantum processing-ready format. This entails converting traditional data into quantum states controlled by the QNN's configured quantum circuit (Das, 2023). The input settings provided during creation are used to initialize the quantum circuit, enabling it to handle the quantum-ready data following its design and specifications. This is important because it bridges the Quantum and classical worlds, allowing the QNN to deal with classical data in a quantum context and explore quantum-enhanced learning techniques.

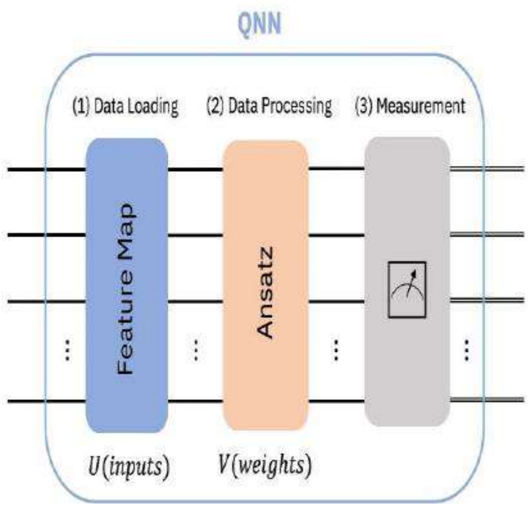

Fig.3: QNN Model

The Estimator QNN computes expectation values for the forward pass based on a possible hybrid mechanics variable and a parametric quantum network as inputs. Lists of observables may also be entered into the Estimator QNN to create more intricate QNNs.

Let us use a basic example, Figure 4, to demonstrate how an Estimator QNN works. Building the parametrized circuit is where we begin. Two parameters make up this quantum circuit: one denotes a Q-N-N contribution, and the additional a trainable load.

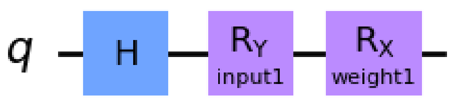

Figure 4: QNN input

Now that we have defined the expected value computation, we can construct an observable. The Estimator QNN will automatically create the default observable if it is not set. The number of qubits in this quantum circuit is n.

3.3 Data preprocessing

Two primary phases are involved in data preparation for quantum neural networks (QNNs) based on the code snippets that have been provided:

Data Encoding into Quantum States: For quantum circuits to handle input data in the context of QNNs, classical data must be converted into a quantum description. Shifting classical data onto quantum states is a common step in an encoding procedure. This can be done using volume-encoded data, angle coding, or other encoding approaches (Weigold et al., 2021). This phase is demonstrated in the given code when using QuantumCircuit from Qiskit to create the quantum circuits (qc1 and qc2) to process the quantum-ready data during the forward pass, and these circuits are initialized with parameters (params1 and inputs2) that reflect the classical input data.

Quantum Circuit Parameterization: The quantum circuits of the QNN process the classical data once it has been encoded into quantum states. These quantum circuits are parametrized, which means that the variables (weights) are changed within the training phase to maximize the network's performance for the assigned job (Shi et al., 2023). The given code builds the quantum circuits (qc1 and qc2) using parameters (params1 and inputs2) and then modifies them using gates like R_X and R_y to represent the QNN's processing phases. The network's performance is then enhanced by training these parameters using optimization methods like backpropagation to minimize a specified loss function.

3.4 Implementation and Measurement

Quantum Neural Networks (QNNs), which are application-agnostic compute units tailored to various use cases, are available through the Qiskit Machine Learning package. These QNNs have two distinct implementations that are organized around an interface:

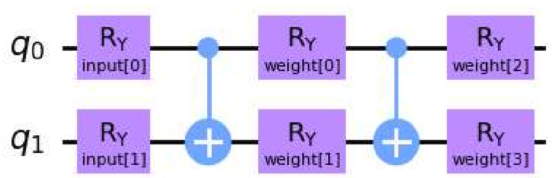

Fig.5: Input QNN Estimator QNN

Neural Network: This is the interface for all neural networks within the Qiskit Machine Learning framework. It is an abstract class from which all QNNs inherit.

Estimator QNN: This implementation evaluates quantum mechanical observables for its operations.

Sampler QNN: In contrast, depending on the data acquired by testing a quantum computing circuit, Sampler-QNN functions.

Estimator QNN and Sampler-QNN software versions use Qiskit primitives from Figure 5, the building blocks for running QNNs on simulators or real quantum hardware. Each of these implementations accepts an extra class of the appropriate basic, Base-Sampler for Sampler QNN and Base Estimator for Estimator QNN (Innan et al., 2023). The QNN classes automatically instantiate the proper reference primitive (Sampler or Estimator) for smooth operation if no instance is explicitly supplied. Let us explore the theory of utilizing a Quantum Neural Network (QNN) in Qiskit Machine algo to do a forward and backward pass together (Abbas et al., 2021). We will review the underlying idea of these procedures and provide code examples.

Forward Pass

In a QNN, a forward move entails calculating the output, transferring the input data via the quantum circuit, and maybe doing some afterward. This is how it operates:

Input Preparation: Quantum states—typically represented as qubits in a quantum circuit—are created by encoding the incoming data. A characteristic of the incoming data may be correlated with each qubit.

Quantum Circuit Execution: The quantum circuit's training weights determine the encoded quantum states' processes.

Measurement: The quantum circuit is executed, and then the qubits are measured. The results of these measurements yield classical data that can be handled further.

The output of the Sampler QNN is a probability distribution across all potential measurement results, with each element representing the likelihood of detecting a particular measurement outcome. The output vector in this instance is shaped like (1, 4), meaning that there is one sample and four potential measurement results. The corresponding probability for each possible event is around 0.018, 0.257, 0.527, and 0.198. Conversely, the Estimator QNN yields a single probability value for every input sample. The output vector's structure of (2, 1) denotes that two input samples were processed concurrently, with one probability value computed for each sample. In this instance, the probability value obtained from both samples is around 0.297.

Backward Pass:

The backward pass in a QNN involves calculating gradients of the loss function concerning the quantum circuit's trainable parameters (weights). Here is how it works:

Compute Loss: First, the loss function is computed using the predicted output from the forward pass and the target output.

Gradient Calculation: Grades of the loss functions through deference to the trainable limits (weights) are calculated using methods like backs-propagation shown in Figure 6.

Parameter Update: The gradients are used to update the parameters of the quantum circuit to minimize the loss function.

```
Input gradients for SamplerQNN: [[[-0.05844702 -0.10621091]
                [ 0.38798796 -0.19544083]
                [-0.34561132  0.09459601]
                [ 0.01607038  0.20705573]]].
                Shape: (1, 4, 2)
Weight gradients for SamplerQNN: [[[ 0.00606238 -0.1124595  -0.06856156 -0.09809236]
                [ 0.21167414 -0.09069775  0.06856156 -0.22549618]
                [-0.48846674  0.32499215 -0.32262178  0.09809236]
                [ 0.27073021 -0.12183491  0.32262178  0.22549618]]].
                Shape: (1, 4, 4)
```

Figure 6: Gradient model training

The quantum neural network (QNN) propagates input data forward during each epoch, and then gradients calculated by gradient descent propagate backward. The objective is to repeatedly adjust the QNN's parameters to reduce the loss function and enhance its functionality. Attaining an accuracy score of 83% signifies that the QNN has successfully learned to categorize or predict outcomes with a high degree of accuracy after several training epochs. The QNN may effectively modify its parameters to better suit the training data by utilizing Gradient Descent, which improves the QNN's performance in deep learning tasks.

IV. CONCLUSION

In summary, the depth and complexity of quantum neural networks (QNNs) are critical to their effectiveness and generalizability in various applications. The quantity of layers in a neural network architecture—conventional and Quantum—is called the QNN's depth. Deeper QNNs are often associated with a higher ability to identify complex patterns and correlations in the input data, which may enhance performance on challenging tasks. Moreover, there are drawbacks to deepening a QNN, including greater computing complexity, noise sensitivity, and the possibility of gradients disappearing or ballooning during training.

The debate on QNN depth entails weighing the trade-offs between computational viability and model expressiveness. The potential for improved representation capacity in deeper QNNs allows them to take on more difficult learning tasks and extract higher-level features from the data. However, the effective use of deep QNNs necessitates strong optimization methods, effective resource management, and noise and quantum error mitigation approaches to guarantee realistic scalability and practicality in quantum computing platforms; the depth of QNNs must be matched with the quantum resources available, such as the number of qubits, circuit coherence times, and gate fidelities.

REFERENCES

[1] Abbas, A., Sutter, D., Zoufal, C., Lucchi, A., Figalli, A., & Woerner, S. (2021). The power of Quantum Neural Networks. *Nature Computational Science*, *1*(6), 403–409. https://doi.org/10.1038/s43588-021-00084-1

[2] Alchieri, L., Badalotti, D., Bonardi, P., & Bianco, S. (2021). An introduction to quantum machine learning: From Quantum Logic to Quantum Deep Learning. Quantum Machine Intelligence, 3(2). https://doi.org/10.1007/s42484-021-00056-8

[3] Avramouli, M., Savvas, I. K., Vasilaki, A., & Garani, G. (2023). Unlocking the potential of quantum machine learning to advance drug discovery. Electronics, 12(11), 2402. https://doi.org/10.3390/electronics12112402

[4] Batra, K., Zorn, K. M., Foil, D. H., Minerali, E., Gawriljuk, V. O., Lane, T. R., & Ekins, S. (2021). Quantum machine learning algorithms for Drug Discovery Applications. Journal of Chemical Information and Modeling, 61(6), 2641–2647. https://doi.org/10.1021/acs.jcim.1c00166

[5] Beer, K., Bondarenko, D., Farrelly, T., Osborne, T. J., Salzmann, R., Scheiermann, D., & Wolf, R. (2020). Training Deep Quantum Neural Networks. Nature Communications, 11(1). https://doi.org/10.1038/s41467-020-14454-2

[6] Bishwas, A. K., Mani, A., & Palade, V. (2020). 4. from classical to Quantum Machine Learning. Quantum Machine Learning, 67–88. https://doi.org/10.1515/9783110670707-004

[7] Buffoni, L., & Caruso, F. (2020). New trends in Quantum Machine Learning ^(a). Europhysics Letters, 132(6), 60004. https://doi.org/10.1209/0295-5075/132/60004

[8] Das, P. (2023). Design and Comparative Analysis of Quantum Hashing Algorithms Using Qiskit. https://doi.org/10.36227/techrxiv.24037440.v1

[9] Dave, R. (2022). Machine Learning Applications of Data Security and Privacy a Systemic Review. https://doi.org/10.36227/techrxiv.20063219.v1

[10] Dunjko, V., & Wittek, P. (2020). A non-review of Quantum Machine Learning: Trends and explorations. Quantum Views, 4, 32. https://doi.org/10.22331/qv-2020-03-17-32

[11] Egon, K., ROSINSKI, J., KARL, L., & EUGENE, R. (2023). Quantum Machine Learning: The Confluence of Quantum Computing and Ai. https://doi.org/10.31219/osf.io/rf4xp

[12] Fikadu Tilaye, G., & Pandey, A. (2023). Investigating the effects of hyperparameters in quantum-enhanced deep reinforcement learning. Quantum Engineering, 2023, 1–16. https://doi.org/10.1155/2023/2451990

[13] Gil-Fuster, E., Eisert, J., & Bravo-Prieto, C. (2024). Understanding Quantum Machine Learning also requires rethinking generalization. Nature Communications, 15(1). https://doi.org/10.1038/s41467-024-45882-z

[14] Innan, N., Khan, M. A.-Z., & Bennai, M. (2023). Financial fraud detection: A comparative study of quantum machine learning models. International Journal of Quantum Information, 22(02). https://doi.org/10.1142/s0219749923500442

[15] Jadhav, A., Rasool, A., & Gyanchandani, M. (2023). Quantum Machine Learning: Scope for real-world problems. Procedia Computer Science, 218, 2612–2625. https://doi.org/10.1016/j.procs.2023.01.235

[16] Jerbi, S., Trenkwalder, L. M., Poulsen Nautrup, H., Briegel, H. J., & Dunjko, V. (2021). Quantum enhancements for deep reinforcement learning in large spaces. PRX Quantum, 2(1). https://doi.org/10.1103/prxquantum.2.010328

[17] Jhanwar, A., & Nene, M. J. (2021). Enhanced machine learning using quantum computing. 2021 Second International Conference on Electronics and Sustainable Communication Systems (ICESC). https://doi.org/10.1109/icesc51422.2021.9532638

[18] Khan, T. M., & Robles-Kelly, A. (2020). Machine learning: Quantum vs classical. IEEE Access, 8, 219275–219294. https://doi.org/10.1109/access.2020.3041719

[19] Kharsa, R., Bouridane, A., & Amira, A. (2023). Advances in quantum machine learning and deep learning for image classification: A survey. Neurocomputing, 560, 126843. https://doi.org/10.1016/j.neucom.2023.126843

[20] Lewis, L., Huang, H.-Y., Tran, V. T., Lehner, S., Kueng, R., & Preskill, J. (2024). Improved machine learning algorithm for predicting ground state properties. Nature Communications, 15(1). https://doi.org/10.1038/s41467-024-45014-7

[21] Liu, J., Liu, M., Liu, J.-P., Ye, Z., Wang, Y., Alexeev, Y., Eisert, J., & Jiang, L. (2024). Towards provably efficient quantum algorithms for large-scale machine-learning models. Nature Communications, 15(1). https://doi.org/10.1038/s41467-023-43957-x

[22] Priyanka, G. S., Venkatesan, M., & Prabhavathy, P. (2023). Advancements in quantum machine learning and Quantum Deep Learning: A Comprehensive Review of Algorithms, challenges, and future directions. 2023 International Conference on Quantum Technologies, Communications, Computing, Hardware and Embedded Systems Security (iQ-CCHESS). https://doi.org/10.1109/iq-cchess56596.2023.10391745

[23] Rahmaniar, W., Ramzan, B., & Ma'arif, A. (2024). Deep learning and quantum algorithms approach to investigating the feasibility of wormholes: A Review. Astronomy and Computing, 47, 100802. https://doi.org/10.1016/j.ascom.2024.100802

[24] Ramezani, S. B., Sommers, A., Manchukonda, H. K., Rahimi, S., & Amirlatifi, A. (2020). Machine learning algorithms in Quantum Computing: A survey. 2020 International Joint Conference on Neural Networks (IJCNN). https://doi.org/10.1109/ijcnn48605.2020.9207714

[25] Santosh, K., Das, N., & Ghosh, S. (2022). Deep learning models. Deep Learning Models for Medical Imaging, 65–97. https://doi.org/10.1016/b978-0-12-823504-1.00013-1

[26] Shi, J., Li, Z., Lai, W., Li, F., Shi, R., Feng, Y., & Zhang, S. (2023). Two end-to-end quantum-inspired deep neural networks for text classification. IEEE Transactions on Knowledge and Data Engineering, 35(4), 4335–4345. https://doi.org/10.1109/tkde.2021.3130598

[27] Surjeet, S., Bulla, C., Arya, A., Idrees, S., Singh, G., Rao, S. G., & Shirahatti, A. (2023, March 6). A quantum machine learning approach for bridging the gap between Quantum and classical computing. International Journal of Intelligent Systems and Applications in Engineering. http://www.ijisae.org/index.php/IJISAE/article/view/4539

[28] Tychola, K. A., Kalampokas, T., & Papakostas, G. A. (2023). Quantum Machine Learning—an overview. Electronics, 12(11), 2379. https://doi.org/10.3390/electronics12112379

[29] Valdez, F., & Melin, P. (2022). A review on quantum computing and deep learning algorithms and their applications. Soft Computing, 27(18), 13217–13236. https://doi.org/10.1007/s00500-022-07037-4

[30] Weigold, M., Barzen, J., Leymann, F., & Salm, M. (2021). Expanding data encoding patterns for quantum algorithms. 2021 IEEE 18th International Conference on Software Architecture Companion (ICSA-C). https://doi.org/10.1109/icsa-c52384.2021.00025

[31] Wichert, A. (2023). Qiskit. Quantum Artificial Intelligence with Qiskit, 41–62. https://doi.org/10.1201/9781003374404-3

[32] Zahorodko, P. V., Semerikov, S. O., Soloviev, V. N., Striuk, A. M., Striuk, M. I., & Shalatska, H. M. (2021). Comparisons of performance between quantum-enhanced and classical machine learning algorithms on the IBM Quantum experience. Journal of Physics: Conference Series, 1840(1), 012021. https://doi.org/10.1088/1742-6596/1840/1/012021

[33] Zeguendry, A., Jarir, Z., & Quafafou, M. (2023). Quantum Machine Learning: A Review and Case Studies. Entropy, 25(2), 287. https://doi.org/10.3390/e25020287

International Journal of Advanced Engineering Research and Science (IJAERS)
Peer-Reviewed Journal
ISSN: 2349-6495(P) | 2456-1908(O)
Vol-11, Issue-5; May, 2024
Journal Home Page Available: https://ijaers.com/
Article DOI: https://dx.doi.org/10.22161/ijaers.115.6

A Web-Based "Department Management System" for Academic Institutions

Kulkarni Rohini, Shelke Aditi, Mane Rutuja, Kulkarni Shruti, Prof. D.P. Kulkarni

Department of Computer Engineering, Karmayogi Institute of Technology, DBATU University, Lonere, Maharashtra, India
Email: rohinikulkarni133@gmail.com

Received: 08 Apr 2024,

Receive in revised form: 10 May 2024,

Accepted: 17 May 2024,

Available online: 25 May 2024

Keywords— *Department Management System, DMS, DEPT, MGMT, Management System.*

Abstract— *This work done is pointed toward fostering a web-based Online application "Division The executives Framework" that is of significance to explicit branch of school. The framework is electronic application that can be gotten to all through the division of an association. This framework might be utilized for checking the general exercises as well as execution of the understudies. This work is being produced for a designing to keep up with and work with simple admittance to data. For this the clients should be enrolled with the framework after which they can access as well as alter information according to the consents given to them. DMS is an online application that targets giving data to every one of the degrees of division in an association. For a given understudy/personnel can get to the framework to either transfer or download some data from the information base.*

I. INTRODUCTION

The title of the project Department Management System is characterized as an application expands on web that is helpful in giving data at all levels of a division. For the clients of this framework the manager makes login IDs and particular passwords from which understudy/staff can undoubtedly get to the framework. This work is basically a website which includes attractive designs and proper arrangements of links and images from staff rating to, every notice and upcoming events is showcased in this system. Student user interface, allowing users to access Information and submit requests online thus reducing processing time.

HOD Dashboard – The HOD having privileges to manage or perform the activities related to staff and student and department.

Staff Dashboard – The Staff having privileges to manage or perform the activities related to student.

Student Dashboard – The student can see their Presenty, can access the syllabus, can access the assignment. They do not have privileges to change the date only access the data.

II. METHODOLOGY

1. Software Requirement Specification:

A Bunch of programs associated with the operation of a computer is called software. Software is the part of the computer system, which enables the user to interact with several physical hardware devices. The minimum software requirement specifications for developing this project are as follows:

Operating System: Windows 11 Presentation Layer: PHP, CSS, HTML, JS

Tool: MS Office

2. Hardware Requirement Specification:

The collection of internal electronic circuits and external physical devices used in building a computer is called the Hardware. The minimum hardware requirement specifications for developing this project are as follows:

Processor: Standard processor with a speed of 1.6 GHz RAM: 256 MB RAM or more

Hard Disk: 20 GB or more Monitor: Standard color monitor Keyboard: Standard keyboard Mouse: Standard mouse

III. FIGURES AND TABLES

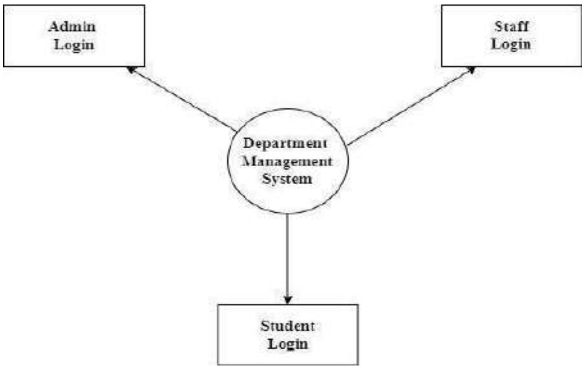

Fig. 1: DFD Level 0

In DMS there are 3 modules named as Admin login, staff login, and Student login.

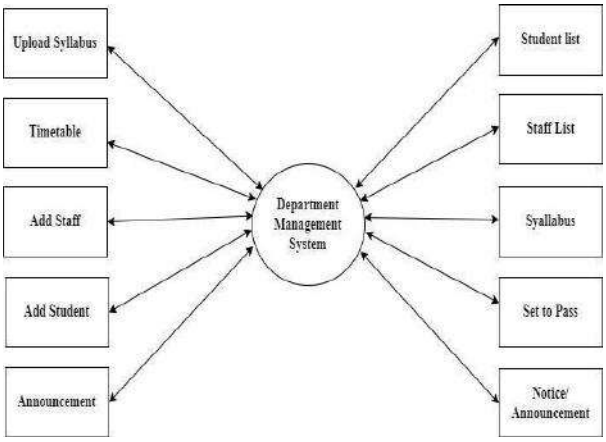

Fig 2: DFD Level 1

In DFD level 1 consisting multiple entities. Mainly forms following entities upload syllabus, Timetable, add staff, add student, announcement, staff list ,etc.

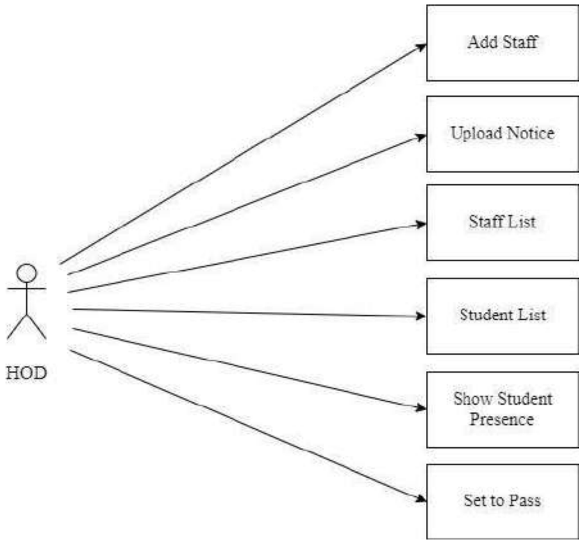

Fig. 3: Use case of HOD

In the above fig 3 above mentioned entities handled by HOD (admin).

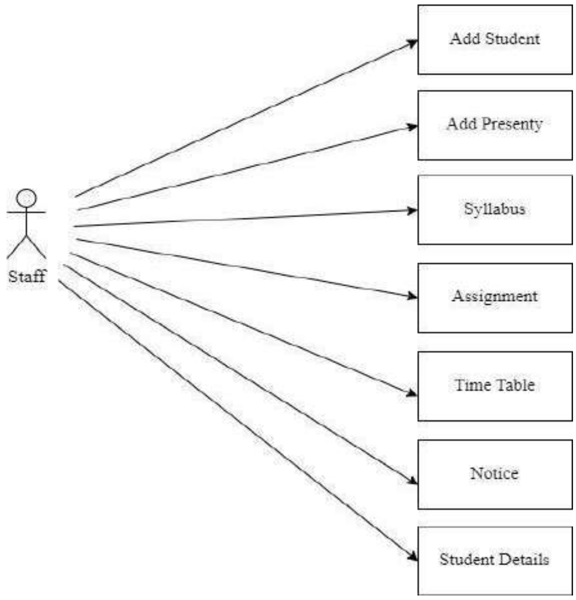

Fig 4: Use case of Staff

In this fig 4 staff can have different authorities are given those are as above mentioned.

IV. RESULTS

Home Page:

HOD Dashboard:

V. CONCLUSION

The project entitled as Department Management System is Web based Application that deals with issues related to manual working in college department. This project is successfully implemented with all the features mentioned in application. The application provides appropriate information to user according to the desired service. The project is designing doing the day-by-day activity problem faced by in college department. Deployment of our application will certainly help the department to reduce unnecessary wastage of time, paper work etc. So, this serves the right purpose in achieving the desire requirement of both communities. Also, we can generate the report of all information.

ACKNOWLEDGEMENTS

At the pleasing moment of having completed my project, I wish to convey my sincere thanks and gratitude towards the management of our college who provided all the possibilities and wisdom to us. First and foremost, my sincere thanks to the principal Dr. S.P. Patil sir forwarding us to do our project and offering adequate duration to fully complete my project. We are also grateful to the Head of Department of CSE prof. D. V. Bhosale sir for his constructive suggestions and encouragement during our project work. Last but not least we would like to thanks to all the staff of the Karmayogi Engineering College, and our friends for increased and propels and encouragement throughout in this position.

REFERENCES

[1] https://www.google.com/search?q=depatment+managemnt+system&rlz=1C1RXQR_enIN1094IN1094&oq=depatment+managemnt+system+&gs_lcrp=EgZjaHJvbWUyBggAEEUYOdIBCjE3Njk3ajBqMTWoAgiwAgE&sourceid=chrome&ie=UTF-8

[2] A.V.Shivasane, Feb-2018, College Department Management System, International Research Journal of Engineering and Technology (IRJET), Volume 05 Issue 02 https://www.irjet.net/archives/V5/i2/IRJET-V5I250.pdf

[3] Kartiki Datarkar, April 2016, Online college management system, International Journal of Computer Science and Mobile Computing, IJCSMC, Volume 5, Issue no. 4, April 2016, pg.118 – 122 https://www.ijcsmc.com/docs/papers/April2016/V5I4201657.pdf

[4] Jigar Makhija, 0ctober 2015, IICT Department Management website https:// www.slideshare.net / jigarmakhija/college-department-management-system.

International Journal of Advanced Engineering Research and Science (IJAERS)
Peer-Reviewed Journal
ISSN: 2349-6495(P) | 2456-1908(O)
Vol-11, Issue-5; May, 2024
Journal Home Page Available: https://ijaers.com/
Article DOI: https://dx.doi.org/10.22161/ijaers.115.7

Effect of Charging Current Variation on Internal Resistance in Lithium-Ion Batteries

Keshawa Udiatma, S.T.[1], Trias Andromeda, S.T., M.T., Ph.D.[2], Dr. Iwan Setiawan, S.T., M.T.[3]

[1]Department of Electrical Engineering, Diponegoro University, Indonesia
Email: keshawaudiatmaa@gmail.com
[2]Department of Electrical Engineering, Diponegoro University, Indonesia
Email : triasandromeda@lecturer.undip.ac.id
[3]Department of Electrical Engineering, Diponegoro University, Indonesia
Email : iwansetiawan@lecturer.undip.ac.id

Received: 09 Apr 2024,

Receive in revised form: 11 May 2024,

Accepted: 22 May 2024,

Available online: 31 May 2024

***Keywords*— Current, Internal Resistance, Charging, State of Health, Lithium-Ion.**

***Abstract*— *Internal resistance of a battery is affected by the amount of charging current and how many charge cycles are carried out. The value of internal resistance is also related to the State of Health (SoH) of the battery. The smaller value of internal resistance indicates a higher SoH of the battery. This paper presents a comparison of internal resistance due to variation of charging current. The current values are 500 mA, 1000 mA, and 3000 mA. Lithium-ion 18650 batteries which have capacity 1200 mAh are charged by these current values. Three batteries are used using three scenarios, namely the 500 mA for scenario 1 using the Liitokala-Lii500 charger, 1000 mA for scenario 2 using the Liitokala-Lii500 charger, and the 3000 mA for scenario 3 using the XL4016 constant current (CC) constant voltage (CV) charger. Every battery is charged 20 times. Internal resistance of each battery is measured using YAOREA YR1030 module during experimental work. The data experiments indicate that variation of current of 500 mA for scenario 1, internal resistance is increased by 1 mΩ. Scenario 2, 1000 mA, internal resistance will extend by 1.4 mΩ. Scenario 3 which uses 3000 mA, gives the highest internal resistance alteration by 2.1 mΩ. It can be concluded that the greater values of charging current will affect a higher value of internal resistance.*

I. INTRODUCTION

Recently, batteries are widely used for electrical energy storage. Batteries can be easily applied to existing electronic devices and convenience to users.

Batteries have many types depending on the use to be used, but batteries also have an age where the battery is still suitable for use or not, battery life is usually called State of Health (SoH). SoH has many parameters to determine whether the battery has good performance or has decreased performance including the value of internal resistance, internal resistance is one of the parameters that shows the ability of the battery to conduct electric current. The lower the value of the internal resistance, the better the battery's ability to flow current. The higher the internal resistance value also affects the decrease in battery performance to flow current, the energy lost due to the large value of the internal resistance will be converted into heat, which makes the battery heat faster and battery performance will decrease. Lithium-ion 18650 batteries were used in research because they have several advantages, namely fast charging, long battery life, and higher power density.

But in addition to the advantages of lithium-ion batteries, lithium-ion batteries also have some disadvantages, namely temperatures that can increase quickly, prone to overcharge which can damage the battery, prone to explode if too hot. The selection of the 18650 battery is based on the experience of researchers that the 18650 battery has better battery life for performing charge and discharge cycles with large quantities, and also has a more diverse reference module measurement circuit than other types of batteries. The author chose to use the constant current constant voltage charger method because this method is considered the safest method for batteries because it combines 2 charging methods that can avoid overcharge if the battery remains installed in the module when the condition is fully charged.

II. RESEARCH METHODS

The research method will be divided into two parts, namely theoretical basis and research flow.

2.1 Theoretical Basis

2.1.1 Lithium-Ion Battery

The batteries used in this research are *lithium-ion* 18650 type batteries. This type of battery falls into the category of rechargeable batteries. *Lithium-Ion* batteries are widely used in electronic devices that require high power and have a long lifespan. The name "18650" refers to the physical dimensions of the battery, which are 18 *mm* in diameter and 65 *mm* in height, with "0" indicating high tolerance. For example, these batteries have a longer lifespan when used in electronic circuits equipped with protection [1].

These batteries have a standard operating voltage of 3.7 *V* and a maximum operating voltage of 4.2 *V* when fully charged. When the voltage is between 2.8 *V* and 3 *V*, it indicates that the battery is empty. The maximum capacity of these batteries is known to reach 3600 *mAh*, which means the battery can provide an electrical current of 3600 *mA* for one hour of use [1].

The basic component of these batteries is *lithium-ion*, which can be combined with other chemicals such as *cobalt*, *manganese*, and so on. The advantage of this material is its large storage capacity and it does not have detrimental memory effects after several charging and discharging cycles. However, these batteries are susceptible to the risk of fire under certain conditions [1].

2.1.2 Internal Resistance

Internal resistance is a crucial parameter for assessing the health condition of a battery. Generally, the lower the internal resistance, the better the battery is at delivering current to electronic devices. Conversely, if the internal resistance increases, the battery will struggle to deliver current to electronic devices and may cause excessive heat in the battery [2]. This determines whether the battery can still be used and provides an indication of its lifespan.

Measuring the internal resistance of a battery can be done by using a circuit where the batteries are connected in a closed loop, with the load directly connected to the battery.

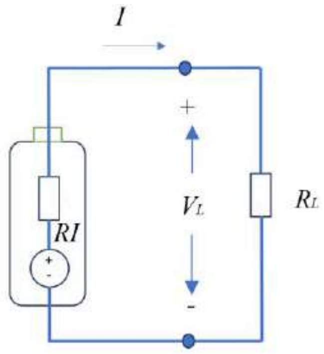

Fig. 1: Internal resistance tester circuit

In Fig. 1, we can add an *RL* load to calculate the magnitude of the internal resistance (*RI*) of the battery. First, we will use *Ohm*'s law to find the value of the current (*I*) flowing from the battery to the *RL* load, and the calculation can be seen in the following equation (2.1) :

$$I = VL \;/\; RL \qquad (2.1)$$

After determining the magnitude of the current (*I*) flowing from the battery to the load, the next step is to calculate the voltage drop across the internal resistance. The principle used to calculate the voltage drop is using *Kirchoff*'s law, which states that the voltage drop across both resistors, *RI* and *RL*, must be equal to the ideal battery voltage. This voltage drop will be symbolized by *VI*. Where *Voc* is the voltage reading when the circuit is open, measured manually using a multimeter. Thus, the calculation to determine the value of *VI* or the voltage drop can be seen in the following equation (2.2) :

$$VDROP = VOC - VL \qquad (2.2)$$

After determining the value of the voltage drop that occurs across the internal resistance, the next step is to find the value of the internal resistance (*RI*) using *Ohm*'s law. This can be calculated using equation (2.3) as follows :

$$RI = VDROP \,/\, I \qquad (2.3)$$

After the calculation above, the value of its internal resistance can be determined. This value determines whether the battery is still usable or not, as a higher internal resistance leads to poorer battery performance.

The increase in internal resistance value in the battery is typically influenced by the charging and discharging cycles, age, and battery temperature.

2.1.3 Buck Converter XL4016 CCCV

The charger module used in this study is the XL4016 Buck Converter Constant Current Constant Voltage (CCCV) module. This module has the main function of converting the DC value of a system to be smaller than its input voltage, or in other words, reducing the input voltage [3]. The XL4016 module has two loops or multilevel feedback, the inner loop, which controls current, and the outer loop, which controls output voltage. The XL4016 module is depicted in Fig. 2. below.

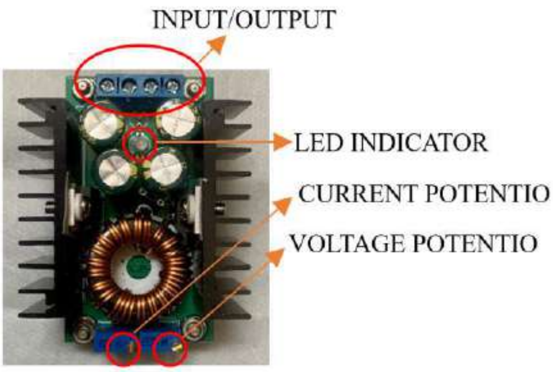

Fig. 2: Buck converter XL4016 module

The XL4016 module has two components potentiometer that functions to adjust the output voltage and another potentiometer that functions as a current limiter generated by the buck converter. The working principle of the XL4016 module is as follows,

a. Outer Loop (CV mode)

If the load connected to the module is a resistive load, with a resistance value large enough approaching infinity, then the resulting voltage at the control block will be relatively small, and this control value will become the current reference value. The module will activate constant voltage mode, meaning the output voltage will track this reference.

b. Inner Loop (CC mode)

If the load connected to the module is a resistive load, with a resistance value very small approaching zero, then the result from the voltage feedback control will produce a relatively large control signal (approaching infinity). However, because the control signal passes through the current saturation block or limiter, what is passed to the inner loop is the flowing current, which does not exceed the current limit set on the current potentiometer. The module will activate constant current mode.

In conclusion, constant voltage (CV) mode will be active when the current value is below the current limit, while constant current (CC) mode will be active when the current reaches the current limit, indicating that the battery charging mode has reached a full or charged condition.

2.2 Research Flow

The research procedure begins with determining the type of battery to be used, namely the *lithium-ion* 18650 battery with a capacity of 1200 *mAh*. Subsequently, the internal resistance value of the battery is measured using the YAOREA YR1030+ Internal Resistance Tester before the charging process. Ensure that the battery is in a discharged state before conducting the internal resistance measurement. The results of the internal resistance measurement of the battery can be seen in Fig. 3. below.

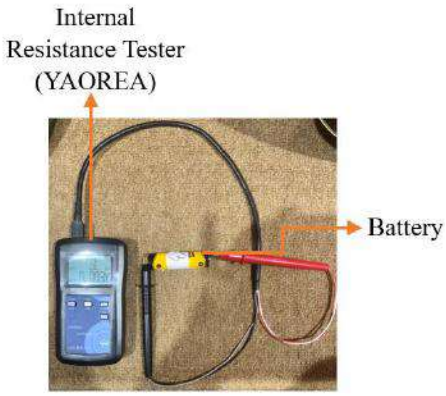

Fig. 3: Measuring battery internal resistance

After obtaining the initial values of internal resistance and battery voltage before the charging process, the next step is to install the battery for scenarios 1 and 2, which involve current variations of 500 *mA* and 1000 *mA*, using the Liitokala-Lii500 charger module. This can be seen in Fig. 4. below.

In scenario 1, with a charging current variation of 500 *mA*, the battery takes approximately 2 hours and 5 minutes to reach full charge. Meanwhile, in scenario 2, with a charging current variation of 1000 *mA*, the battery requires about 1 hour and 10 minutes to reach full charge. After the battery is fully charged, the internal resistance and voltage values are measured again to gather data post-charging.

The next step is to assemble the battery charger circuit for scenario 3 by connecting a 19*V* power supply to the XL4016 charger module to reduce the voltage to 4.2 *V*, and adjusting the desired output current variation to 3000 *mA*. This can be seen in Fig. 5.

Fig. 4: Battery charging for scenario 1 and scenario 2

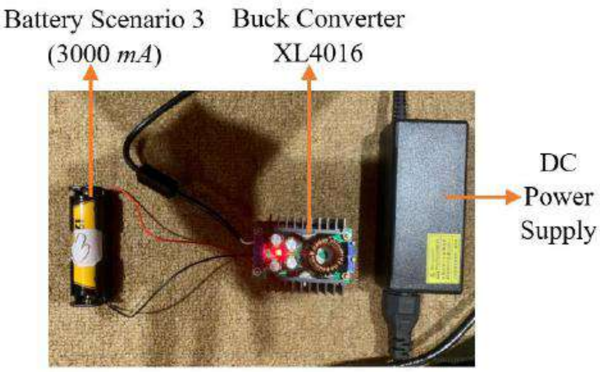

Fig. 5: Battery charging for scenario 3

During the charging phase of scenario 3 with a current variation of 3000 *mA*, the battery requires approximately 35 minutes to reach full charge. However, the time needed for the battery to charge from empty to full is considered too long. This is due to the charging current supplied by the XL4016 module to the *lithium-ion* battery not reaching precisely 3000 *mA*. This is because the *lithium-ion* battery used in this study does not have a *C-Rate* specification that allows such a high current to flow.

The ideal time required to charge a 1200 *mAh* battery should only take 24 minutes if the charging current flowing from the XL4016 module reaches 3000 *mA*. When charging the battery load, the LED on the XL4016 module will be colored red, which means that the module by continuously flowing charging current, this condition can be referred to as constant current mode. Then the LED will be blue when the battery is fully charged which means that current is no longer flowing from the module to the battery, but the voltage value remains constant to keep the battery in full condition, which means the module is in constant voltage mode. Once the battery is fully charged it then takes measurements of the internal resistance value and voltage back to collect data after the charging process.

The next stage is to assemble the discharging module using the Zhiyu ZB2L3 module which is supplied with a DC voltage supply of 5 *V*, the Zhiyu ZB2L3 module has a discharge current setting value of 1 *A*. The installation scheme of the discharge module can be seen in Fig. 6.

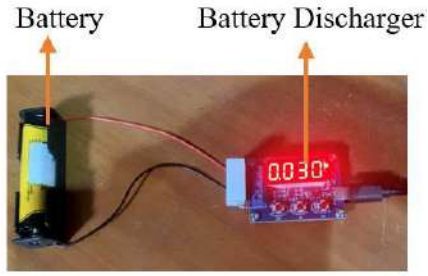

Fig. 6: Battery discharging system

In this stage, the battery is installed in the Zhiyu ZB2L3 module to undergo the discharging process with a minimum discharge voltage limit of 3*V*. This value is chosen because it is considered safe to discharge the battery without damaging it. The discharging process takes approximately 1 hour and 25 minutes, and it is considered complete when the LED screen flashes continuously, indicating that the battery capacity value has been reached.

After all stages are completed, the process continues with the final measurement of internal resistance values for all three batteries using the YAOREA YR1030+ Internal Resistance Tester module. This process is repeated until the internal resistance and battery voltage values are obtained after the discharging process. The measurement process is repeated 20 times, representing 20 charging and discharging cycles.

The final stage of this research is the creation of a trend graph comparing the internal resistance values of the batteries when new with the internal resistance values after undergoing 20 charging and discharging cycles.

III. RESULTS

The process of measuring the internal resistance value of the batteries is conducted over 20 charging and discharging cycles. These measurements are taken after the batteries undergo the charging process as well as after they undergo the discharging process. The results of these measurements are recorded in graphs that show the increase in internal resistance values across the three current variation scenarios. These graphs can be seen in Fig. 7., Fig. 8., and Fig. 9.

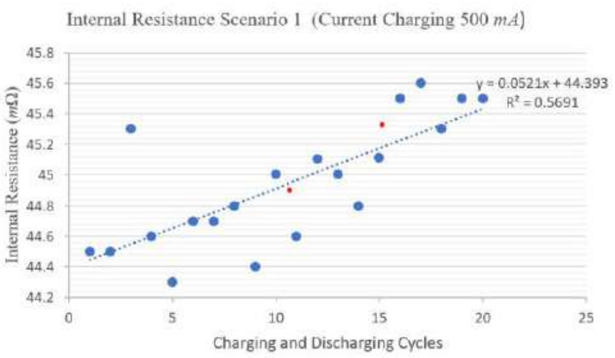

Fig. 7: Internal resistance graph of scenario 1 (500 mA)

In Fig. 7., it can be observed that the data for the internal resistance value in the charging current variation scenario of 500 mA has an initial value of 44.5 mΩ. This value increases to 45.5 mΩ, indicating that the battery experiences an increase in internal resistance of 1 mΩ after undergoing 20 charging and discharging cycles.

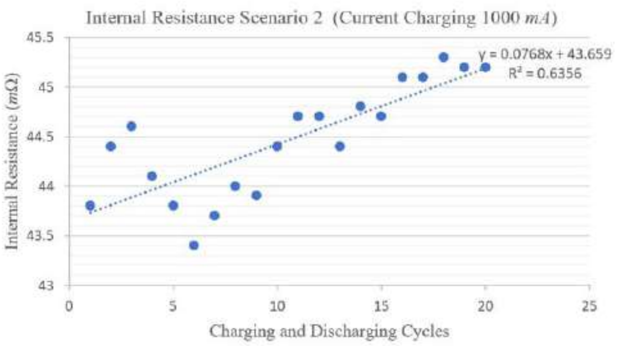

Fig. 8: Internal resistance graph of scenario 2 (1000 mA)

In Fig. 8. it can be seen that the data of the internal resistance value in the scenario of a charging current variation of 1000 *mA*, has an initial value of 43.8 *mΩ* whose data increases to a value of 45.2 *mΩ*, which means that the battery experiences an increase in the value of internal resistance by 1.4 *mΩ* after 20 charge and discharge cycles.

In Fig. 9., it is evident that the data for the internal resistance value in the charging current variation scenario of 3000 *mA* has an initial value of 41.5 *m*Ω. This value increases to 43.6 *m*Ω, indicating that the battery experiences an increase in internal resistance of 2.1 *m*Ω after undergoing 20 charging and discharging cycles.

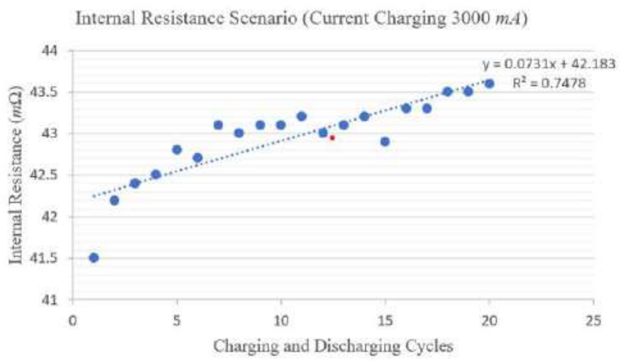

Fig. 9: Internal resistance graph of scenario 3 (3000 mA)

IV. CONCLUSION

From the data obtained in this study, it can be concluded that the larger the charging current variation, the greater the increase in internal resistance in the battery. In the case of scenario 1, with a current variation of 500 *mA*, there is a lower increase in internal resistance, only 1 *m*Ω. Meanwhile, in scenario 2, with a current variation of 1000 *mA*, there is an increase in internal resistance of 1.4 *m*Ω, and in scenario 3, with a current variation of 3000 *mA*, there is the highest increase in internal resistance, which is 2.1 *m*Ω. The larger the value of the charging current variation, the greater the impact on the State of Health (SoH) of the battery, as the internal resistance value will increase more rapidly compared to the charging process using small currents.

One advantage of using larger current variations is shorter charging times. For example, in scenario 3 with a charging current variation of 3000 *mA*, only 35 minutes are needed, which is much faster than scenario 1, where a charging current variation of 500 *mA* requires about 2 hours and 5 minutes.

REFERENCES

[1] 6 Jenis Baterai Mobil Listrik dan Karakteristiknya. Retrieved Augustus 8 , 2023, from https://nissan.co.id/new-press/artikel/6-jenis-baterai-mobil-listrik-dan-karakteristiknya/

[2] Measuring Internal Resistance of Batteries. Retrieved December 18, 2023, from https://learn.sparkfun.com/tutorials/measuring-internal-resistance-of-batteries/internal-resistance

[3] Metode Pengisian Baterai Asam Timbal. Retrieved Augustus 9, 2023, from https://henduino.github.io/library/ototronik/leadacid-charger/

[4] Putra, R., Rusdinar, & Kurniawan. (2015). Desain dan Implementasi Sistem monitoring dan Manajemen Baterai

Mobil Listrik. Bandung: Fakultas Teknik Elektro, Universitas Telkom.

[5] Farizy, A., Asfani, & Soedibjo. (2016). Desain Sistem Monitoring State of Charge Baterai Pada Pengisian Station Mobil Listrik Berbasis Fuzzy Logic Dengan Mempertimbangkan Temperature. Surabaya: Jurusan Teknik Elektro, Fakultas Teknologi Industri, Institut Teknologi Sepuluh November.

[6] Susanti, R., Rumiasih, Carlos, & Firmansyah. (2019). Analisa Penentuan Kapasitas Baterai dan Pengisiannya Pada Mobil Listrik. Palembang: Politeknik Negeri Sriwijaya.

[7] Suwanto. (2016). Rancang Bangun Sistem Pengisian Baterai Berbasis Smart Pengisian Dengan Metode Pengisian Arus Konstan. Surabaya: Program Magister Bidang Keahlian Instrumentasi, Fakultas Matematika dan Ilmu Pengetahuan Alam, Institut Teknologi Sepuluh November.

[8] Fan, Y., Yijie, L., & Renjing, S. (2023). A Module-Level Pengisian Optimization Method of Lithium-Ion Battery Considering Temperature Gradient Effect of Liquid Cooling and Pengisian Time. China: Dallan University of Technology.

[9] Arunagirinathan, S. (2023). Analysis of a Li-Ion Battery State of Charge by Artificial Neural Network. Department of Electrical and Electronics Engineering, Government College of Technology, India.

[10] Fioritti, Sacarpelli, Pellegrino, Lutzemberger, Micolano, & Samalone. (2023). Battery Lifetime of Electric Vehicles by Novel Rainflow-Counting Algorithm With Temperature and C-Rate Dynamics: Effect of Fast Charging, User Habits, Vehicle-To-Grid, and Climate Zones. University of Pisa, Italy.

[11] Zhicheng, Zhang, Sun, & Liu. (2022). The Electric-Thermal Coupling Simulation and State Estimation of Lithium-Ion Battery. Hebei University of Technology, China.

[12] Xianfei, Zhang, Wang, Zhang, Zhiqiang, Zhu, Zhao, Liu, & Jiang. (2022). Transient Thermal Analysis of The Thermal Management of High-Power Fast Charging Module Using Phase Change Material. Zhongyuan University of Technology, China.

[13] Al-Saadi, Olmos, Saez-de-Ibarra, Mierlo, & Berecibar. (2022). Fast Charging Impact on Lithium-Ion Batteries' Lifetime and Cost-Effective Battery Sizing in Heavy-Duty Electric Vehicle Applications. Vrij Universiteit Brussel, Belgium.

[14] Jiang, Berliner, Lai, Asinger, Zhao, Herring, Bazant, & Braatz. (2021). Fast Charging Design for Lithium-Ion Batteries via Bayesian Optimization. Department of Automation, Tsinghua University, Beijing, China.

[15] Makeen, Ghali, & Memon. (2022). A Review of Various Fast Charging Power and Thermal Protocols for Electric Vehicles Represented by Lithium-Ion Battery Systems. Electrical Engineering Department, Faculty of Engineering, The British University of Egypt, Egypt.

[16] Irianto, Yanaratri, & Rahmatullah. (2021). Desain dan Simulasi Battery Charger Metode CCCV (Constant Current-Constant Voltage) dengan Kontrol Logika Fuzzy Menggunakan MATLAB. Politeknik Elektronika Negeri Surabaya, Surabaya.

[17] Ramadhan, Putra, Salam, Parizi, Anugrah, & Warmi. (2022). Perancangan Model Wireless Fast Charging Menggunakan Constant Current Dan Constant Voltage Pada Kendaraan Listrik. Program Studi Teknik Elektro, Institut Teknologi Padang, Padang.

[18] Bakhtiar, & Tadjuddin. (2021). Pengaruh Battery Management System (BMS) Pada Pengisian Baterai Lithium Sistem PLTS. Teknik Elektro, Politeknik Negeri Ujung Pandang, Makassar.

[19] Anshori, Siswojo, & Hasanah. (2020). Teknik Fast Charging Baterai Lithium-Ion Menggunakan Logika Fuzzy. Universitas Brawijaya, Surabaya.

[20] Nugraha, Ersha, Sunarno, Qudsi, Frediansyah, & Prabowo. (2021). Desain Baterai Charger Kendaraan Listrik dengan Metode Constant Current dan Constant Voltage. Politeknik Elektronika Negeri Surabaya, Surabaya.

[21] Yaqin, Pratiwi, & Maison. (2019). Rancang Bangun Charge Controller Panel Surya Dengan Menggunakan Sistem Fast Charging. Fakultas Teknik Elektro, Universitas Jambi, Jambi.

[22] Tarigan, Setiawan, & Edi. (2022). Rancang Bangun Voltmeter Ekonomis Berbasis Android Dengan Kalibrasi Open Circuit Voltage Menggunakan Metode Moving Average Untuk Aplikasi Sistem Monitoring Baterai Pada Kendaraan Elektrik. Teknik Otomotif, Mesin Otomotif, Politeknik Astra, Cikarang.

[23] Firmansah, Prastiyo, & Alimi. (2022). Rancangan Bangun Indikator Baterai Untuk Baterai Pesawat Tanpa Awak Menggunakan Sensor INA260 Secara Nirkabel. Teknik Dirgantara, STTKD, Yogyakarta

[24] Mamahit, Ticoh, Memah, & Angmalisang. (2022). Studi Sistem Pengisian Cepat Baterai Kendaraan Listrik Berbasis Papan Pengendali OpenEVSE. Pendidikan Teknik Elektro, Fakultas Teknik, Universitas Negeri Manado, Manado.